ALEXANDRE MARTUSCELLI FARIA

WIND TURBINE NOISE: DEVELOPMENT OF AN AIRFOIL TURBULENT INFLOW NOISE PREDICTION METHOD BASED ON AMIET'S THEORY

São Paulo
2022

ALEXANDRE MARTUSCELLI FARIA

Wind Turbine Noise: Development of an Airfoil turbulent inflow noise prediction method based on Amiet's theory

Versão Corrigida

Tese apresentada à Escola Politécnica da Universidade de São Paulo para obtenção do título de Doutor em Ciências.

Área de Concentração: Engenharia Mecânica Energia e Fluidos
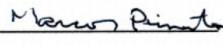
Orientador: Prof. Dr. Marcos de Mattos Pimenta

São Paulo

2022

Autorizo a reprodução e divulgação total ou parcial deste trabalho, por qualquer meio convencional ou eletrônico, para fins de estudo e pesquisa, desde que citada a fonte.

Este exemplar foi revisado e corrigido em relação à versão original, sob responsabilidade única do autor e com a anuência de seu orientador.

São Paulo, ____20____ de ____janeiro____ de ____2022____

Assinatura do autor: _____

Assinatura do orientador: _____

This thesis is entirely dedicated to the memory of my grandfather José Geraldo Faria.

ACKNOWLEDGMENTS

"The universe works on a math equation that never even ever really ends in the end"

-- Isaac Brock of Modest Mouse at
Never Ending Math Equation

RESUMO

Os esforços da comunidade científica no campo das energias renováveis tem se mantido focado em evitar que o acréscimo da temperatura média global ultrapasse a marca de 1.5°C. Nesse cenário, a energia elétrica proveniente de fonte eólica tem experenciado uma rápida e contínua expansão em sua capacidade instalada global durante as duas últimas décadas. Essa expansão, entretanto, é balizada por múltiplos fatores síncronos, como a disponibilidade de terras e impactos relacionados ao ambiente, à fauna e às pessoas, ao se levar em consideração que esta expansão leva os parques eólicos para áreas cada vez mais próximas a regiões habitadas. Uma das grandes preocupações que vêm atreladas às novas tecnologias de turbinas eólicas de eixo horizontal é que o nível de ruído seja mantido em compasso com as legislações de controle de ruído locais. Como o nível de ruído produzido por uma turbina eólica é diretamente proporcional ao diâmetro do rotor, e turbinas eólicas modernas apresentam pás cada vez maiores, por aumento simultâneo na conversão de energia, é mandatório que seja adotado o ruído como variável de projeto e buscar novas geometrias de pás que combinem eficiências aerodinâmica e aeroacústica. PNoise é um módulo para predição de ruído aerodinâmico de aerofólios e pás de turbinas eólicas desenvolvido na Poli-USP pelo grupo Poli-Wind em colaboração com a Universidade Tecnológica de Berlim, para o desenvolvimento do software de projetos de pás de turbinas eólicas QBlade. O PNoise, através de uma modelagem 2D, leva em consideração, de maneira combinada, as fontes de ruído aerodinâmico, de modo a obter uma predição precisa do espectro sonoro e contribuir para o projeto de pás mais silenciosas, sem que haja diminuição na efetividade da conversão de energia. O ruído de aerofólio consiste da combinação também sincronizada de múltiplas fontes, sendo as duas principais o ruído próprio do aerofólio e o ruído provocado pelo escoamento turbulento incidente. A modelagem matemática e a integração do último no código do QBlade é o principal objetivo deste estudo. O ruído provocado pelo escoamento turbulento incidente é causado pela interação entre escalas de turbulência e a superfície do aerofólio. Tende a ser dominante sobre o ruído próprio de aerofólio na faixa de frequências baixa a média (até cerca de 2000 Hz) e apresenta alta sensibilidade ao par escala integral de comprimento e intensidade de turbulência. Também centrais para este estudo são a aplicação da teoria de Amiet, suas extensões e a discussão com relação à modelagem do espectro de turbulência, considerando a usual adoção do espectro de turbulência homogêneo e isotrópico de von Kármán e a teoria de distorção rápida de Batchelor (RDT). Como sabido, condições de turbulência atmosférica dificilmente são obtidas em túnel aeroacústico e portanto um diferente comportamento espectral deverá ser observado em cada caso. Desta forma, ambas situações devem ser cobertas pelo novo método de predição de ruído provocado pelo escoamento turbulento incidente no PNoise.

Palavras-Chave – Energias renováveis, turbinas eólicas, ruído de aerofólio, ruído provocado pelo escoamento turbulento incidente, teoria de Amiet, aeroacústica.

ABSTRACT

The scientific community efforts in the field of renewable energy have been focused on avoiding an increase of the average global temperature that surpasses the 1.5°C mark. In that scenario, wind energy had experienced a rapid and continuous growth in its installed capacity worldwide along the past two decades. This expansion however is bounded synchronously by multiple factors, such as land availability and impacts on the environment, fauna and people, once wind farms are being pushed more and more to the vicinity of inhabited areas. One of the major concerns regarding newer technologies of horizontal axis wind turbines is maintaining the noise level in line with each local noise control regulations. As noise level is direct proportional to the wind turbine rotor diameter, and newer blades are becoming larger and larger because of the simultaneous increase on power output, it is mandatory to adopt the noise emission as a wind turbine blade design constraint and look after new blade geometries that combine both aerodynamic and aeroacoustic efficiency. PNoise is an airfoil and wind turbine noise prediction module developed at Poli-USP by Poli-Wind group in collaboration with TU-Berlin QBlade wind turbine blade design software. PNoise, through a 2D mathematical modeling, takes into account the sources of airfoil noise combined in order to have an accurate spectrum prediction and contribute to the design of quieter blades without lowering the power output. Airfoil noise consists of a synchronized effect of multiple sources, being the main sources the airfoil self-noise and the turbulent inflow noise. The mathematical modeling and integration of the latter within QBlade code is the main objective of this study. The turbulent inflow noise is caused by the interaction between turbulent scales and the airfoil surface. It tends to be dominant over airfoil self-noise in the low to mid frequency range (up to 2000 Hz) and is very sensitive to the pair turbulence integral length scale and intensity. Central to this study are the application of Amiet theory and its extensions, and also the discussion regarding turbulence spectrum modeling considering the usual von Kármán homogeneous and isotropic turbulence assumption and Batchelor rapid distortion theory (RDT) that adds anisotropy effects on noise. As it is known, atmospheric turbulence conditions are hardly obtained in a aeroacoustic tunnel setup, and so a distinct turbulence spectrum may be observed in each case. Therefore, both may be covered by PNoise novel turbulent inflow noise prediction method.

Keywords – Renewable energy, wind turbines, airfoil noise, turbulent inflow noise, Amiet theory, aeroacoustics.

LIST OF FIGURES

LIST OF TABLES

LIST OF SYMBOLS AND ACRONYMS

ABEEÓLICA	Brazilian Association for Wind Energy
$ABNT$	Brazilian Association of Technical Standards
b	Airfoil semi-chord
BPM	Brooks, Pope and Marcolini
β	Prandtl-Glauert compressibility factor ($\beta = \sqrt{1 - M^2}$)
c	Airfoil chord
c_0	Sound velocity
d	Airfoil half-span
D_L	Spherical directivity
δ	Displacement thickness
E	Fresnel integral
f	Frequency
Φ	Flow velocity potential
φ	Flow velocity potential Fourier transformed in time and space coordinates
$GWEC$	Global Wind Energy Council
$HAWT$	Horizontal-axis wind turbine
i	Imaginary unit ($i = \sqrt{1}$)
k	Wavenumber ($k = \omega/c_0$)
k_e	Average wavenumber of the energy-containing eddies
K_x	Specific chordwise wavenumber
k_x	Chordwise wavenumber
$\bar{k}_x$	Normalized wavenumber ($\bar{k}_x = k_x b$)
$\bar{k}_x^{\,*}$	Normalized wavenumber considering Mach ($\bar{k}_x^{\,*} = \bar{k}_x M/\beta^2$)
K_y	Specific spanwise wavenumber ($K_y = y/\sigma_0 k$)
k_y	Spanwise wavenumber
$\mathcal{L}$	Aeroacoustic lift response function
LE	Leading-edge
μ	Compressibility parameter, dynamic viscosity
M	Flow Mach number
$NREL$	National Renewable Energy Laboratory
ω	Angular frequency
$\hat{p}_{ref}$	Pressure of reference
$PNoise$	Wind turbine noise assessment module for QBlade
PSD	Power Spectral Density
$QBlade$	Wind turbine preliminary design tool
RDT	Rapid Distortion Theory
Re	Reynolds number
ρ	Flow density

SPW	Sound power level
SPL	Sound pressure level
U	Mean longitudinal flow velocity
u	Velocity fluctuation root-mean-square
WT	Wind turbine
WTN	Wind turbine noise

CONTENTS

1   INTRODUCTION

1.1   Wind energy expansion worldwide

For the past 25 years, climate change due to the anthropogenic factor has become the center of the world debate. United Nations Climate Conference has established that the increase in the average global temperature should be limited to 1.5°C, while also promoting climate justice, thus ensuring an uniformity to the temperature increase. To do so, among other measures to be taken, a demand on planning new energy matrices around the globe takes place, as well as the necessity to revisit and to redefine the concept of sustainable development. Yet, the need for energy rose through the same period, the planning of a new energy matrix is required as an effort to diminish CO_2 emission, as well as other greenhouse gases and pollutants. Consequence of that is the global expansion of alternative energetic sources, such as photovoltaic panels and wind turbines (WT).
Being the latter matter of this study, let us have a overlook on wind energy participation over the past half of a century. The Global Wind Energy Council (GWEC) presents every year an updated outlook to the global installed wind capacity. One can precisely assert that the expansion is being pushed to higher levels as Figure 1 illustrates.
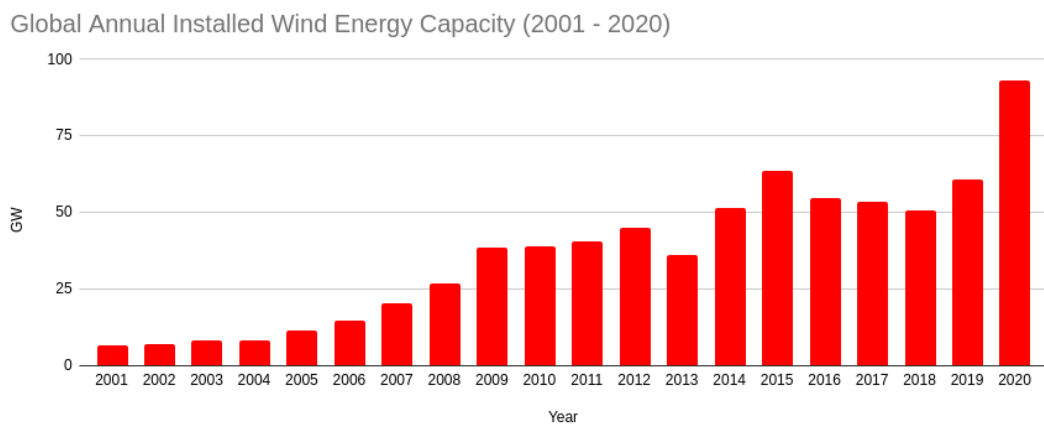
Figure 1: Global annual installed wind capacity 2001 – 2020 (GWEC, 2021).

With respect to the tendency observed in Figure 2, it is expected that the global installed wind capacity exceeds the 800 GW mark within the next two years.
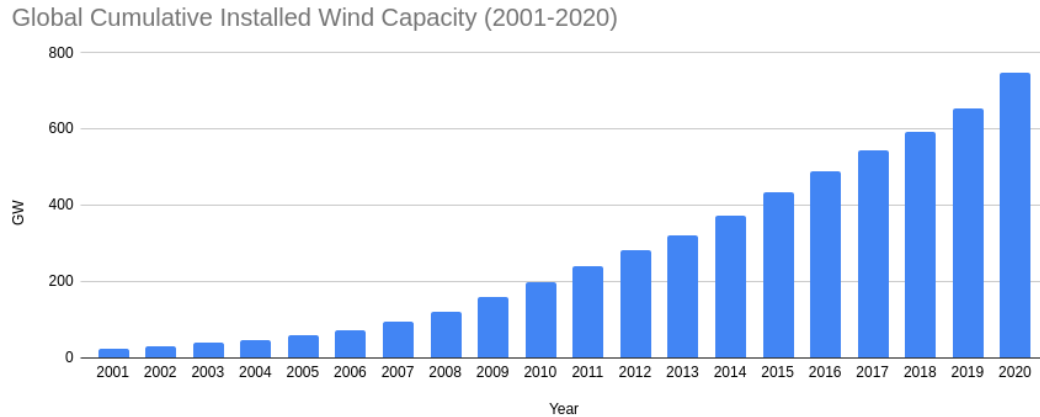
Figure 2: Global cumulative installed wind capacity 2001 – 2020 (GWEC, 2021).

This expansion, however, is not equally distributed along the different regions, continents or even countries. A close look at Figure 3 evidences the discrepancies between these regions. That means underdeveloped continents experience a slower expansion in terms of wind energy capacity when compared to more developed regions. Asia, driven by China and India, has expanded the wind energy participation in a pace which is faster than the rest of the world together. Europe has an ascendant pace, which can be direct related to the presence of most of the wind turbine manufacturers in European soil, especially in Germany, Spain, the UK, France, Spain and Denmark. Despite having a large presence of WT manufacturers, North America has presented a more unstable profile of expansion, decreasing linearly its pace for the period of 2015-2017. Latin America has experienced a significant rise from 2013 to 2014 on the rate of expansion of wind energy installed capacity. However, since 2015, many of the Latin America countries have been facing economic and political crisis, which have aggravated deindustrialization rate and have forced the reduction of state investments in strategic fields, such as energy and infrastructure. Since the most recent GWEC Report (GWEC, 2021) does not provide an equivalent to this chart, Figure 3 remains from a batch of past data from GWEC (GWEC, 2018).

ANNUAL INSTALLED CAPACITY BY REGION 2009-2017

	2009	2010	2011	2012	2013	2014	2015	2016	2017
Asia	15,507	21,481	20,981	15,624	18,252	26,058	33,962	27,721	24,412
Africa & Middle East	251	153	8	131	240	934	953	418	618
Europe	10,660	10,466	10,393	12,862	12,524	12,988	13,831	13,926	16,803
Latin America	471	459	771	1,248	1,240	3,744	3,678	3,078	2,578
North America	11,008	6,208	8,137	14,807	3,112	7,382	10,829	9,359	7,836
Pacific Region	578	294	345	358	655	568	381	140	245

Source: GWEC

Figure 3: Annual installed capacity by region 2009 – 2017 (GWEC, 2018).

An even closer look can be taken when comparing the top ten countries with the higher onshore wind power installations. Figure 4 shows that the Popular Republic of China is at the top of the list and has an installed capacity that represents near 40% of the entire global amount. The Chinese installed capacity is almost equals to the summation of the USA, Germany, India, Spain, France and Brazil onshore installed capacity. The European installed capacity is led by Germany, with 7.79% of the global installed capacity. Brazil is the only representative from Latin America among the ten countries, with 2.51% of the world's wind energy installed capacity.

Also noteworthy is the rest of the world contribution, which corresponds to 15.87% of the global installed capacity. That means almost 85% of the participation on onshore wind energy corresponds to only ten countries.

Cumulative global onshore wind power installations by end of 2020

Rest of World 15.87%
Italy 1.49%
Canada 1.92%
United Kingdom 1.94%

China 39.34%

Brazil 2.51%
France 2.54%

TOTAL= 707,396 MW

Spain 3.85%

India 5.46%

Germany 7.79%

US 17.29%

GWEC
GLOBAL WIND ENERGY COUNCIL
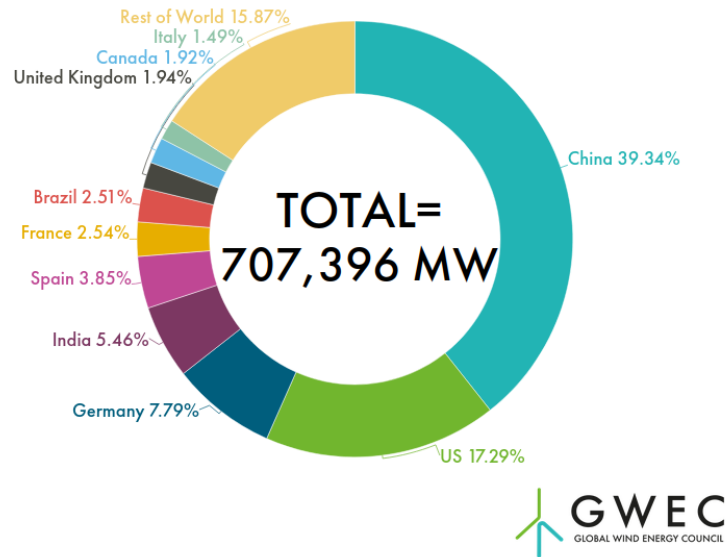
Figure 4: Top 10 cumulative onshore wind installed capacities by December, 2020 (GWEC, 2021).

1.2 Wind energy expansion in Brazil

According to data from Brazilian National Agency of Electrical Energy (ANEEL), wind energy was definitively introduced in Brazil in the decade of 2000 and began its expansion since 2005, as Figure 5 shows. The wind energy expansion was then consolidated in 2009, when it has achieved pace of more than 250 MW per year. In 2015, the installed wind capacity raised 2753.8 MW, which was the maximum growth rate. Comparing to Figure 1, it can be observed that the expansion behavior of Brazilian installed wind capacity follows the global rates.

Brazilian Annual Installed Wind Capacity (2005 - 2020)
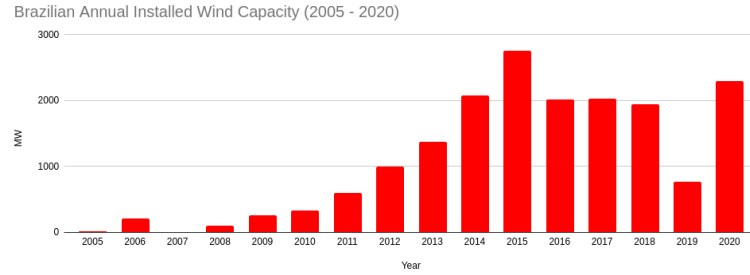
Figure 5: Brazilian annual installed wind capacity 2005-2020 (Adapted from Abeeólica, 2021).

Same is true for the cumulative installed wind capacity. As is presented in Figure 6, its behavior follows the global tendency illustrated in Figure 2.

Brazilian Cumulative Installed Wind Capacity (2005 - 2020)
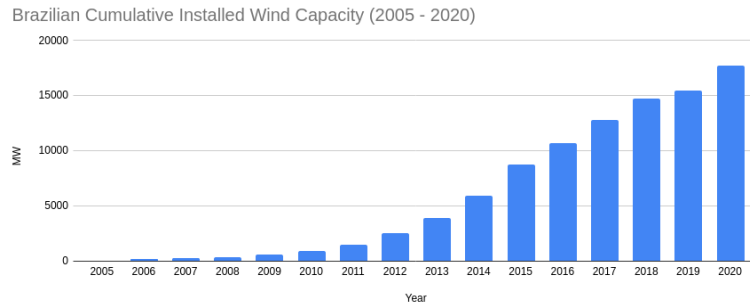
Figure 6: Brazilian cumulative installed wind capacity 2005-2020 (Adapted from Abeeólica, 2021).

Brazilian Agency of Wind Energy (Abeeólica) presents every year a detailed report about the annual wind power generation. A comparison between the four Brazilian regions which are responsible for the country's wind energy generation is shown in Figure 7. There can be seen that the wind energy potential is most concentrated at the south and northeast regions, corresponding to 11.5% and 85.6%, respectively. North and southwest regions, on the other hand, have experienced significant decrease on their generated wind power in the year of 2020.

Generation and its share of the power supply	2019		2020		
	Generation (TWh)	Share	Generation (TWh)	Share	Growth %
REGION					
Southeast	0.06	0.1%	0.05	0.1%	-11%
South	5.62	10.3%	6.34	11.5%	13%
Northeast	47.13	86.7%	47.08	85.6%	0%
North	1.55	2.9%	1.51	2.7%	-3%
Total	**54.37**	**100%**	**54.98**	**100%**	**1.1%**

Figure 7: Wind generation and its share per region (Abeeólica, 2017).

Also according to Abeeólica Annual Report (Abeeólica, 2021), the five states responsible for the most part of wind energy generation in 2020 were Bahia (16.22 TWh), Rio Grande do Norte (15.59 TWh), Ceará (5.95 TWh), Piauí (5.91 TWh) and Rio Grande do Sul (5.81 TWh).

1.3 Social and environmental impacts due to wind energy expansion in Brazil

The expansion of wind energy finds, however, many boundaries as other sources, given its intrinsic necessity for physical space and its single requirements, such as a propitious and perennial wind regime. Besides that, it has become common throughout the years the so-called NIMBY (acronym for "not in my backyard") attitude, which has been spread out not only in small communities, but also in global politics, and noticeable consequences are conflicts of interest based on misinformation. Because of that, a class of preliminary study is being conducted, the environmental licensing. In order to aid this first, researchers propose another category, the social licensing, which is responsible to promote dialogue with the local communities near wind farm areas and learn about their main concerns regarding wind energy facilities from building to operation.

In order to have an accurate comprehension of possible conflicts regarding wind energy expansion, one should have an overview of wind distribution. Taking Brazil as this study case, by having a look at the wind potential distribution in the map shown in Figure 8, one can see that the highest average wind potential is concentrated near the east coast, where the wind annual mean velocity can reach up to 8 m/s, while the continental regions appear to have more discrete results for the wind annual mean velocity, which is around 4 m/s.

From the population perspective, however, the same areas seen as high wind energy potential localities present the highest population density in the whole country, specifically the east coast, as mentioned before. When comparing the maps presented on Figure 8 and Figure 9, it is conclusive that population, as well as the local fauna, may be somehow affected by - or at least concerned about - construction and operation of wind farms. This evidences necessity of both environmental and social licensing. A study from Barreto *et al.* summarizes social and environmental concerns (Barreto *et al.*, 2019), being the principal described as follows:

- Impact on native population and tourism: in Brazilian northeast region, wind farm might have a negative impact on seaside and indigenous population which have

a subsistence relation with the sea area, where most of the wind farms are being placed. This is also reported as a potential threat to tourism, since the littoral landscape could be affected by WT (Meireles, 2011).

- Home devaluation: Gibbons (Gibbons, 2015) points out that, for the specific case of England, wind farms could represent a home devaluation of up to 12%, considering an average distance of 14 km between a siting with 20 WT units and the inhabited area. An increase on the size of the wind farm and shortening of the distance to inhabited areas could further promote home devaluation.

- Noise generation: the annoyance potential due to wind turbine noise (WTN), more specifically, the noise generation from large scale horizontal axis wind turbines (HAWT) is an issue commonly related by communities near wind farms worldwide, and actually the most annoying aspect of wind energy (Bowdler and Leventhall, 2011). Since there is a direct relationship between noise and size of the wind turbines, this demands project and design solutions. In order to do so, the need of mapping the WT main noise sources takes place, as well as knowing the local noise control regulations.

- Access blocks: another negative impact of the wind energy expansion is the potential access block caused by wind farms to recreation areas, or even road restriction, because of the installation. Study conducted by Mendes (Mendes, 2015) reports that after a wind farm building in Ceará the only access to a specific inhabited area was a gate operated by the wind energy facility, and the community was not allowed to pass through freely. This case was only solved after court decision.

- Telecommunications: Angulo *et al* (Angulo *et al*, 2014) reports interference of the presence of wind farms in telecommunication, more specifically for television, and both analog and digital signals.

Given that these items refer to negative anthroposocial aspects of living in the proximity to wind farms or changing the landscape, it does worth mentioning that neither wildlife impact nor the problems regarding sustainable energy generation in opposition to deforestation of virgin areas in order to provide the wind farm siting were covered by Barreto *et al.*. The latter is center of discussion nowadays and one of the main worries when it comes to ensure that the increase in the average global temperature will be kept below the 1.5 °C mark.
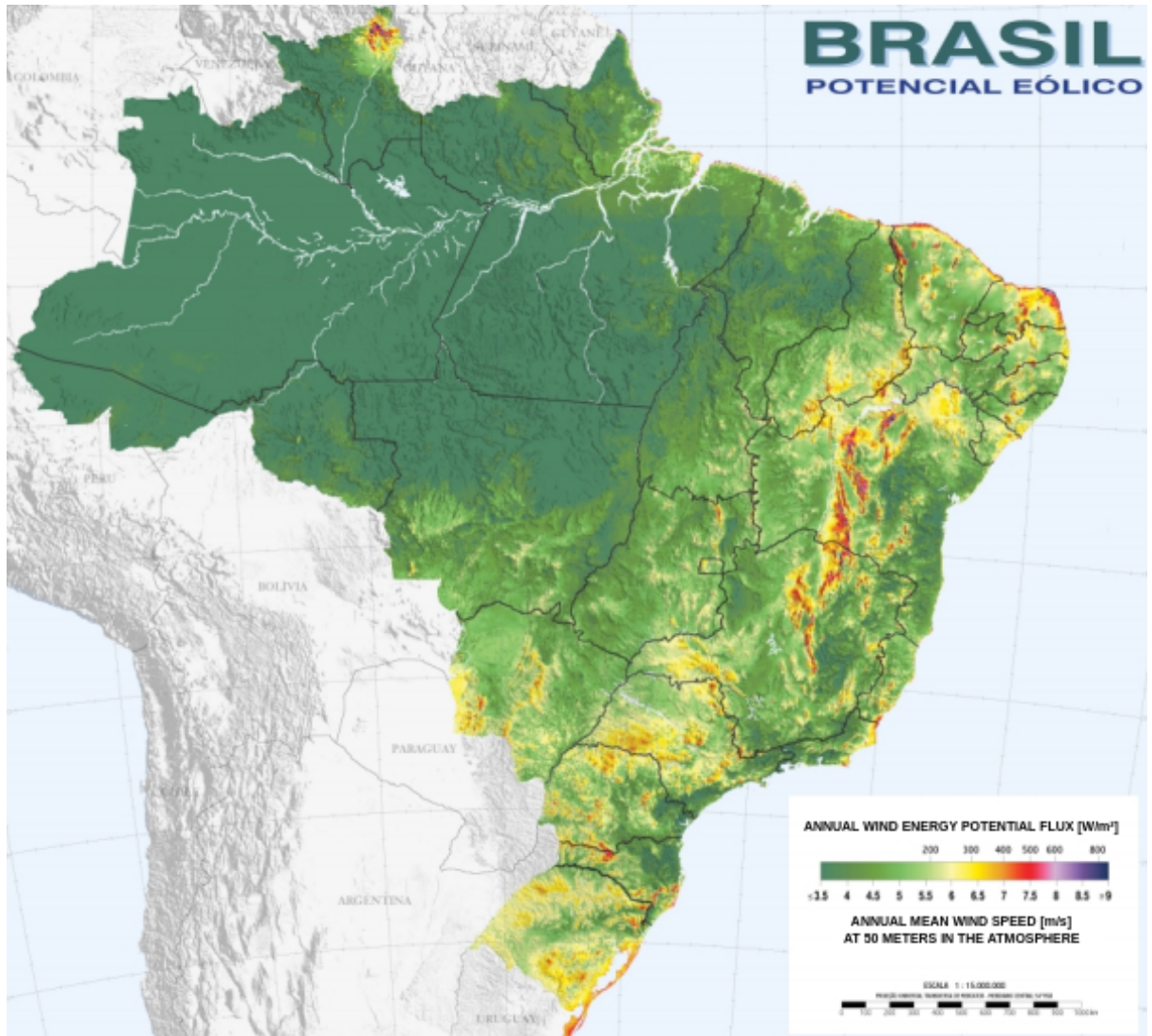
Figure 8: Wind potential distribution in Brazil (Atlas do potencial eólico brasileiro, 2002).

Figure 9: Population density in Brazil (IBGE, 2010).

Wildlife impact of wind turbines, which is commonly associated to bird and bat strikes, is considered low, when compared to other causes. A NREL 2005 report states that buildings, communication towers, traffic, and even house cats are more harmful than WT. However, the recent deactivation of 800 wind turbine units at the Californian desert, after a repowering process, reduced the bird strike rate by 35% between 2006 and 2010. Specifically in Brazil, there is still a lack of studies quantifying the impact of wind farms on the avian fauna. There is a recommendation, however, to avoid bird concentration areas or bird migration routes, when planning a wind farm site. The comparison between Figure 8 and Figure 10 draws attention to the fact that the Atlantic migration route and the Northeast migration route are coincident with areas with high wind energy potential. That means extra attention should be paid to these regions, when planning a wind farm.

Figure 10: Bird migration routes in Brazil (ICMBIO, 2016)

.

At last, when it comes to wind turbine noise, the loudness associated to WT can be compared to other human everyday utensils, as Figure 11 shows. The dependency on distance is also observed.
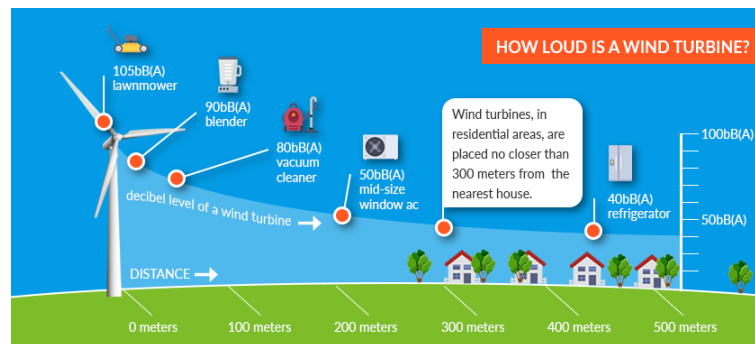
Figure 11: Wind turbine loudness compared to other everyday utensils

.
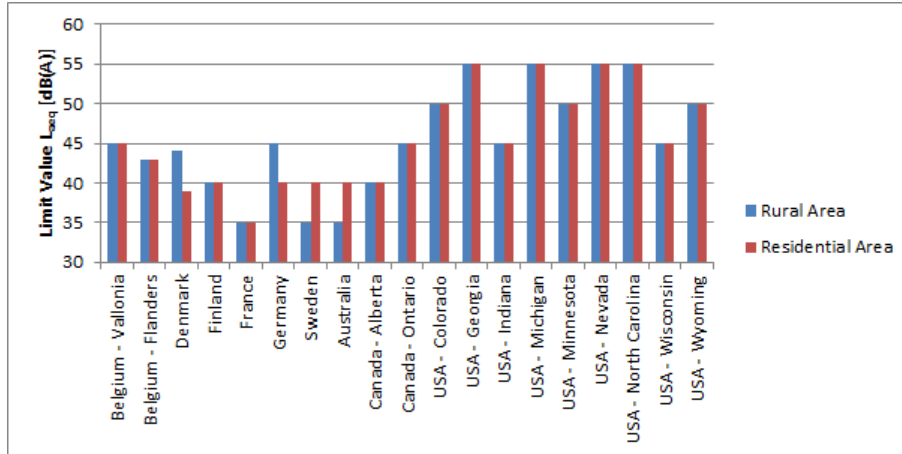
Figure 12: Limit values for wind turbine noise in various regions (Adapted from Koppen and Fowler, 2015)

.

Noise control regulations do not follow a specific pattern worldwide, as Figure 12 illustrates. The limits presented are night time values. By examining the limit values for the equivalent sound levels, L_{aeq}, one can infer that many European countries have more stringent noise limits, when compared to the permitted levels in the USA and Canada (Koppen and Fowler, 2015), and this is indeed a physical limitation to wind energy expansion.

It can also be seen that while Denmark and Germany allow higher noise levels at rural areas than at residential areas, Swedish and Australian regulations are on the opposite side. This evidences the dependency on demographic aspects for each country and region. In Brazil there are no specific regulations concerning WTN currently. That means wind turbine noise is subject to general noise regulations. The maximum noise levels allowed are regulated by Brazilian Association of Technical Standards (ABNT), NBR 10151 Standard (Acoustics – Measurement and evaluation of sound pressure levels in inhabited environments - Application for general use), (NBR10151, 2019).

In order to illustrate the impact of regulations on planning WT sites, consider the van der Borg linear model, which relates the wind turbine sound power level (SPW) simply to the rotor diameter D (GIPE, 2004):

$$SPW = 22 \cdot \log D + 65 \ dBA. \tag{1.1}$$

Taking the wind turbine as an omnidirectional noise source, far from ground, whose waves propagate spherically, without attenuation, and, considering a stationary observer placed at the far-field, in a distance r from the wind turbine, Bistafa (2011) presents an expression

for the sound pressure level (SPL) at any distance r, as follows:

$$SPL = SPW - 20 \cdot \log r - 11 \ dBA. \tag{1.2}$$

Combining equations (1.1) and (1.2), it is possible to obtain a relation between the rotor diameter D and the distance r from the source, considering the specific allowed sound pressure level:

$$\log r = \frac{22 \log D - SPL + 54}{20} \ dBA. \tag{1.3}$$

Table 1: Allowed noise limits in Brazil (Adapted from ABNT, 2019)

Type of area	Criteria level (dBA)	
	Day	Night
Farms and country land	40	35
Strictly residential urban area or hospital or school area	50	45
Mixed use, predominantly residential	55	50
Mixed use, commercial and service prone	60	55
Mixed use, recreational prone	65	55
Industrial area (mostly)	70	70

Considering the Brazilian daytime criteria level for maximum acceptable sound pressure level in farms and country lands, 40 dB(A) (NBR10151, 2019), the relation established by equation (1.3) is illustrated by Figure 13. This makes explicit the fact that the larger the WT unit, the farther away its siting must be from dwellings, in order to fulfill legal noise requirements. By recovering Figure 11 one can ensure that the 300 meters distance is referred to small WT, whose rotor diameters are smaller than 40 meters.
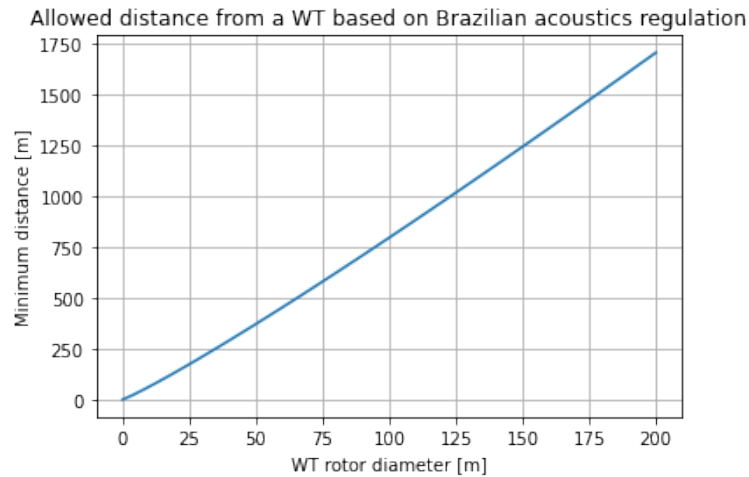
Figure 13: Allowed distances from WT units, considering the rotor diameter and Brazilian acoustics regulation – acceptable SPL in farms and country lands of 40 dB(A) (NBR10151, 2019).

With that said, it has been made evident that the expansion of wind energy technologies is mostly bounded by land availability and by noise control policy. For a more efficient planning, the possibility of having accurate noise prediction methods, as assessment tools, at the preliminary project phase plays a fundamental role, in order to guarantee the manufacture of quieter WT models. Considering the horizontal axis wind turbines (HAWT) as object of study, the first step adopted is to map the potential noise sources of a HAWT. Second is to define criteria to evaluate the contribution of each source based on various operational conditions. The selected noise prediction methods need to be validated against experimental data gathered from the literature. Once validated, the noise prediction method should be arranged on a user-friendly interface that allows the complete noise assessment for WT blades and rotor.

1.4 Wind turbine noise sources

In general, noise radiated from a WT can be originated mechanically or aerodynamically. Mechanical noise is usually associated to the generator and, for indirect drive units, older WT models, to the gearbox. Before it gets airborne, the mechanical noise is transmitted along the structure. It is then radiated from surfaces like the nacelle, the tower and the rotor blades. Noise originated aerodynamically may be classified as self-noise and interaction noise (Blake, 1986). Portion of the aerodynamic noise is radiated from the blades and from the wake in the near-field region, the so-called airfoil self-noise. The

interaction noise, on the other hand, is radiated from the interaction of the rotor with inflow turbulence and with the tower wake. Figure 14 illustrates the contribution from each individual component of a HAWT to its total sound power level.
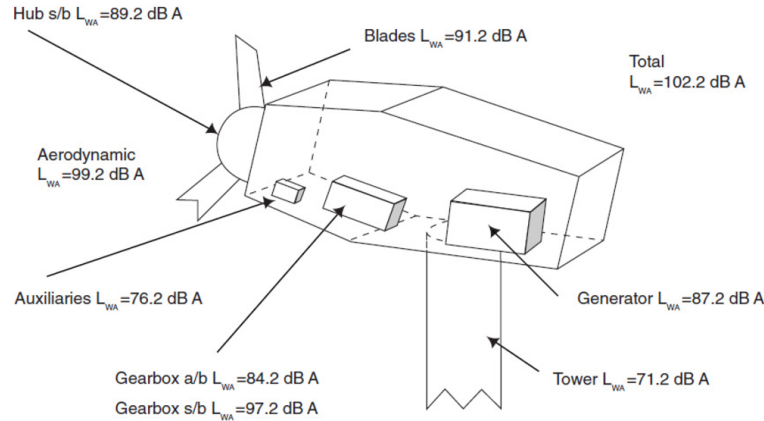
Figure 14: Individual contribution of components to the total sound power level of a WT (Jianu, Rosen and Naterer, 2012)

.

However, with the general adoption of the WT rotor in an upwind position for HAWT, and the fact that modern WT units' transmission systems are direct-driven, part of the mechanical noise is minimized, as well as the rotor/tower wake interaction noise. Since the rotor/tower wake interaction noise becomes negligible, the interaction noise is referred to as turbulent inflow noise. Both self-noise and turbulent inflow noise are produced by mechanisms that involve the flow around the WT blades. As the blades are arrangements of airfoil profiles, so the self-noise mechanism is also treated as airfoil self-noise, or even airfoil trailing-edge (TE) noise, while the turbulent inflow noise is also referred to as airfoil leading-edge (LE) noise. Wind turbine noise prediction methods are the central subject of this thesis and will be further discussed in the next sections.

1.5   *QBlade*

QBlade is an open-source code wind turbine calculation software, distributed under the general public licensing (GPL) initiative. It provides tools for preliminary WT blade design, simulation, and performance analysis for HAWT and also vertical axis wind turbines (VAWT) in an integrated environment with a very intuitive graphic user interface (GUI), as can be seen in Figure 15.

Years after its inception, many improvements were implemented, being boosted by a pro-

fessional integration of existing open codes, such as XFLR5 and Aerodyn/FAST, and other powerful tools, i.e. blade design module, blade element momentum (BEM) module, 360 polar extrapolation models, structural analysis, and so on, by the TU-Berlin team. In the year 2016, a wind turbine noise prediction tool was embedded into *QBlade* code, the *PNoise*.
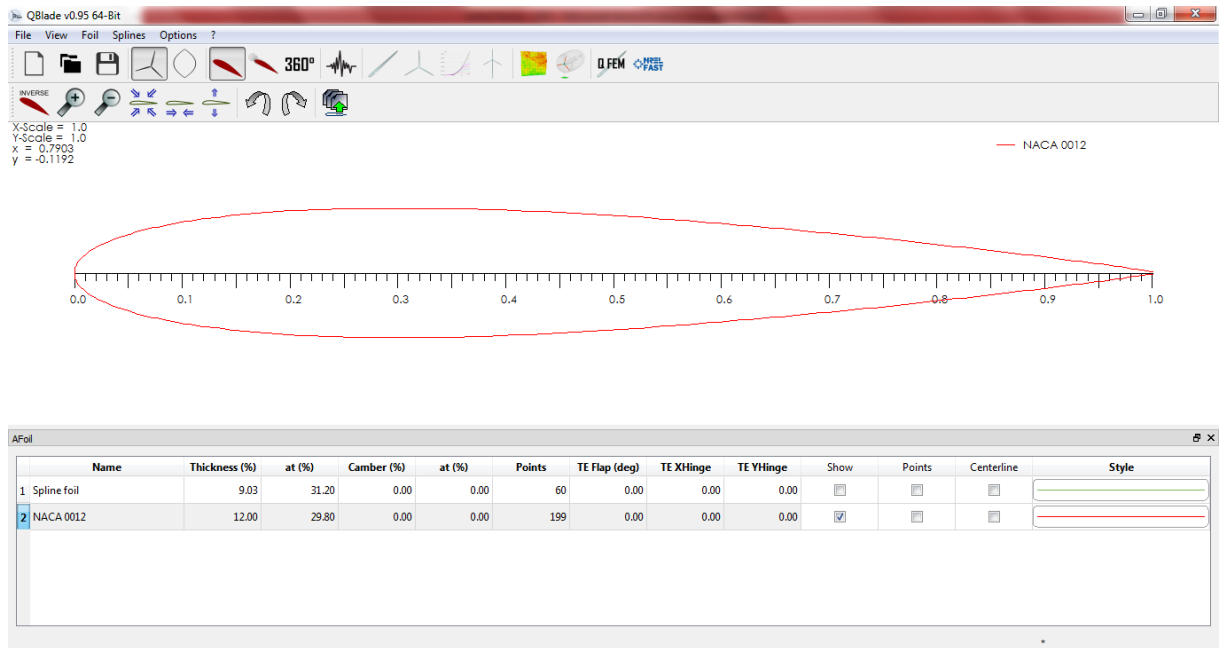
Figure 15: *QBlade* environment

.

1.5.1 *PNoise*

Currently, *PNoise* consists of a 2D airfoil noise prediction module, where a modified version of the Brooks, Pope and Marcolini turbulent boundary layer trailing-edge noise (NASA BPM TBL-TE) prediction method, which was proposed by Saab (Saab, 2016), was integrated into *QBlade* v0.95 and released in June, 2016. The calculation considers the geometrical aspects of the airfoil subjected to arbitrary flow conditions, as Figure 16 illustrates, for a wide range of operational points, based on displacement thickness correlations (Saab and Pimenta, 2016).
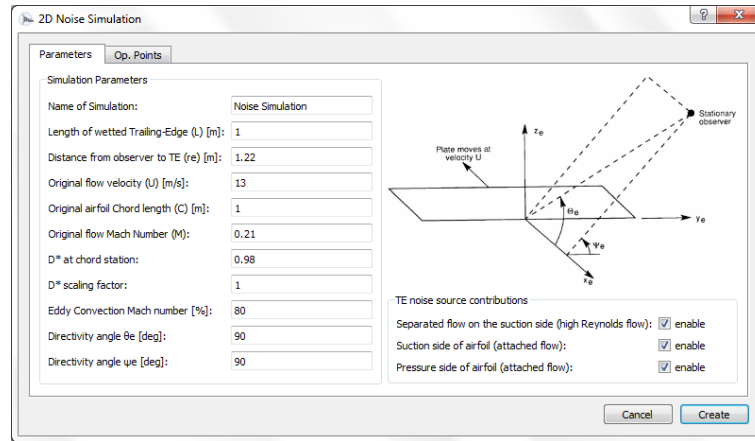
Figure 16: *PNoise* input dialog inside *QBlade*

.

After running *PNoise* simulation, the resultant noise profiles are obtained, as Figure 17 shows:
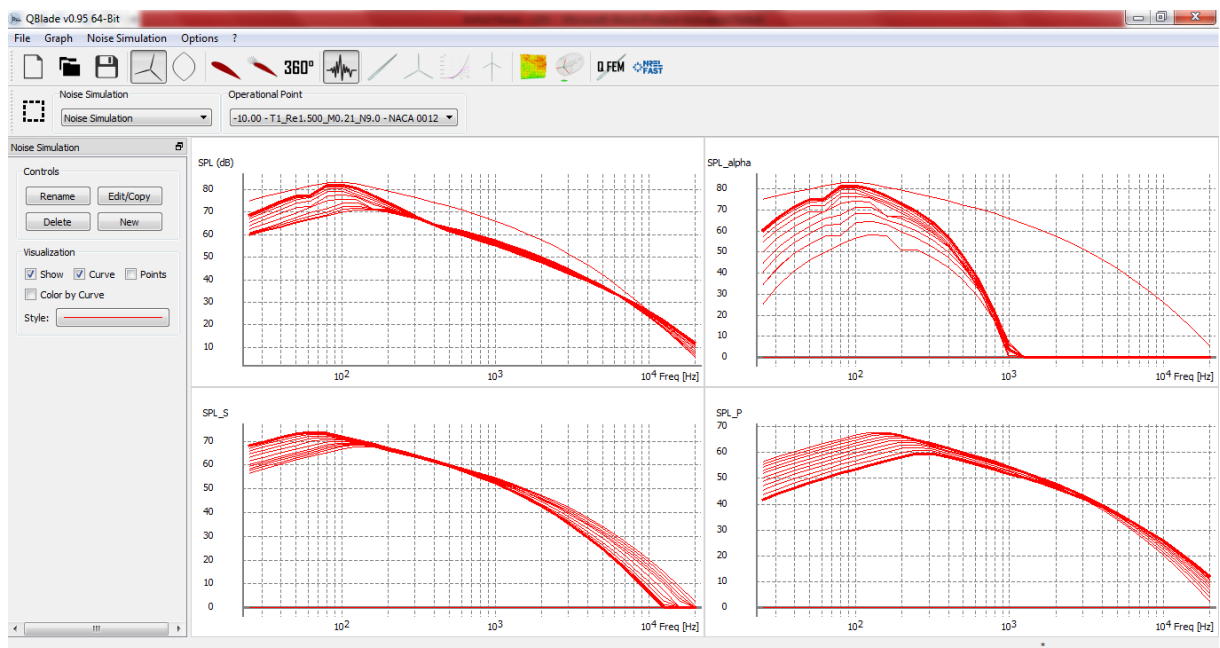
Figure 17: *PNoise* output window

.

Among the desirable steps of the further development of *PNoise* are the incorporation of other relevant airfoil noise sources prediction methods, primarily the turbulent inflow noise, which is the central subject of the present thesis, and an upcoming quasi-3D full wind turbine noise prediction module.

1.6 Objectives and scope of the thesis

This thesis main objective is to select and implement a turbulent inflow noise prediction method in *QBlade* software, as an additive to the current *PNoise* functionalities. Being *QBlade* a WT blade preliminary design tool, that requires as a constraint the airfoil LE noise prediction method to have a low computational cost, no complex computational aeroacoustics (CAA) calculation should be employed, restricting the method selection to the semi-empiric formulations. In addition to that, it is also desirable that the selected method presents any degree of compatibility to the already implemented modified NASA BPM TBL-TE.

The selection of the method is guided by understanding basic airfoil aeroacoustics, more specifically based on studies conducted by Amiet, after the 1975 manuscript, which brought light to the problem of broadband noise emitted by an airfoil in response to an incoming turbulent flow.

The semi-empiric approach follows the theoretical development side-by-side, not only in this first article, but also later partnership with Paterson, with Schlinker and with Simonitch. The latter, an article from 1986, begins the discussion on the turbulent energy spectrum modeling, at that time dealing with helicopter rotor noise due to ingestion of atmospheric turbulence. Simonitch study brought Batchelor rapid distortion theory (RDT) to the center of discussion on airfoil turbulent inflow noise. However, a gap of nearly 25 years is observed on this theme, being only revisited by Santana in 2016, which then presented solid evidences that near the airfoil surface, the turbulence cannot be approximated by homogeneous and isotropic condition.

In the early nineties, more exactly 1992, Lowson has presented further modifications to the Paterson and Amiet semi-empiric method, which had a limitation of being representative of acoustic tunnel experiments, with a fixed observer position, directly overhead the airfoil LE. The main contribution of Lowson to the semi-empirical methods is the incorporation of a directivity factor, in a similar fashion to the NASA BPM TBL-TE, so the observer can be placed anywhere in a spherical coordinates space. Despite presenting this spatial advantage, Lowson method still considers the homogeneous and isotropic turbulence assumption, modeled after the von Kármán turbulence spectrum.

For the purpose of further developing the semi-empirical methods, the present thesis intends to bring the RDT turbulent energy spectrum model to Lowson turbulent inflow noise prediction method. This is made after fully understanding Amiet broadband noise theory and the derivation of the correspondent semi-empirical Amiet-based methods in a detailed bibliography review of the subject.

Directly after the derivation of the RDT-modified Lowson method for turbulent inflow noise prediction comes the need for experimental validation. Despite the lack of available acoustic tunnel measurement data concerning turbulent inflow noise, there are three recent studies, from 2018, 2019 and 2020, by Juknevicius and Chong, Bampanis *et al.* and Narayanan and Singh, respectively, which conducted experiments for evaluating the turbulent inflow noise attenuation by attachment of serrations on the airfoil leading-edge. These two articles present data for three different flow conditions, each for a different airfoil geometry.

At this point, the most noticeable limitation of the experimental validation of the RDT-modified Lowson method is the fact that in both of the available manuscripts containing turbulent inflow noise measurement data, the experiments are conducted for thin airfoils (the maximum airfoil relative thickness is 12%, for the NACA 65 profile, from Narayanan and Singh setup), which despite being enough for validating an Amiet-based noise prediction method that considers the hypothesis of thin airfoils, that is not representative of a wind turbine blade airfoil geometry, so without thicker airfoils experimental measurements for the LE noise, it is not possible to set a proper validity range for the method yet.

Discussion on thickness effects for airfoil noise prediction methods are subject of discussion of many authors. Gershfeld have introduced a thicker airfoil noise prediction method in 2004, being revisited nowadays by Zhong *et al.* (Zhong *et al.*, 2020), with focus on CAA calculations. In the field of semi-empirical methods, Guidati and Moriarty (Guidati *et al.*, 1997, Moriarty *et al.*, 2004, Buck *et al.*, 2018) and Tian and Cotté (Tian and Cotté, 2016) have presented a SPL reduction expression for Amiet-based airfoil noise prediction methods. Being these methods, at the time, derived under the assumption of homogeneous and isotropic turbulence modeled after von Kármán turbulent energy spectrum, it does not contemplate properly the RDT-modified Lowson method. The present study investigates then, even in a qualitative manner, how this correction should be applied in order to be suitable for the RDT-modified method, or if they do present any eventual pitfall, since its derivation after a simple linear regression.

After accomplishing the specific objectives listed above, the more adequate airfoil LE noise prediction method will be seamlessly integrated to *PNoise* and *QBlade* environment, as part of the under development 3D noise prediction module. All of the limitations and the validity range of the method must be informed to the user.

1.7 Thesis outline

This thesis provides the reader, in chapter 1, an overview on wind energy expansion worldwide, as well as the specific Brazilian case. Discussion around wind farm planning and environmental impacts, focused on the concept of social licensing, human impact of noise, noise control regulations are also presented in this first chapter. There is also a brief contextualization to the reader about research on WTN prediction and the partnership between Poli-Wind and TU-Berlin. Finally, the research objectives are declared.

In chapter 2, a review on theoretical aeroacoustics is presented, focused on the application for wind turbines, covering both airfoil self-noise and turbulent inflow noise mechanisms. The theme turbulent inflow noise is then further detailed, presenting the fundamentals of Amiet's theory and many extensions. In this chapter, turbulence modeling is also matter of understanding, so many aspects are covered, from describing turbulence intensity and turbulence integral length scale based on terrain and height to the actual eddies behavior and its energetic spectrum. Differences between the turbulence velocity spectrum modeling after von Kármán homogeneous and isotropic turbulence and Batchelor rapid distortion theory are detailed and a modified version of the semi-empiric Lowson turbulent inflow noise prediction method is derived. After that, at the end of the literature review a note on aerodynamics of wind turbine blades is presented, in order to give the reader a basic understanding of how *QBlade* and *PNoise* work, and how is the environment set up to the turbulent inflow noise prediction method integration.

Chapter 3 is dedicated to the methodology, which consists of defining the validation tests and its constraints, which correspond to an acoustic tunnel experimental setup. Two main sets of experiments are detailed here at this point for airfoils with relative thickness up to 8%. For higher relative thickness values, as it is the case for WT blade airfoils (which normally range from 18% to 24%), it is proposed to investigate the actual need for a SPL correction model based on the airfoil thickness at the preliminary design step. In the recent literature, there is mention to two models, one that is proposed by Tian and Cotté, based on the maximal airfoil thickness, and other, proposed by Guidati and Moriarty, and revisited by Buck *et al.*, which is, on the other hand, based on two specific local thicknesses of the airfoil.

Chapter 4 contains the quantitative comparison between the experimental data obtained from the literature and the predicted turbulent inflow noise SPL, considering both turbulence modeling, RDT and von Kármán turbulence spectra, in order to validate the obtained expression and define the most consistent and adequate method to be implemented in *PNoise*. The investigation of the necessity of a SPL correction is made through

a qualitative comparison between the reduction obtained from the expressions presented at the end of chapter 3 and the prediction from the modified RDT-Lowson method, due to the lack of available measurement data for thicker airfoils.

In chapter 5, a comparison of the prediction methods with measured data from two old full scale wind turbines is performed. Given that in their original study both of the noise spectra are mainly due to the turbulent inflow noise, it seems to be a promising opportunity to test the prediction methods in a situation other than an acoustic tunnel measurement, where turbulence is no longer grid-generated, but based on local atmospheric conditions, so structures will be much larger than the scales measured in an acoustic tunnel.

Chapter 6 presents an overview of the newly implemented *PNoise* code and its features inside *QBlade*, most of them concerning the achievements and contributions of the present research.

Chapter 7 concludes this thesis, by summarizing its achievements and listing some possibilities for further development and future research.

The appendices section brings the basis for basic understanding fluid dynamics and aeroacoustics before entering the airfoil field.

2 A REVIEW ON AIRFOIL AEROACOUSTICS

An airfoil in a turbulent flow experiences a fluctuating lift which radiates noise to the far-field. This fluctuating lift is a result of the unsteady pressure field produced by the airfoil in response to turbulence (Staubs, 2008). The turbulent flow field can be either produced upstream the airfoil, by the presence of inflow distortions and other aerodynamic elements, or it can be also consequence of the development of a turbulent boundary layer over the airfoil surface, in case of a steady inflow. The upstream mechanism is linked with the noise produced close to the airfoil leading edge, while the mechanism related to the turbulent boundary layer is a self-noise mechanism, discussed in details by Saab (Saab, 2016).

As it is represented by Figure 18, the two noise generation mechanisms coexist and are responsible for the overall noise spectra. Normally, for WT applications, airfoil self-noise constitutes the dominant noise source. For certain flow conditions, however, i.e. when the incoming turbulence intensity and the integral length scale of the inflow eddies are large enough, the pressure fluctuations caused by the boundary layer eddies is smaller compared to the pressure fluctuations due the turbulent inflow, and the turbulent inflow noise mechanism is predominant over the self-noise.
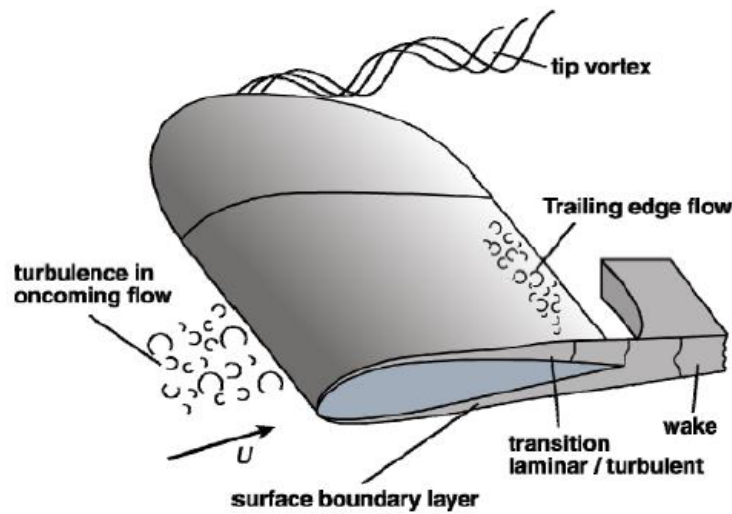
Figure 18: Flow around a WT rotor blade (Wagner, Bareiß and Guidati, 1996)

.

The following subsections present a discussion regarding characterization of the airfoil noise mechanisms as well as an extensive review on WT noise prediction methods, focused on the turbulent inflow noise source and at the part that closes this chapter, a new expression for airfoil turbulent inflow noise prediction is derived.

2.1 Airfoil self-noise

Airfoil self-noise is characterized as most broadband, mainly high frequency, noise mechanism. The airfoil self-noise mechanism can be divided in six sources: the trailing-edge noise, which consists of noise produced due to interaction of boundary layer turbulence with the blade trailing edge, the tip vortex noise, which is produced by the interaction of tip turbulence with the blade tip surface, the stall-separation noise, caused by the interaction of turbulence with the blade surface, the laminar boundary layer noise, which is caused by non-linear boundary layer instabilities interacting with the blade surface, the blunt trailing-edge noise, which is characterized as the noise produced by vortex shedding at the blunt trailing-edge, and the noise from flow over holes, slits and intrusions, this last produced by unstable shear flow over holes and slits, and vortex shedding from intrusions (Rogers, Manwell & Wright, 2006). The five first mentioned sources are displayed at Figure 19. Laminar boundary layer noise, blunt trailing edge noise and noise from flow over holes, slits and intrusions are characterized as tonal and can be avoided. The remaining turbulent boundary layer trailing-edge (TBL-TE) noise, tip noise and stall-separation

noise are the broadband components.
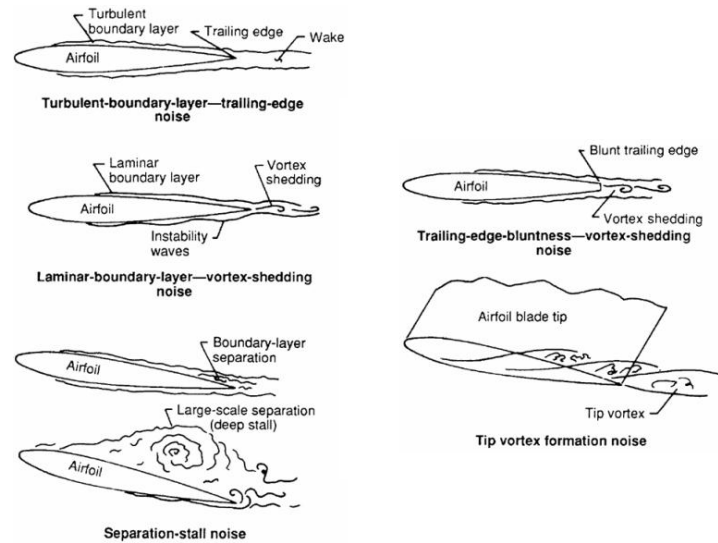
Figure 19: Airfoil self-noise mechanisms (Adapted from Brooks, Pope and Marcolini, 1989)

.

For high Reynolds numbers applications, the interaction between turbulent boundary layer and the airfoil trailing edge is dominant over the other self-noise mechanisms, and produces a whistle-like noise, which frequencies range from 750 Hz up to 2 kHz. For lower flow velocities, on the other hand, a laminar boundary layer is developed, and its instabilities produce vortex shedding at the airfoil TE. The vortex shedding can also occur at the blade tip or at a blunt TE airfoil. In addition to that, for non-zero angles of attack (AoA), detachment of the boundary layer near the airfoil TE can happen, producing a smooth stall or, if the detachment occurs near the airfoil LE, low frequency noise is produced, similar to flow around bluff bodies (Martinazzo, 2015).

Acoustic field measurements accomplished within the European research project SIROCCO context confirmed that the TBL TE noise is the dominant noise mechanism for large HAWT units (Oerlemans, Sijtsma and Méndez-López, 2007) (Kammruzzaman, Lutz, Nübler and Krämer, 2011) (Oerlemans, 2011). That means the airfoil TBL-TE noise can be considered a convenient approximation to the whole airfoil self-noise source. Figure 20 illustrates the individual contribution of each airfoil self-noise source to the overall mechanism. The total noise spectrum is also displayed. Most of the frequency range, from 250 Hz to 4000 Hz, is dominated by TBL-TE noise source (Bareiß, Guidati and Wagner, 1994).
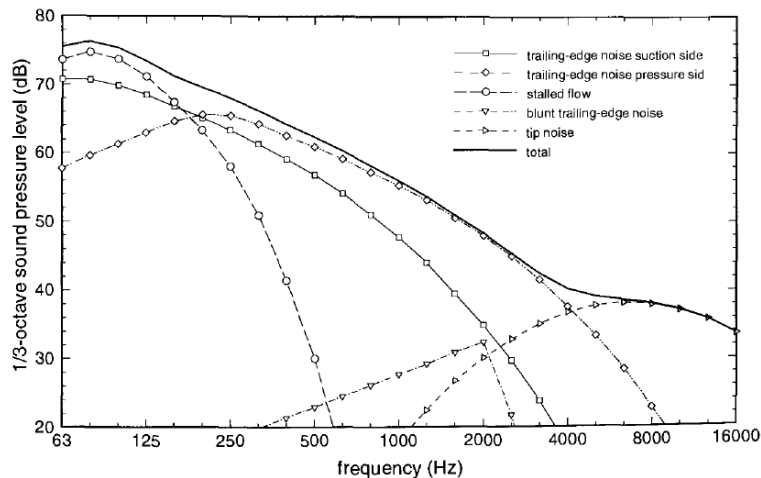
Figure 20: Calculated contributions of airfoil self-noise individual sources, for a WT blade, and the total SPL spectrum (Bareiß, Guidati and Wagner, 1994)

.

Following the discussion around airfoil turbulent boundary layer trailing edge noise being a convenient approximation to the airfoil self-noise source, an overview on TBL-TE noise prediction NASA-BPM method should be introduced. Since this research is contextualized as a sequel to Saab thesis and concerns the turbulent inflow noise source, a more complete explanation is provided by Saab (Saab, 2016).

2.2   Airfoil TBL-TE BPM noise prediction method

The NASA-BPM model is a semi-empirical method for predicting airfoil noise, based on experimental acoustic tunnel measurement data from a NACA0012 profile. After results of Ffowcs Williams and Hall (1969), an expression for the scaling law applied to TBL-TE noise can be described by (Ffowcs Williams and Hall, 1969)

$$\hat{p} \propto \rho^2 \overline{u^2} \frac{U^3}{c_0} \left(\frac{Ll}{r^2} \right) \overline{D}, \tag{2.1}$$

where $\overline{u^2}$ is the mean square turbulence velocity fluctuations, L is the spanwise extent of the wetted edge by the flow, l is a characteristic turbulence correlation scale and $\overline{D}$ is the directivity factor, which is equal to 1 for observers normal to the surface of the TE. For the BPM method, l is approximated to δ or δ^* and $\overline{u^2} \sim U^2$ (Brooks, Pope and Marcolini,

1989), which results in

$$\hat{p} \propto \rho^2 \frac{U^5}{c_0} \left(\frac{L\delta}{r^2} \right) \overline{D}. \tag{2.2}$$

The relation of the *rms* pressure signal and the sound pressure level is given by

$$SPL = 10 \log_{10} \frac{\hat{p}^2}{\hat{p}_{ref}^2}, \tag{2.3}$$

where $\hat{p}_{ref} = 2 \cdot 10^{-5}$ Pa, which is the standard reference pressure, in S.I. system of units, corresponding to the weakest audible sound at 1000 Hz, or 1 dB. Considering self-noise dominated by the TBL-TE, a spectrum shape, F(St), is assumed, which is a function only of the ratio of the Strouhal number $St = f\delta/U$ and its peak value St_{peak}. The resultant normalized form for the 1/3 octave SPL spectral shape is

$$SPL_{1/3} - 10 \log_{10} \left[\left(\frac{U}{100} \right)^5 \left(\frac{L\delta}{r^2} \right) \right] = F(St) - K, \tag{2.4}$$

where $SPL_{1/3} = OASPL + F(St)$ and K is an empirical constant. Next step in the development of the model was the determination of the parametric dependencies and spectral scaling, resulting in the following initial scaling, for zero angle of attack (AoA).

$$Scaled \quad SPL_{1/3} = SPL_{1/3} - 10 \log_{10} \left[M^5 \left(\frac{L\delta_0^*}{r_e^2} \right) \right], \tag{2.5}$$

where δ_0^* is the displacement thickness at the TE at zero AoA and r_e is the retarded observer distance, fixed at 1.22 m. However, comparing the scaled spectra for airfoils with different chords, it was suggested that $F(St) + K$ was not an adequate representation of the phenomena.

Further studies of the measured data provided means to improve upon the model, and the final scaling expression for the i side follows:

$$Scaled \quad SPL_{1/3,i} = SPL_{1/3,i} - 10 \log_{10} \left[M^5 \left(\frac{L\delta_0^*}{r_e^2} \right) \right] = A \left(\frac{St_i}{St_1} \right) + (K_1 - 3), \quad (2.6)$$

where i = p, s, respectively for pressure and suction sides. $St_1 = St_{peak}$, $St_i = f\delta_0^*/U$ and K_1 is a continuous function that expresses the scaled sound pressure level variation with the chord based Reynolds number Re_c. The total spectra for the TBL-TE noise at zero AoA, in 1/3 octave presentation for both pressure and suction sides is:

$$SPL_{TBL-TE} = 10 \log_{10} \left(10^{SPL_s/10} + 10^{SPL_p/10} \right) \tag{2.7}$$

In order to include angle of attack effects to the total SPL spectrum, a similar relation is derived:

$$Scaled \quad SPL_\alpha = SPL_\alpha - 10\log_{10}\left[M^5\left(\frac{L\delta_s^*}{r_e^2}\right)\right] = B\left(\frac{St_s}{St_2}\right) + K_2. \qquad (2.8)$$

In this case, the flow is not symmetrical about the chord, and the displacement thickness of the suction side is employed as the TBL scaling length, δ_s^*, as well as the Strouhal number, St_s. This result leads to a new expression accounting the three contributions to the predicted of noise, which follows:

$$SPL_{TOTAL} = 10\log_{10}\left(10^{SPL_s/10} + 10^{SPL_p/10} + 10^{SPL_\alpha/10}\right). \qquad (2.9)$$

For more details regarding displacement thickness evaluation, see Brooks *et al.* (Brooks, Pope and Marcolini, 1989).

2.2.1 Modified BPM method for airfoil TBL-TE noise prediction

In order to improve the BPM model, while pursuing higher geometry and flow independence, it was proposed by Saab and Pimenta to replace the original BPM δ^* correlations by coupling the model to a generic flow solver (Saab and Pimenta, 2015). The displacement thickness evaluation was conducted with aid of the the hybrid solver XFLR5 and the employment of computational fluid dynamics Reynolds averaged Navier-Stokes (CFD-RANS), which were then compared to experimental measurement data from Brooks and Marcolini (1985). The results have shown that, the order of magnitude of the error of the displacement thickness is similar, whether evaluated with the XFLR5 code or the CFD-RANS. The computational cost, on the other hand, is much lowe using the XFLR5, which took near five seconds, while the CFD took an average of 2,160 per point. Because of that, the TBL layer solver method selected to feed the BPM TE noise prediction method was the XFLR5 (Saab, 2016).

In addition to that, while the original BPM δ^* correlations produce an average overestimation of 3.5 dB to the total SPL, the XFLR5 have obtained overestimation that range from 0.67 dB to 2.71 dB. As the classic BPM model, however, the current validation of the method is only available for NACA0012 airfoil profiles.

2.3 Turbulent inflow noise

In the case of large HAWT, the broadband noise is also dependent on the turbulent inflow characteristics. Perceived as swishing low frequency noise, the turbulent inflow noise is generated when the atmospheric turbulence encounters the rotor blades. As described in the previous section as an interaction noise source, turbulent inflow noise, or airfoil leading-edge noise, is caused by the flow-surface interaction. Since turbulence is not an uniform phenomenon, its characteristics depend on local parameters, such as eddy size and turbulence intensity.

The eddy size is the most important parameter for determining the inflow turbulent noise (Zhu, 2004). Due to the turbulence structure and the atmospheric stability, a wide range of eddy sizes interacts with the blade, as Figure 21 points out. When the eddy size is larger than the chord length of a specific blade segment, it generates low frequency noise and the blade experiences a fluctuating lift. Therefore, the blade can be simplified as an acoustic dipole, which source strength is equal to the total fluctuating lift on the blade surface. Smaller eddies, on the other hand, generate high frequency noise from the WT blade, and the acoustic dipole simplification (acoustic compactness condition) cannot be applied.
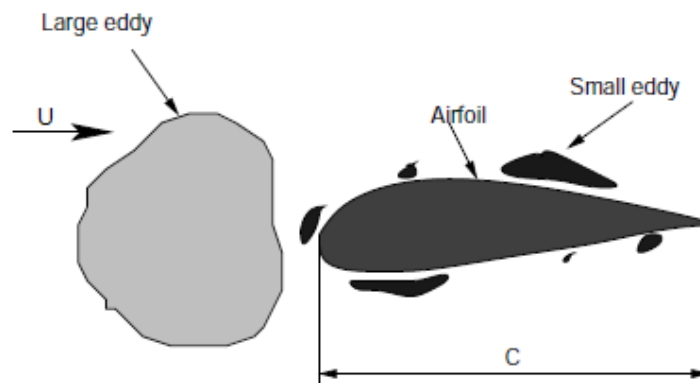
Figure 21: Turbulent eddies of different sizes (Adapted from Zhu, 2004)

.

In addition to that, studies conducted by Paterson and Amiet, Oerlemans and Migliore and Moreau, Roger and Jurdic have shown that the turbulent inflow noise predominant at lower frequencies, where the turbulent structures responsible for the inflow noise generation are the larger structures (Paterson and Amiet, 1976) (Oerlemans and Migliore, 2004) (Moreau, Roger and Jurdic 2005), being the higher frequencies dominated by the airfoil self-noise mechanism. Estimation methods for quantifying TI noise should take into

account parameters such as turbulence intensity, the longitudinal integral length scale, the largest turbulent structure, and the HAWT geometric data, since turbulence depends on atmospheric conditions for specific height values (Staubs, 2008).

Since the leading-edge plays a large role as an airfoil noise source to be analyzed, a method to be implemented in *PNoise* is discussed, in order to predict the generated noise spectrum.

2.4 Amiet broadband noise theory for airfoil LE noise prediction

A theoretical formulation and a semi-empirical methodology, for predicting the turbulent inflow noise, were introduced by Amiet with agreement to Kirchhoff and Curle theories, in order to ensure more reliability to the prediction against measurements. His methodology evaluates the far-field acoustic power spectral density produced by an airfoil in a subsonic turbulent stream, given in terms of characteristic quantities of the turbulence (Amiet, 1975).

The theoretical approach, illustrated by Figure 22, corresponds to compute the acoustic response of an airfoil of $2b$ chord and $2d$ span subjected to a turbulent flow with mean velocity U in the x direction. The noise source S is placed at the center of the airfoil, at the (x_0, y_0, z_0) coordinate system and the observer O is placed at the far-field, represented by the (x, y, z) coordinate system. This is a more general case, since it considers the observer placed at an arbitrary position of the far-field, with the free stream extending to infinity, what suggests suitability for WT noise prediction.
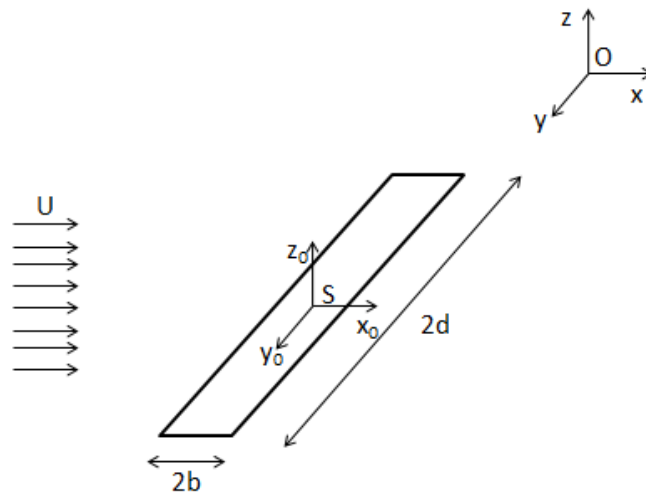
Figure 22: Amiet problem representation

.

The second formulation is a semi-empirical method, based on the acoustic tunnel experiment. An airfoil of $2b$ chord and $2d$ span is placed in a turbulent flow with mean velocity U in the x direction, as Figure 23 illustrates. The y coordinate extends in the spanwise direction and the origin of the coordinate system is placed at the center of the airfoil. The observer is located at the far-field, directly overhead the airfoil, represented as a microphone. This procedure is used to neglect the retarded time differences, what allows one to formulate the far-field sound in terms of the total fluctuating lift of the airfoil.
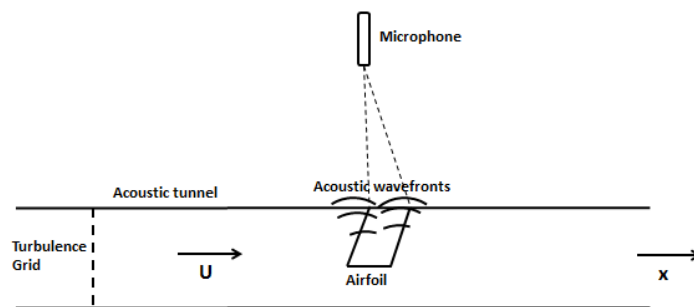
Figure 23: Airfoil in the free stream of an acoustic tunnel (adapted from R.K. Amiet, 1975)

.

Before entering the following subsections, consider the situation of a sinusoidal gust incident to the airfoil leading edge. This allows one to formulate the far-field sound in

terms of the total fluctuating lift of the airfoil. Figure 24 illustrates gusts with wave fronts parallel and skewed relative to the airfoil LE. Parallel type gust is an efficient sound producer, while skewed gusts present a problem, for the far-field sound calculation, given that it varies sinusoidally along the airfoil span, causing substantial cancellation of the lift produced by adjacent spanwise stations. Being turbulent eddies compositions of both parallel and skewed gusts, it would be expected that the sound radiation produced by parallel gusts would be the dominant noise source. This procedure then does not give a good representation of sectional lift, because of the presence of the skewed gusts, but does give a good representation of the total lift, which is the matter that concerns airfoil noise (Amiet, 1975).
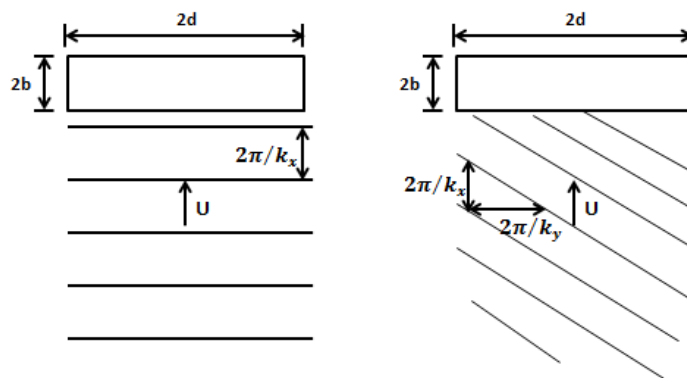
Figure 24: Parallel and skewed gusts incident on the airfoil (adapted from R.K. Amiet, 1975)

.

2.4.1 Theoretical approach

As shown in Figure 22, an airfoil with $2b$ chord and $2d$ span is placed in subjected to turbulent flow with mean velocity U in the chordwise x direction. The y coordinate is extended in the spanwise direction. The origin of the coordinate system is placed at the center of the airfoil, the S position, while the observer is placed at the far-field, in the O position .

For grid-generated turbulence, where $u/U \ll 1$, it is possible to consider the Taylor hypothesis, which is also known as frozen turbulence approximation. This approximation states that in a coordinate system $x' = x - Ut$, which moves attached to the mean flow, the turbulent velocity in the $z = 0$ plane can be written as $w(x', y)$. In the airfoil fixed coordinate system, the turbulent velocity $\hat{w}(x, y, t)$ can be written in terms of its

wavenumber components, $\hat{\hat{w}}_R(k_x, k_y)$, as follows:

$$\hat{w}(x, y, t) = \iint_{-\infty}^{\infty} \hat{\hat{w}}_R(k_x, k_y) e^{i[k_x(x-Ut)+k_y y]} dk_x dk_y, \qquad (2.10)$$

where the double hats on $\hat{\hat{w}}_R$ indicate double spatial Fourier transform of w in terms of the variables x and y. The Fourier components $\hat{\hat{w}}_R(k_x, k_y)$ can be determined from $w(x, y)$ by the inverse relation

$$\hat{w}(x, y, t) = \frac{1}{4\pi^2} \iint_{-R}^{R} w(x, y) e^{i[k_x(x-Ut)+k_y y]} dk_x dk_y, \qquad (2.11)$$

where R is a large, but finite, number. R is not set because of convergence difficulties if $w(x, y)$ does not tend to zero, while x and y go to infinity.

Analytical expressions for the distribution of the pressure jump, ΔP, are provided by Amiet (1975). For a gust of the form of

$$w_g = w_0 e^{i[k_x(x-Ut)+k_y y]}, \qquad (2.12)$$

the distribution of the pressure jump can be written as

$$\Delta P(x, y, t) = 2\pi \rho_0 U b w_0 g(x, k_x, k_y) e^{i[k_x(x-Ut)+k_y y]}, \qquad (2.13)$$

where $g(x, k_x, k_y)$ is the transfer function between turbulent velocity and airfoil pressure jump. The pressure jump in a given point on the airfoil due to all wavenumber components is

$$\Delta P(x, y, t) = 2\pi \rho_0 U b w_0 \iint_{-\infty}^{\infty} \hat{\hat{w}}_R(k_x, k_y) g(x, k_x, k_y) e^{i[k_x(x-Ut)+k_y y]} dk_x dk_y. \qquad (2.14)$$

The Fourier transform with respect to time can be performed to give the frequency dependency of the pressure jump. Since in equation (2.11) the turbulence was assumed to extend between $-R < x < R$, the time integration will be between $\pm T$, where $T = R/U$. Given that

$$\int_{-T}^{T} e^{|\xi|} dt \to 2\pi \delta(\xi) \quad as \quad T \to \infty, \qquad (2.15)$$

the result of the Fourier transform will be

$$\Delta \hat{P}_T(x, y, \omega) = 2\pi \rho_0 b \int_{-\infty}^{\infty} \hat{\hat{w}}_R(K_x, k_y) g(x, K_x, k_y) e^{i k_y y} dk_y, \qquad (2.16)$$

where $K_x = \omega/U$. That is, a given frequency component of the pressure jump is produced by the specific chordwise turbulence wavenumber ω/U.

Since turbulence is a random quantity, rather than work with deterministic quantities such

as time history of the pressure jump at a point, it is necessary to work with statistical quantities such as the cross-power spectral density (PSD), S_{QQ}, of the pressure jump at two points of the surface. The cross-PSD can be written as follows:

$$S_{QQ}\left(x_1, x_2, y_1, y_2, \omega\right) = \lim_{T \to \infty} \left\{ \frac{\pi}{T} E\left[\hat{P}_T^*\left(x_1, y_1, \omega\right), \hat{P}_T\left(x_2, y_2, \omega\right)\right] \right\}, \tag{2.17}$$

where $E\left[\hat{P}_T^*\left(x_1, y_1, \omega\right), \hat{P}_T\left(x_2, y_2, \omega\right)\right]$ denotes the expected value or ensemble average of a quantity.

The only statistical or non-deterministic quantity on the right-hand side of equation (2.16) is $\hat{w}_R$. Thus, if equation (2.16) is used to replace $\Delta \hat{P}_T$ in equation (2.17), all functions other than $\hat{w}_R$ can be taken outside the expected value sign. This operation isolates the quantity $E\left[\hat{\hat{w}}_R\left(K_x, k_y\right), \hat{\hat{w}}_R^*\left(K_x, k_y'\right)\right]$.

However, because of the statistical orthogonality of the wavevectors, it can be shown that

$$E\left[\hat{\hat{w}}_R\left(K_x, k_y\right), \hat{\hat{w}}_R^*\left(K_x, k_y'\right)\right] = \frac{R}{\pi} \delta\left(k_y - k_y'\right) \Phi_{ww}\left(K_x, k_y'\right), \tag{2.18}$$

where

$$\Phi_{ww}\left(k_x, k_y\right) = \int_{-\infty}^{\infty} \Phi_{ww}\left(k_x, k_y, k_z\right) dk_z, \tag{2.19}$$

and $\Phi_{ww}\left(k_x, k_y, k_z\right) dk_z$ is the energy spectrum of turbulence, which modeling is further discussed at subsections 2.4.2 and 2.4.3. Combining equations (2.16) through (2.18) results in a expression for the cross-PSD of the surface pressure jump, as follows:

$$S_{QQ}\left(x_1, x_2, \eta, \omega\right) = \left(2\pi \rho_0 b\right)^2 U \int_{-\infty}^{\infty} g^*\left(x_1, K_x, k_y,\right) g\left(x_2, K_x, k_y,\right) \Phi_{ww}\left(K_x, k_y'\right) e^{ik_y \eta} dk_y, \tag{2.20}$$

where $\eta = y_2 - y_1$ is the spanwise separation of the two points of the airfoil surface for which the cross-PSD is desired. Ignoring end effects of the airfoil, only spanwise separation of the two points enters the equation, not the y coordinate of each point.

The theories of Kirchhoff and Curle are then used to relate the cross-PSD of the surface pressure to the far-field sound. These theories state that the acoustic response of the airfoil can be determined by distributing dipoles over the airfoil surface equal in strength to the force on the surface. The far-field sound produced by a point force of strength $F(x_0, y_0, \omega)e^{i\omega t}\hat{k}$ in a stream of Mach number M is

$$P_1\left(x, y, z, \omega, x_0, y_0\right) = \frac{i\omega z F(x_0, y_0, \omega)}{4\pi c_0 \sigma^2} e^{i\omega \left[t + \frac{M(x - x_0) - \sigma}{c_0 \beta^2} + \frac{xx_0 + yy_0 \beta^2}{c_0 \beta^2 \sigma}\right]}, \tag{2.21}$$

where $\sigma = \sqrt{x^2 + \beta^2\left(y^2 + z^2\right)}$ is the distance from source to the far-field considering compressibility effects, and $\beta = \sqrt{1 - M^2}$ is the Prandtl-Glauert compressibility factor.

For the present problem, the force $F(x_0, y_0)$ is the difference in pressure between the upper and lower surfaces of the airfoil. The far-field pressure can be found by integration of equation (2.17) over x_0 and y_0, the airfoil planform area. If the result of this integration is multiplied by its complex conjugate and the expected value taken, the power spectral density of the far-field noise, S_{pp}, can be shown to be related to the cross-PSD of airfoil loading by

$$S_{pp}(x, y, z, \omega) =$$
$$\left(\frac{\omega z}{4\pi c_0 \sigma^2}\right)^2 \int\int\int\int S_{QQ}(x_1, x_2, \eta, \omega) \, e^{\frac{i\omega}{c_0}\left[\beta^{-2}(x_1 - x_2)(M - (x/\sigma) + y\eta/\sigma)\right]} dx_1 dx_2 dy_1 dy_2. \quad (2.22)$$

If equation (2.20) is now substituted into equation (2.22), an expression for the far-field acoustic PSD in terms of turbulence energy spectrum and airfoil response function results. Defining the following chordwise integral of the surface loading as

$$\mathcal{L}(x, K_x, k_y) = \int_{-b}^{b} g(x_0, K_x, k_y) \, e^{-i\omega x_0 (M - (x/\sigma))/c_0 \beta^2} dx_0, \quad (2.23)$$

it allows the far-field to be written as

$$S_{pp}(x, y, z, \omega) =$$
$$\left(\frac{\omega z \rho_0 b}{4\pi c_0 \sigma^2}\right)^2 U d\pi \int_{-\infty}^{\infty} \left[\frac{\sin^2(d(k_y + \omega y/c_0 \sigma))}{(k_y + \omega y/c_0 \sigma)^2 \pi d}\right] |\mathcal{L}(x, K_x, k_y)|^2 \phi_{ww}(K_x, k_y) \, dk_y. \quad (2.24)$$

The function $\mathcal{L}$ defined by equation (2.23) is related to the degree of non-compactness of the airfoil. If the frequency is small, the imaginary exponent is small, and $\mathcal{L}$ reduces to the sectional lift of the airfoil. Derivation of $\mathcal{L}$ is object of the following sub-sections 2.4.1.1 to 2.4.1.8.

In order to conclude the discussion around the far-field PSD, in order to simplify further equation (2.24), one can note that as the semi-span, d, increases, the quantity in square brackets tends to a delta function

$$\lim_{d \to \infty} \left[\frac{\sin^2 \xi d}{\xi^2 \pi d}\right] = \delta(\xi), \quad (2.25)$$

which leads to the most usual expression

$$S_{pp}(x, y, z, \omega) = \left(\frac{\omega z \rho_0 b}{4\pi c_0 \sigma^2}\right)^2 U d\pi \phi_{ww}(K_x, k_y) |\mathcal{L}(x, K_x, k_y)|^2. \quad (2.26)$$

For physical explanation of this phenomenon and the simplification introduced in equation (2.26), it is recommended to see Amiet, 1975, p.p. 411-413.

2.4.1.1   Linearized airfoil theory

In addition to the flow considerations, now consider the airfoil as an infinitely thin flat-plate. The intensity of the lift dipole is admitted as much larger than the drag dipole, so the noise generation is consequence of the incident gust component perpendicular to the airfoil surface only. In order to compute the $\mathcal{L}$ function, the Amiet problem is solved considering the linearized airfoil theory and prescribing as boundary conditions: the zero velocity potential upstream the airfoil leading edge; zero airfoil surface normal velocity (non-penetration condition) and zero pressure jump at the airfoil trailing edge (Kutta condition) and downstream.

$$\phi\left(x, y, 0, t\right) = 0 \qquad x \leq 0, \tag{2.27}$$

$$\frac{\partial \phi}{\partial z}\left(x, y, 0, t\right) = -w\left(x\right) \qquad 0 \leq x \leq 2b, \tag{2.28}$$

$$\frac{D\phi}{Dt}\left(x, y, 0, t\right) = 0 \qquad x > 2b, \tag{2.29}$$

where x, y and z are directions in a normal system of coordinates and time t, c_0 is the sound speed. The total derivative operator is defined as

$$\frac{D}{Dt} = \frac{\partial}{\partial t} + U\frac{\partial}{\partial x}. \tag{2.30}$$

Considering the mean velocity component normal to the xy plane equal to zero, the linearized flow can be represented in term of velocity potential as

$$\left[\nabla^2 - \frac{1}{c_0^2}\frac{D^2}{Dt^2}\right]\phi\left(x, y, z\right) = 0. \tag{2.31}$$

2.4.1.2   Flow potential as Fourier-type functions

The flow potential function ϕ can be decomposed as a relation of three Fourier-type functions (Santana, Desmet and Schram, 2014) as follows:

$$\phi\left(x, y, z\right) = \varphi\left(x, z\right)e^{i\omega t}e^{i\gamma x}e^{i\alpha y}, \tag{2.32}$$

where $i = \sqrt{-1}$, ω is the perturbation angular frequency, $\gamma = kM/\beta^2$, $\alpha = -k_y$. The flow wave number is represented by $k = \omega/c_0$.
Combining equations (2.31) and (2.32), it is obtained that

$$\beta^2\frac{\partial^2 \varphi}{\partial x^2} + \left(\frac{k^2}{\beta^2} - \alpha^2\right)\varphi + \beta^2\frac{\partial^2 \varphi}{\partial z^2} = 0. \tag{2.33}$$

The following nondimensionalization relations are proposed:

$$\overline{x} = \frac{x}{b}; \overline{y} = \frac{\beta y}{b}; \overline{z} = \frac{\beta z}{b}. \tag{2.34}$$

Equation (2.33) can be written as

$$\frac{\partial^2 \varphi}{\partial \overline{x}^2} + \frac{\partial^2 \varphi}{\partial \overline{z}^2} + \frac{b^2}{\beta^2} \left(\frac{k^2}{\beta^2} - \alpha^2 \right) \varphi = 0. \tag{2.35}$$

Adopting the following definitions

$$k_x = \frac{\omega}{c_0}; k = k_x M; \overline{k}_i = k_i b, \tag{2.36}$$

equation (2.35) becomes

$$\frac{\partial^2 \varphi}{\partial \overline{x}^2} + \frac{\partial^2 \varphi}{\partial \overline{z}^2} + \left(\frac{\overline{k}_x^2 M^2}{\beta^4} - \frac{\overline{k}_y^2}{\beta^2} \right) \varphi = 0. \tag{2.37}$$

The obtained equation (2.37) has a form of a canonical Helmholtz equation, i.e.:

$$\frac{\partial^2 \varphi}{\partial \overline{x}^2} + \frac{\partial^2 \varphi}{\partial \overline{z}^2} + \kappa^2 \varphi = 0, \tag{2.38}$$

where

$$\kappa^2 = \mu^2 - \frac{\overline{k}_y^2}{\beta^2}; \mu = \frac{\overline{k}_x}{\beta}; \overline{k}_x^* M. \tag{2.39}$$

As a partial differential equation (PDE) problem, its nature is dependent on the sign of κ^2. If $\kappa^2 > 0$, the PDE is classified as a hyperbolic equation and the gust is named supercritical. For a supercritical gust, an initial perturbation is not seen at the same instant on all positions of the flow, but it is wave-likely propagated with constant and finite speed along characteristic lines. For negative values of κ^2, the PDE is classified as elliptical and the gust is subcritical. This gust type only contributes to the far-field for finite-span airfoils, since they produce fleeting waves (Santana, 2015).

The boundary conditions pointed by equations (2.27), (2.28) and (2.29) can be also represented by Fourier-type components (Christophe, 2011), so they can be rewritten as

$$\varphi(\overline{x}, 0) = 0 \qquad \overline{x} \le 0, \tag{2.40}$$

$$\frac{\partial \varphi}{\partial \overline{z}}(\overline{x}, 0) = \frac{-w_0 b}{\beta} e^{\overline{k}_x^* \overline{x}} \qquad 0 \le \overline{x} \le 2, \tag{2.41}$$

$$\left(i\overline{k}_x^* + \frac{\partial}{\partial \overline{x}} \right) \varphi(\overline{x}, 0) = 0 \qquad \overline{x} > 2. \tag{2.42}$$

2.4.1.3 Schwarzschild theorem

In the year 1901, Schwarzschild has described a problem of diffraction and polarization of the light through a gap (Schwarzschild, 1901). Mathematically, the problem consists of a canonical Helmholtz equation subjected to the boundary condition pair that follows:

$$\phi\left(x,0\right) = F\left(x\right) \qquad x > 0, \tag{2.43}$$

$$\frac{\partial \phi}{\partial z}\left(x,0\right) = 0 \qquad x < 0. \tag{2.44}$$

It is demonstrated by Schwarzschild that this problem has a solution ϕ given by

$$\phi\left(x,z\right) = \frac{1}{\pi}\int_0^\infty G\left(x,\xi,z\right) F\left(\xi\right) d\xi, \tag{2.45}$$

where G is the Green's function solution of the boundary value problem. It is a function that depends typically on the geometry of the problem and the perturbation frequency. The problem described by Schwarzschild refers to light diffraction, so the no-penetration condition is not satisfied by this procedure. Amiet suggests an iterative method that this condition can be satisfied together with one of the other two boundary conditions.

2.4.1.4 The Amiet strategy

The Amiet strategy for computing the airfoil response to a periodic gust consists of dividing the problem in sub-problems, by the appliance of the Schwarzschild method. In other words, it is a superimposition of solutions to the three boundary conditions two to two.

The first sub-problem consists on solving equation (2.37), subjected to the non-penetration boundary condition along the domain. After obtaining the flow potential, Amiet methodology suggests that, at the upstream region of the airfoil, the zero potential condition should be satisfied. Because of that, equation (2.37) should be solved with imposition of the equation (2.39) and the non-penetration boundary condition on the region downstream the airfoil leading edge. The third step is to satisfy the Kutta condition and the wake condition. To do so, the boundary condition of equation (2.32) is applied for the region downstream the airfoil trailing edge.

The non-penetration boundary condition has already been satisfied, since it is imposed.

2.4.1.5 First sub-problem: flow potential for an infinite plane

The Helmholtz equation can be solved verifying the non-penetration boundary condition on an infinite plane. By supposing that the flow potential is given by the relation

$$\varphi^{(0)}\left(\overline{x}, \overline{z}\right) = r e^{s\overline{x} - i\sqrt{\kappa^2 + s^2}\,\overline{z}}. \tag{2.46}$$

It is verified that this relation satisfies equation (2.20) if the coefficients are

$$s = -i\overline{k}_x{}^{*}; r = \frac{w_0 b}{\overline{k}}; \overline{k} = \sqrt{\overline{k}_x{}^2 + \overline{k}_y{}^2}. \tag{2.47}$$

The solution for the velocity potential is then given by

$$\varphi^{(0)}\left(\overline{x}, \overline{z}\right) = \frac{w_0 b}{\overline{k}} e^{-i\overline{k}_x{}^{*}\left(\overline{x} - \overline{k}\overline{z}/\beta\right)}. \tag{2.48}$$

2.4.1.6 Second sub-problem: LE correction

In the last section, the flow potential has been calculated considering the airfoil as an infinite plane. However, the second step of the iterative process takes into account the finite chord aspect of the airfoil. The airfoil is considered a semi-infinite plane extending downstream. In mathematical terms, a partial differential equation is written as:

$$\frac{\partial^2 \Psi_1}{\partial \overline{x}^2} + \frac{\partial^2 \Psi_1}{\partial \overline{z}^2} + \kappa^2 \Psi_1 = 0, \tag{2.49}$$

which is the convected Helmholtz equation. Its solution, at this step is given by using the Schwarzschild procedure considering the following boundary conditions,

$$\Psi_1\left(\overline{x}, 0\right) = -\varphi^{(0)}\left(\overline{x}, 0\right) \qquad \overline{x} \leq 0, \tag{2.50}$$

$$\frac{\partial \Psi_1}{\partial \overline{z}}\left(\overline{x}, 0\right) = 0 \qquad \overline{x} \geq 0, \tag{2.51}$$

where the equation (2.50) is the zero flow potential at the region upstream the leading edge and the equation (2.51) is the non-penetration boundary condition at the region downstream the airfoil leading edge. The solution for this boundary value problem is given by

$$\Psi_1\left(\overline{x}, 0\right) = \frac{w_0 b}{\overline{k}} e^{-i\overline{k}_x{}^{*}\overline{x}} \left(1 - (1-i) E\left[\overline{k}_x{}^{*} - \kappa\right]\overline{x}\right), \tag{2.52}$$

where E is a combination of Fresnel integrals as follow:

$$E\left(x\right) = C\left(x\right) + iS\left(x\right) = \int_0^x \cos t^2 dt + i \int_0^x \sin t^2 dt = \int_0^x \frac{e^{it}}{\sqrt{2\pi t}} dt. \tag{2.53}$$

It is noteworthy that further in this thesis, another combination of the Fresnel integral appears as the complex conjugate of E, i.e. $E^*(x)$. In order to avoid possible misconceptions for the reader, it is defined as

$$E^*(x) = C(x) - iS(x) = \int_0^x \cos t^2 dt - i \int_0^x \sin t^2 dt. \tag{2.54}$$

Downstream the airfoil leading edge, the flow potential $\varphi^{(1)}$ is given by the superimposition of the both flow potentials computed in each step, $\varphi^{(0)}$ and $\Psi^{(1)}$.

$$\varphi^{(1)}(\overline{x},0) = \varphi^{(0)}(\overline{x},0) + \Psi_1(\overline{x},0), \tag{2.55}$$

$$\varphi^{(1)}(\overline{x},0) = -\frac{w_0 b}{\overline{k}}\left(1 - E\left[\overline{k}_x{}^* - \kappa\right]\overline{x}\right)e^{-i\overline{k}_x{}^*\overline{x}} \tag{2.56}$$

Since the potential ϕ is given by equation (2.15), it can be written as

$$\phi^{(1)}(x,y,0,t) = \varphi^{(1)}(x,y,0,t)\,e^{i\omega t}e^{i\gamma x}e^{i\alpha x}, \tag{2.57}$$

$$\phi^{(1)}(x,y,0,t) = -\frac{w_0 b}{\sqrt{k_x^2 + k_y^2}}\left(1 - E\left[\overline{k}_x{}^* - \kappa\right]\overline{x}\right)e^{-i\overline{k}_x{}^*\overline{x}}e^{i\omega t}e^{i\gamma x}e^{i\alpha x}. \tag{2.58}$$

The disturbance pressure can be written as a function of the flow potential, as follows

$$p_1(x,y,0,t) = -\rho\frac{D\phi_1}{Dt} = -\rho\left(\frac{\partial \phi_1}{\partial t} + U\frac{\partial \phi_1}{\partial x}\right). \tag{2.59}$$

From the combination of equations (2.58) and (2.59), the disturbance pressure is derived and follows:

$$p_1(x,y,0,t) = -\rho U w_0 \frac{e^{-\pi/4}\left(\overline{k}_x{}^* - \kappa\right)}{\sqrt{\pi\left(\overline{k}_x{}^* - \kappa\right)\left(k_x^2 + k_y^2\right)}}e^{i\left(\omega t - \left[\frac{\left(\overline{k}_x{}^* - \kappa\right)}{b} - k_x\right]x - k_y y\right)}. \tag{2.60}$$

2.4.1.7 TE correction

After performing the leading edge correction, the next step is to consider the effect of the trailing edge on the airfoil response computation. First, the pressure computed on the previous section is space and time Fourier transformed:

$$p_1(x,y,0,t) = P_1(x,0)\,e^{i\omega t}e^{i\gamma x}e^{i\alpha x}. \tag{2.61}$$

The zero pressure jump condition at the airfoil wake, equation (2.42), should be satisfied. To do so, a correction pressure P_2 has to be computed on the region downstream the

trailing edge of the airfoil. A new boundary value problem is then stated as follows:

$$\frac{\partial^2 P_2}{\partial \overline{x}^2} + \frac{\partial^2 P_2}{\partial \overline{z}^2} + \kappa^2 P_2 = 0, \tag{2.62}$$

$$P_2\left(\overline{x}, 0\right) = -P_1\left(\overline{x}, 0\right) \qquad \overline{x} \geq 2, \tag{2.63}$$

$$\frac{\partial P_2}{\partial \overline{z}}\left(\overline{x}, 0\right) = 0 \qquad \overline{x} > 2. \tag{2.64}$$

The boundary value problem is solved applying the Schwarzschild procedure, i.e.:

$$P_2\left(\overline{x}, 0\right) = -\frac{1}{\pi} \int_0^\infty G\left(\overline{x} - 2, \xi, 0\right) P_1\left(2 + \xi, 0\right) d\xi. \tag{2.65}$$

Since this integral has no exact analytical solution, the following approximation is proposed (Christophe, 2005):

$$P_2\left(\overline{x}, 0\right) \approx \rho U w_0 \frac{e^{-i\pi/4} e^{-i\kappa\overline{x}}}{\sqrt{2\pi \left(\overline{k}_x^* - \kappa\right) \left(k_x^2 + \beta^2 \kappa^2\right)}} \left[1 - (1+i) E^*\left(2\kappa\left(2 - \overline{x}\right)\right)\right]. \tag{2.66}$$

Analogously to the computation of p_1(equation 2.60), p_2 is computed as

$$p_2\left(\overline{x}, 0\right) \approx$$

$$\rho U w_0 \frac{e^{-i\pi/4} \left(\overline{k}_x^* - \kappa\right)}{\sqrt{2\pi \left(\overline{k}_x^* - \kappa\right) \left(k_x^2 + \beta^2 \kappa^2\right)}} \left[1 - (1+i) E^*\left(2\kappa\left(2 - \overline{x}\right)\right)\right] e^{i\left[\left(\overline{k}_x^* M^2\right)\overline{x} - \pi/4 + \omega t - k_y y\right]}. \tag{2.67}$$

As it has been previously mentioned, the equations (2.66) and (2.67) are a function of the combination of Fresnel integrals E^*.

2.4.1.8   Aeroacoustics transfer functions

With the objective to compute sound generated aerodynamically, a relation between pressure jump and sound radiation has to be defined. Amiet established that

$$\Delta p\left(x, 0, t\right) = 2\pi \rho U w_0 g\left(x, k_x, k_y\right) e^{i\omega t}, \tag{2.68}$$

where the $g\left(x, k_x, k_y\right)$ is the called reduced lift function. As the airfoil thickness and the camber are considered negligible, the local lift is considered to be twice the pressure fluctuation. So, the reduced lift function is written as

$$g\left(x, k_x, k_y\right) = \frac{p\left(x, y, 0, t\right) e^{ik_y y} e^{-i\omega t}}{\pi \rho U w_0}. \tag{2.69}$$

To calculate the reduced lift function, the computed pressures after the leading edge and trailing edge corrections (equations 2.60 and 2.67) are needed, i.e.:

$$g_1\left(\overline{x}, k_x, k_y\right) = \frac{e^{-\pi/4}}{\pi\sqrt{2\pi\left(\overline{k}_x + \beta^2\kappa\right)\left(\overline{x}+1\right)}}e^{-i\left(\kappa - \overline{k}_x{}^*M^2\right)\left(\overline{x}+1\right)}, \tag{2.70}$$

$$g_2\left(\overline{x}, k_x, k_y\right) = -\frac{e^{-\pi/4}}{\pi\sqrt{2\pi\left(\overline{k}_x + \beta^2\kappa\right)}}\left[1 - (1+i)\,E^*\left(2\kappa\left(1-\overline{x}\right)\right)\right]e^{-i\left(\kappa - \overline{k}_x{}^*M^2\right)\left(\overline{x}+1\right)}. \tag{2.71}$$

The aeroacoustic transfer function for a supercritical gust is defined as

$$\mathcal{L}\left(x,y,z,k_x,k_y\right) = \int_{-1}^{1} g\left(\xi, k_x, k_y\right)e^{-i\mu(M-x/\sigma)\xi}d\xi, \tag{2.72}$$

where

$$\sigma = \sqrt{x^2 + \beta^2\left(y^2 + z^2\right)}. \tag{2.73}$$

Substituting g_1 and g_2 into equation (2.72), the aeroacoustics transfer functions $\mathcal{L}_1$ and $\mathcal{L}_2$ are derived:

$$\mathcal{L}_1\left(x,y,z,k_x,k_y\right) = \frac{1}{\pi}\sqrt{\frac{2}{\left(\overline{k}_x + \beta^2\kappa\right)\theta_1}}E^*\left(2\theta_1\right)e^{i\theta_2}, \tag{2.74}$$

$$\mathcal{L}_2\left(x,y,z,k_x,k_y\right) =$$
$$\frac{e^{i\theta_2}}{\theta_1\pi\sqrt{2\pi\left(\overline{k}_x + \beta^2\kappa\right)}}\left\{i\left(1 - e^{-2i\theta_1}\right) + (1-i)\left[E^*\left(4\kappa\right) - \sqrt{\frac{2\kappa}{\theta_3}}e^{-2i\theta_1}E^*\left(2\theta_3\right)\right]\right\}, \tag{2.75}$$

where

$$\theta_1 = \kappa - \frac{\mu x}{\sigma}, \theta_2 = \mu\left(M - \frac{x}{\sigma}\right) - \frac{\pi}{4}, \theta_3 = \kappa + \frac{\mu x}{\sigma}. \tag{2.76}$$

2.4.2 Turbulence aspects of the problem

Turbulent inflow noise is fundamentally based on the integral length scale L and the turbulent intensity I, in order to compute the noise spectra. In Amiet-based models, L and I are needed to define the turbulence velocity spectrum Φ_{ww}, the spectrum of vertical velocity fluctuations. Discussion of integral length scale modeling, as well as turbulence intensity modeling, is subject of this subsection, but other appropriate topic is about the PSD modeling.

2.4.2.1 Integral length scale and turbulence intensity

Discussions around integral length scale modeling are presented by many authors. The approach proposed by Moriarty and Migliore sets L as a function of distance from the ground up to a specific height, where is it then set constant (Moriarty and Migliore, 2003). For WT applications, the specific height is the hub height. This modeling follows:

$$L = \begin{cases} 0.7h & 0 \leq h \leq 60 \\ 42 & h > 60 \end{cases}.$$

(2.77)

Units are in meters.

On the other hand, Zhu *et al.* proposes an empirical expression, where L is a function of the hub height h and the surface roughness z_0, the latter varying for different terrain types (Zhu *et al.*, 2005), i.e.:

$$L = 25h^{0.35}z_0^{-0.063}.$$

(2.78)

A third alternative correlation to evaluate the integral length scale L was also presented by Boorsma and Schepers (Boorsma and Schepers, 2011) and is displayed

$$L = 2h\left(0.5 + 0.316\left(3 + \log_{10} z_0\right)\right).$$

(2.79)

Values of surface roughness z_0 can be seen in Table 2 as follows.

Table 2: Surface roughness for various terrain types

Terrain type	z_0 (m)
Very smooth, ice or mud	0.00001
Calm open sea	0.00020
Blown sea	0.0050
Snow surface	0.0030
Lawn grass	0.0080
Rough pasture	0.010
Fallow field	0.030
Crops	0.050
Few trees	0.100
Many trees, hedges	0.250
Forests and woodlands	0.500
Suburbs	1.500
Centers of cities with tall buildings	3.000

In the same manner, correlations for the turbulence intensity, I, are derived by Zhu *et al.* and Boorsma and Schepers as function of the WT hub height and surface roughness (Zhu *et al.*, 2005), (Boorsma and Schepers, 2011). The correlation provided by Zhu *et al.* follows:

$$I = \gamma \frac{\log_{10}\left(30/z_0\right)}{\log_{10}\left(h/z_0\right)}, \tag{2.80}$$

where γ is a power law factor, which gives the amount of shear between the flow mean velocity and the turbulence velocity fluctuations. The γ factor is estimated empirically by Couniham, with respect to Figure 25 (Couniham, 1975). The Couniham correlation follows

$$\gamma = 0.24 + 0.096 \log_{10}\left(z_0\right) + 0.016(\log_{10}\left(z_0\right))^2. \tag{2.81}$$
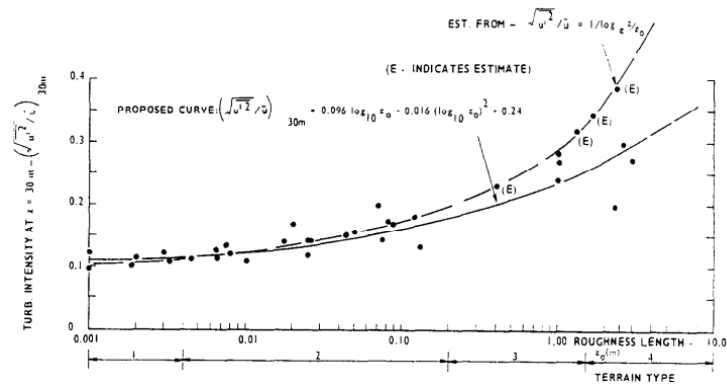
Figure 25: Variation of turbulence intensity with roughness length (Couniham, 1975)

.

The turbulence intensity approximation derived by Boorsma and Schepers based on ESDU standards (Boorsma and Schepers, 2011) and described as a fuction of hub height and terrain roughness follows

$$I = \frac{0.286 + 0.187 \log_{10} h - 0.081 (\log_{10} h)^2}{z_0^{0.07} \log_{10} h/z_0}. \tag{2.82}$$

A comparison of the three presented integral length scale estimation methods is displayed at Figure 26. It is noticeable that the three curves have no relation to each other, what represents that there is not yet a general unified vision of the problem.
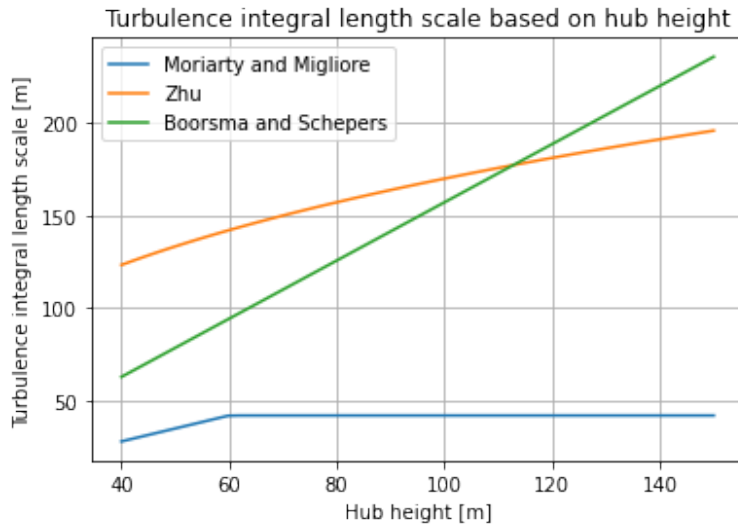
Figure 26: Comparison of three integral length scale estimation methods for lawn grass terrain

.

Despite being also different from each other, the estimation curves for the turbulence intensity, as it can be seen in Figure 27, present certain proximity when looking at usual WT hub height values, e.g. 80 m, the values differ in a range of 2%.
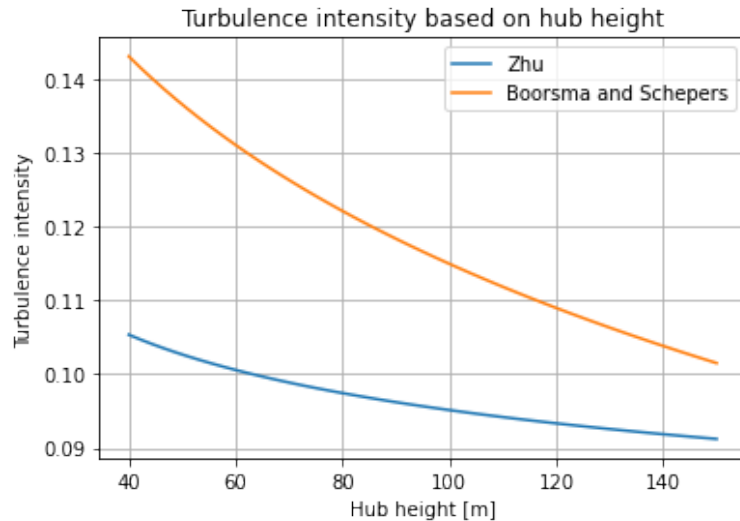
Figure 27: Comparison of two turbulence intensity estimation methods for lawn grass terrain

.

Since the difficulty to measure and validate turbulent inflow, these estimate models are yet open subject of discussion in the aeroacoustics community. However, the power spectral density can be analyzed by imposition of arbitrary pairs of turbulence intensity and integral length scale, since the LE noise prediction methods are not dependent on the WT structure, but depend only on airfoil geometry and flow conditions.

2.4.3 Turbulence velocity spectrum

Considering the hypothesis of homogeneous turbulence, the velocity spectrum tensor compose a Fourier-transform pair with the two-point velocity correlation as follows

$$\Phi_{ij}\left(\vec{k}\right) = \frac{1}{(2\pi)^3} \iiint\limits_{-\infty}^{\infty} R_{ij}\left(\vec{r}\right) e^{-i\vec{k}\cdot\vec{r}} d\vec{r}, \tag{2.83}$$

$$R_{ij}\left(\vec{r}\right) = \iiint\limits_{-\infty}^{\infty} \Phi_{ij}\left(\vec{k}\right) e^{i\vec{k}\cdot\vec{r}} d\vec{k}, \tag{2.84}$$

where $\vec{k} = \{k_x, k_y, k_z\}$ is the continuous wavenumber vector. In order to abbreviate the notation, the dependencies of Φ_{ij} and R_{ij} on time are not shown explicitly.

The information contained in $\Phi_{ij}(\vec{k})$ can be considered in three parts. First, the subscripts i and j give the directions of the velocity in physical space. For example, let us consider $\Phi_{ww}(k_x, k_y, k_z)$, which pertains entirely to the velocity fluctuation field $u_w(\vec{x})$. Second, the wavenumber direction $\vec{k}/|\vec{k}|$ gives the direction of the Fourier mode in the physical space. At last, the wavenumber's magnitude determines the length scale of the mode $l = 2\pi/|\vec{k}|$. A simpler, and more usual description of the turbulence behavior is provided by the energy spectrum function $E(k)$, which is a scalar function of a scalar quantity k, which corresponds to the magnitude $|\vec{k}|$.

The energy spectrum function is obtained by eliminating the directional information of $\Phi_{ij}\left(\vec{k}\right)$. This can be made first by considering half of the trace of the second order tensor, i.e., $\frac{1}{2}\Phi_{ii}\left(\vec{k}\right)$. Then, to remove the directional information of the Fourier modes, a integration over all wavenumbers $\vec{k}$ of magnitude $|\vec{k}| = k$ is performed. This is mathematically expressed by representing the spherical wavenumber space $S(k)$, centered at the origin, with radius k. The energy spectrum function is defined as

$$E(k) = \oint \frac{1}{2}\Phi_{ii}(\vec{k})dS(k). \tag{2.85}$$

The following subsections discuss hypothesis, modeling and derivation of turbulence velocity spectra, utilizing the energy spectrum function as a starting point. In these cases, the inverse process should be performed. For the purpose of exemplification, let us consider the case of isotropic turbulence. In this specific case, the directional information in $\Phi_{ij}(\vec{k})$ depend only on $(\vec{k})$, and, to within scalar multiples, the only second order tensors that can be formed from $\vec{k}$ are δ_{ij} and $k_i k_j$. For isotropic turbulence, consequently, $\Phi_{ij}(\vec{k})$ is given by

$$\Phi_{ij}(\vec{k}) = A(k)\delta_{ij} + B(k)k_i k_j, \tag{2.86}$$

where $A(k)$ and $B(k)$ are scalar functions of k. Being the turbulence velocity spectrum tensor function of the energy spectrum, for isotropic turbulence it yields

$$\Phi_{ij}(\vec{k}) = \frac{E(k)}{4\pi k^2}\left(\frac{k_i k_j}{k^2}\right), \tag{2.87}$$

where one can define the projection tensor $P_{ij}(\vec{k}) = \left(\frac{k_i k_j}{k^2}\right)$.

Under the assumption of $\Phi_{ij}(\vec{k})$ being analytic at the origin, the energy spectrum function $E(k)$ varies with k^4 for small values of k.

From now, two distinct and well-defined situations take place, regarding the airfoil turbu-

lent inflow noise prediction. Different from the BPM TBL-TE noise prediction method, which is based on local flow conditions, but mostly dependent on the mean flow, Amiet-based LE noise prediction methods depend on local inflow turbulence. That means acoustic tunnel measurements will hardly match with field measurements for the turbulent inflow noise and vice-versa, given that neither atmospheric turbulence integral length scale, nor its respective velocity spectrum are likely to be reproduced by grid-turbulence.

2.4.3.1 Von Kármán turbulence spectrum model

When setting up the aeroacoustic tunnel experiment, Amiet has observed that, in the test section of the UARL tunnel, the grid-generated turbulence approached a condition near an isotropic turbulence, in the absence of the airfoil. In this case, as well as in many other studies, authors observe a good agreement with the von Kármán spectrum model. From the definition of the energy spectrum function,

$$E(k) = C\varepsilon^{2/3}k^{-5/3}f_L(kL)f_\eta(k\eta), \tag{2.88}$$

where f_L and f_η are specified non-dimensional functions. The function f_L determines the shape of the energy-containing range, and tends to unity for large kL. Similarly, f_η determines the shape of the dissipation range, and tends to unit for small $k\eta$. The function f_L, for the von Kármán spectrum, follows

$$f_L(kL) = \left(\frac{kL}{[(kL)^2 + c_L]^{1/2}}\right)^{17/3}, \tag{2.89}$$

where c_L is a positive constant. Combination of Equations (2.88) and (2.89) suggests that $E(k) \sim k^4$, as stated in the beginning of this subsection.

Another important characteristic, verified from Equation (2.88) is that von Kármán spectrum decays with the wavenumber following a $-5/3$ asymptotic power law. From Amiet (1975), this reduces to

$$E(k) = \frac{Bk^4}{[1 + (k/k_e)^2]^{17/6}}, \tag{2.90}$$

where $B = \frac{55}{9\sqrt{\pi}}\frac{\Gamma(5/6)}{\Gamma(1/3)}\frac{\overline{u^2}}{k_e^5}$. The quantity $\overline{u^2}$ is evaluated by taking the root mean square of the turbulence fluctuations and can be represented in terms of the turbulence intensity I and the mean flow velocity U as

$$\overline{u^2} = (IU)^2. \tag{2.91}$$

The average wavenumber of the energy-containing eddies, k_e, is defined in terms of the integral length scale of turbulence, L, and the gamma functions $\Gamma(5/6)$ and $\Gamma(1/3)$ as

$$k_e = \frac{\sqrt{\pi}}{L} \frac{\Gamma(5/6)}{\Gamma(1/3)}. \tag{2.92}$$

As a function of the wavevector components, the energy spectrum, $\Phi_{ww}(k_x, k_y, k_z)$, of the vertical velocity fluctuations is related to $E(k)$ by

$$\Phi_{ww}(k_x, k_y, k_z) = \frac{E(k)}{4\pi k^2} \left(1 - \frac{k_z^2}{k^2}\right). \tag{2.93}$$

By integration over k_z, the two-wavenumber von Kármán energy spectrum $\Phi_{ww}(k_x, k_y)$ is obtained as

$$\Phi_{ww}(k_x, k_y) = \frac{4}{9\pi} \frac{\overline{u^2}}{k_e^2} \frac{(k_x/k_e)^2 + (k_y/k_e)^2}{\left(1 + (k_x/k_e)^2 + (k_y/k_e)^2\right)^{7/3}}. \tag{2.94}$$

Note that this condition, described by the turbulent energy spectrum of Equation (2.94), is nearly obtained in the test section of wind or acoustic tunnels, with grid-generated turbulence, in the absence of the airfoil, which is a situation much different than atmospheric turbulence approaching a rotating blade, or even a stationary airfoil interacting with turbulent eddies. It is a "no-airfoil" condition instead. In some cases, which will be further detailed in the next subsection, the eddies tend to rapidly distort while approaching the airfoil leading-edge, thus causing a distancing from the homogeneous and isotropic approximation.

The following topic introduces another perspective regarding modeling of the turbulence energy spectrum, and consequently the turbulence energy spectrum other than von Kármán homogeneous and isotropic spectrum.

2.4.3.2   Rapid distortion theory (RDT)

The discussion on the effect of rapid distortion of a fluid in turbulent motion has been addressed for quite a long time, after Batchelor and Proudman try to describe the changes produced in a homogeneous turbulent flow, when the fluid is itself subjected to a superimposed uniform distortion. The distortion occurs so rapidly that the contribution to the change in relative position of the fluid particles of turbulence is negligible (Batchelor and Proudman, 1954).

In Batchelor and Proudman study, turbulence was seen to behave initially isotropic and the eddies begin to distort while approaching a solid structure, such as a wall or an airfoil, which its characteristic length is larger than the largest turbulent structure, as in Amiet's experiment. In other words, turbulence rapid distortion takes place when a variation in

the mean velocity occurs in response to a change in the boundary conditions.

As later reported by Kevlahan, the rapid distortion can also be produced on the flow by the larger turbulence structures, that can either induce rotational or irrotational distortion in the smaller eddies (Kevlahan, 1993).

The discussion on rapid distortion theory and turbulent inflow noise was introduced by Simonich *et al.*, when describing the velocity field and spectrum of turbulence undergoing a rapid distortion (Simonich *et al.*, 1986) for helicopter rotor noise analysis. In their article, the criteria for application of RDT, introduced by Hunt (1978), and revisited by Goldstein (2013), are well established and can be summarized as follows:

- The turbulence intensity should be much smaller than the unit, i.e.:

$$I = \frac{u^{'}}{U} << 1;$$ (2.95)

- The length scale is short, when compared to the length scale over which the turbulent eddies evolve, i.e.:

$$\frac{L}{L_C} < 1,$$ (2.96)

where L_C is the characteristic length of the solid surface, e.g. an airfoil chord;

- The Reynolds number associated with the turbulence should be large, i.e.:

$$\frac{u^{'} L}{\nu} >> 1.$$ (2.97)

For the purpose of this thesis, as for Simonich *et al.* (1986), the three criteria may be fulfilled in order to ensure that rapid distortion will take place and be dominant.

Proceeding to the description of the turbulence energy spectrum, PIV experimental measurements conducted by Santana (2015), have confirmed the asymptotic decays of the Φ_{ww}, as proposed by Hunt (1973). That means, when small scale turbulence approximates to the wall, the turbulence energy spectrum decays following a $-10/3$ asymptotic at high frequencies, instead of following the $-5/3$ power law as for smaller wavenumbers. In addition to that, research conducted by Christophe proposes a modification to the exponent of the turbulence energy spectrum, which corresponds to modifying the hypothesis of undistorted homogeneous and isotropic turbulence to the anisotropic distorted case. This modification changes the exponent of the turbulence energy spectrum from $17/6$ to $22/6$ (Christophe, 2011). By incorporating these changes, one can write the turbulence energy spectrum as

$$E\left(k\right) = \frac{C\overline{u^2}k^4}{k_e^5\left[1 + (k/k_e)^2\right]^{22/6}},$$ (2.98)

which is still proportional to k^4 for small k, as the von Kármán spectrum. This indicates that the RDT spectrum can be also analytically determined in the origin.

The coefficient C should be defined in order to satisfy the following relation,

$$\int_0^\infty E\left(k\right) dk = \frac{3}{2}\overline{u^2}. \tag{2.99}$$

By adopting the same procedure of the last subsection, the correspondent modified turbulent energy spectrum is derived analogously and it can be written as follows

$$\Phi_{ww}\left(k_x, k_y\right) = \frac{91}{36\pi}\frac{\overline{u^2}}{k_e^2}\frac{\left(k_x/k_e\right)^2 + \left(k_y/k_e\right)^2}{\left(1 + \left(k_x/k_e\right)^2 + \left(k_y/k_e\right)^2\right)^{19/6}}. \tag{2.100}$$

In order to illustrate the difference between the anisotropic distorted turbulence spectrum and the homogeneous and isotropic von Kármán turbulence spectrum, let us consider the generic case of an airfoil under a turbulent flow with $M = 0.12$, $I = 4\%$, $L = 0.03 \; m$. As it may be seen in Figure 28, the energetic content of the anisotropic turbulence spectrum is much higher than the isotropic at the lower frequencies, having a greater order of magnitude. For those specific flow conditions, at frequencies higher than 425 Hz, the energetic content of the isotropic turbulence surpasses the anisotropic turbulence energetic content, until both tend to zero. This may point out to a possible increase on the predicted $SPL_{1/3}$ at lower frequencies and a decrease on the higher.
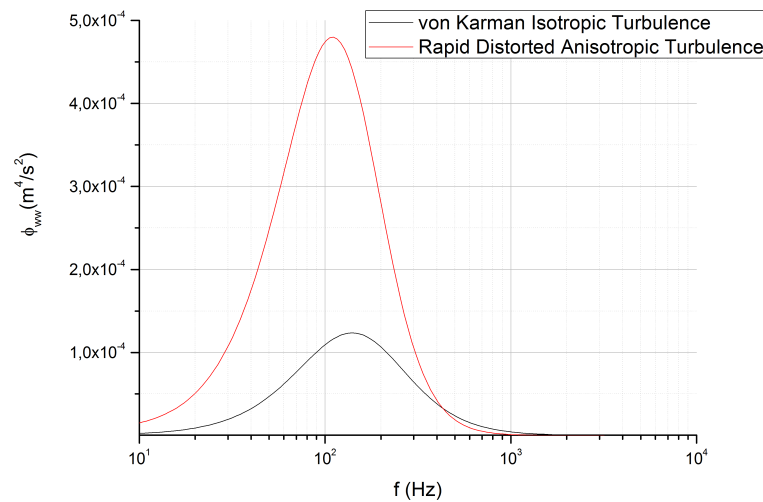
Figure 28: Comparison between von Kármán homogeneous and isotropic turbulence spectrum and the RDT anisotropic turbulence spectrum.

2.4.4 Amiet semi-empirical method for turbulent inflow noise prediction

Figure 29 is a representation of Amiet experimental setup. An airfoil with a 18 inches chord and a 21 inches span was mounted between sideplates at zero AoA in the UARL (United Aircraft Research Laboratories) acoustic facility. A turbulence induction grid was placed upstream the airfoil. The turbulence measurements without the airfoil in the test section have indicated at the test section that turbulence properties were near isotropic and well approximated by the von Kármán isotropic and homogeneous turbulence model.
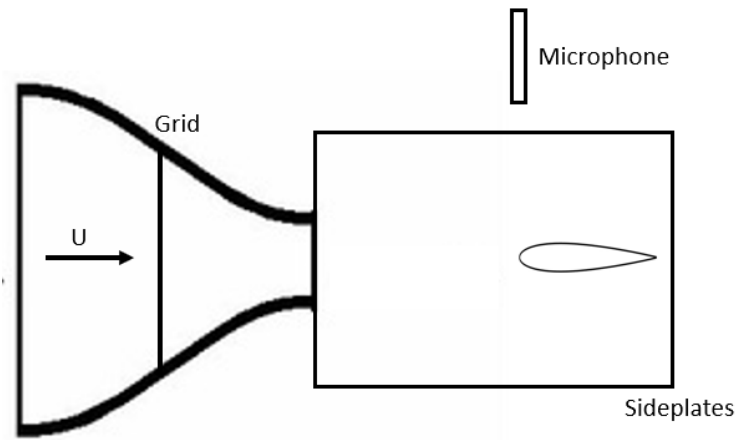
Figure 29: Schematic of the experimental facility for aeroacoustics investigation.

The measured integral length scale, L, of the turbulence was 1.25 inches. The streamwise turbulence intensity, I, was set to 4.4% for $U = 103$ ft/s. For higher velocities, the intensity of turbulence followed approximately the expression

$$I = CU^{-0.2}. \tag{2.101}$$

Amiet conducted third octave sound measurements with a microphone placed at 7 feet directly above the airfoil and obtained a semi-empirical relation for the one third octave level, $SPL_{1/3}$, in dB relative to a pressure of $2 \cdot 10^{-4}$ μbar

$$SPL_{1/3} = 10 \log_{10} \left[\frac{sL}{2z^2} M^5 \frac{\overline{u^2}}{U^2} \frac{(k_x/k_e)^3}{\left(1 + (k_x/k_e)^2\right)^{7/3}} \right] + 181.3. \tag{2.102}$$

Equation (2.102) can be derived after equations (2.26) and (2.94), by considering only parallel gusts ($k_y = 0$) and the lift transfer function, $\mathcal{L}$, is approximated to the unit. Besides that, the observer position is described only in the z direction. Constant values

such as sound velocity and density are incorporated to the constant of 181.3 dB.

It is important to draw attention here for the units of measure, that may influence the total SPL, because, since Amiet experiment was conducted considering the British system of units, the 181.3 dB constant may be biased by that system.

Although showing good agreement to a range of frequencies, which extended from 500 Hz up to 2500 Hz, the experiment was not conducted for any lower range of frequencies because of limitations of the test chamber. Since turbulent inflow noise is characterized as a low frequency noise mechanism, its correspondent prediction methods should be effectively validated for a wider range, that contemplate frequencies below that 500 Hz mark, which, in terms of the overall airfoil noise, is also influenced by the self-noise source, not only the turbulence interaction source.

2.4.5   Paterson and Amiet semi-empirical method

Paterson and Amiet have discussed further development on representing the experiment for a stationary airfoil in an open-jet acoustic tunnel as being measured by a stationary observer outside the open-jet shear layer and directly above the airfoil leading-edge (Paterson and Amiet, 1977). In order to represent accurately the whole frequency spectrum, not being limited to frequencies above 500 Hz anymore, as in the case of Amiet investigation (Amiet, 1975), two different regimes were considered, and two semi-empirical expressions were given. One for high frequency and other for low frequency regimes. To do so, first, a parameter μ is defined,

$$\mu = \frac{M k_x c}{2\beta^2},\tag{2.103}$$

where $\beta = \sqrt{1 - M^2}$ is the Prandtl-Glauert compressibility correction. For the low frequency regime, i.e. $\mu < \frac{\pi}{4}$, the following expression applies

$$SPL_{1/3} = 10 \log_{10} \left[S^2 \frac{M^6}{\beta^2} \overline{k}_x^2 \frac{sL}{2z^2} I^2 \rho_0^2 c_0^4 \frac{(k_x/k_e)^3}{\left(1 + (k_x/k_e)^2\right)^{7/3}} \right] + 68.4,\tag{2.104}$$

where S is the compressible Sears function (Paterson and Amiet, 1977) represented by

$$S^2 \quad = \quad \left(\frac{2\pi\,(\overline{k_x})}{\beta^2} + \left(1 + 2.4\frac{(\overline{k_x})}{\beta^2} \right)^{-1} \right)^{-1},\tag{2.105}$$

with $\overline{k_x} = \frac{k_x c}{2}$. For the high frequency regime, on the other hand,

$$SPL_{1/3} = 10 \log_{10} \left[\frac{\rho_0^2 c_0^4 s L}{2 z^2} M^5 \frac{\overline{u^2}}{U^2} \frac{(k_x/k_e)^3}{\left(1 + (k_x/k_e)^2\right)^{7/3}} \right] + 78.4. \qquad (2.106)$$

Different from Amiet's original semi-empirical method (Amiet, 1975), which can be seen at equation (2.102), these expressions from Paterson and Amiet are derived for the CGS unit system (Paterson and Amiet, 1977).

2.4.6   Lowson's semi-empirical method

In a similar fashion to Paterson and Amiet, Lowson has proposed to characterize the low frequency regime as an additional correction to the high frequency regime. So, without the need for two specific expressions, one can write after Lowson (Lowson, 1992)

$$SPL_{1/3} = SPL_H + 10 \log_{10} \left[\frac{LFC}{1 + LFC} \right], \qquad (2.107)$$

where SPL_H is an improved version of equation (2.102) as follows

$$SPL_H = 10 \log_{10} \left[\frac{\rho_0^2 c_0^2 s L}{2 r_e^2} M^3 U^2 I^2 \frac{(k_x/k_e)^3}{\left(1 + (k_x/k_e)^2\right)^{7/3}} \overline{D_L} \right] + 78.4. \qquad (2.108)$$

One of the most important features of Lowson's expression is the inclusion of the spherical directivity, D_L. Because of that, the observer position is no longer limited to be orthogonal to the airfoil leading edge. It has made possible for one to use semi-empirical formulations to predict wind turbine noise, among other applications. The directivity is expressed in terms of sine and cosine functions, i.e.:

$$\overline{D_L} = \frac{\sin^2 \theta \cos^2 \varphi}{(1 + M \cos \varphi)^4}. \qquad (2.109)$$

The low frequency correction factor is written in terms of the compressible Sears function and other flow conditions as

$$LFC = 10 S^2 M \overline{k_x}^2 \beta^{-2}. \qquad (2.110)$$

There are no mentions to the system of units employed by Lowson (Sucameli, 2017), but seeing that it is an improvement of Paterson and Amiet formulation, and that the constant values from Equation (2.106) and Equation (2.108) are equal to each other, one can conclude that both are derived in the CGS unit system.

Studies from Moriarty *et al.* and Buck *et al.* incorporate the dependency effects of finite angle of attack to the LFC term (Moriarty *et al.*, 2004, Buck *et al.*, 2018), so it can be

written in a more complete way,

$$LFC = 10S^2 \left(1 + 9\alpha^2\right) M\overline{k_x}^2 \beta^{-2},$$ (2.111)

with α in radians.

This final form of Lowson's classical turbulent inflow noise prediction method appears to be still the most suitable semi-empirical method for inclusion in *PNoise*, due to its similarities with respect to the NASA BPM method, such as the spherical directivity, presented in Equations (2.108) and (2.109), and the modification presented for attending a finite AoA range as seen in Equation (2.111). At this point, however, given its characteristics of being based on a homogeneous and isotropic turbulence assumption, further modification may be discussed.

2.4.7   RDT-Modified Lowson method

After the suggestions from Roger and Moreau (2010), Tian and Cotté (2016), Buck *et al.* (2018) and Zhong and Zhang (2019), the RDT effects on the airfoil turbulent inflow noise prediction are embedded into Lowson's semi-empirical method. In order to derive this modification, let us first expand the constant 78.4 from Equation (2.108), using basic logarithmic properties. It results in

$$SPL_H = 10 \log_{10} \left[691830.98 \frac{\rho_0^2 c_0^2 sL}{2r_e^2} M^3 U^2 I^2 \frac{(k_x/k_e)^3}{\left(1 + (k_x/k_e)^2\right)^{7/3}} \overline{D_L} \right].$$ (2.112)

One then should be able to identify the terms of the turbulence spectrum Φ_{ww} relative to the von Kármán homogeneous and isotropic turbulence, from Equation (2.87). The substitution of the turbulence model by the rapid distorted spectrum, from Equation (2.97), leads to an alternative SPL'_H, i.e.:

$$SPL'_H = 10 \log_{10} \left[3934788.65 \frac{\rho_0^2 c_0^2 sL}{2r_e^2} M^3 U^2 I^2 \frac{(k_x/k_e)^3}{\left(1 + (k_x/k_e)^2\right)^{19/6}} \overline{D_L} \right].$$ (2.113)

Or, by writing as Equation (2.108),

$$SPL'_H = 10 \log_{10} \left[\frac{\rho_0^2 c_0^2 sL}{2r_e^2} M^3 U^2 I^2 \frac{(k_x/k_e)^3}{\left(1 + (k_x/k_e)^2\right)^{19/6}} \overline{D_L} \right] + 85.95.$$ (2.114)

It is noteworthy that the only change here is in the turbulence spectrum model. All other variables and the unit system are kept the same as in the original Lowson's method.

2.4.8   Final remarks

There is indeed a lack of experimental data for validating airfoil noise prediction methods, as observed by Saab (Saab, 2016). In the specific case of the turbulent inflow noise, it is not different. An aggravating factor is that the available data from the literature is not representative of real WT conditions, whether the airfoil thickness, or the turbulent flow conditions, which are both different from the wind turbine blades thickness and operational Reynolds, Mach numbers and turbulence structures. Seeing this as a limitation of the validation process, not of the prediction method, this study follows the same protocol as from the NASA BPM (Brooks, Pope and Marcolini, 1989) among others, making clear the current validity range of the method and setting up an inviting environment for continuous improvement and further validation. The validation schedule will follow the steps:

- Validation of the 2D airfoil turbulent inflow noise prediction methods against acoustic tunnel measurement data.

- Discussion on real airfoil effects and the necessity of a thickness correction.

- Validation of the 2D airfoil turbulent inflow noise prediction methods for representation of full scale WT units.

3   ISOLATED AIRFOIL MEASUREMENTS

This chapter main focus is to investigate the validity of the previously discussed airfoil turbulent inflow noise prediction methods. This is made by comparing the standard and the modified Lowson formulations with experimental data gathered from recent literature, i.e. the studies by Bampanis *et al.* (2019), Juknevicius and Chong (2018) and Narayanan and Singh, in both visual and statistical aspects.

To accomplish this objective, the Lowson method equations considering isotropic turbulence and the rapidly distorted spectrum (equations 2.107 and 2.108 and2.114) are written as *Python* language scripts, for purpose of validation. Later, the scripts will be transposed to $C++$ language to be suited for integration in QBlade.

The frequency range of the validation is based on the experimental measurements (tipically from 100 to 10000 Hz). The statistical analysis takes in consideration the overall sound pressure level, which is the integral of the sound pressure level curve, or the log summation of the 1/3 Octave SPL values, i.e. the log summation of the sound pressure level evaluated at 100, 125, 160, 200, 250, 315, 400, 500, 630, 800, 1000, 1250, 1600, 2000, 2500, 3150, 4000, 5000, 6300, 8000 and 10000 Hz, and the respective root mean square error.

3.1   Experimental setup and modeling

The mentioned authors have conducted airfoil leading-edge noise measurements as represented in figure 29 in the context of investigating whether the use of serrations attached to the airfoil leading-edge or using airfoils with a serrated LE contribute on reducing the turbulent inflow noise. The two studies start from unmodified baseline airfoils, which are identified as the relevant cases for the present validation. Furthermore, both experimental analysis were performed at three different flow velocities each, and that can qualify the validation in terms of a range of Mach-Reynolds numbers. Nevertheless, the studies are conducted for airfoils with maximum relative thickness of 8%. This, in addition to the range of Mach-Reynolds pairs, may represent significant drawbacks to

the present validation, at least for being representative of a realistic wind turbine noise emission.

The experimental setups relative to both studies follow, in ascending order of airfoil relative thickness and flow velocities:

- Bampanis *et al.* have performed measurements with a microphone positioned $1\ m$ orthogonal to the airfoil leading-edge, in the mid-span position. An A-filtered SPL spectrum, in dBA, was captured for a flat-plate airfoil with relative thickness of 3% with a chord length $c = 0.10\ m$ and span $s = 0.30\ m$, subjected to mean flow velocities $U = 19\ m/s$, $U = 27\ m/s$ and $U = 32\ m/s$. The measured turbulence intensity and the turbulent eddies integral length scale near the airfoil leading edge position were $I = 0.045\%$ and $L = 0.009\ m$ respectively. These parameters were obtained prior to the experiment, in the absence of the airfoil, where a near isotropic behavior of the turbulence is observed, and well represented by the von Kármán isotropic turbulence spectrum model (Bampanis *et al.*, 2019);

- Juknevicius and Chong, in their turn, have conducted similar measurements for a NACA 0008 airfoil with a chord length $c = 0.15\ m$ and span $s = 0.498\ m$, placing a microphone at a $1.25\ m$ distance orthogonal to its leading-edge. The turbulence intensity and the turbulent eddies integral length scale near the airfoil leading edge were, respectively, $I = 0.037$ and $L = 0.0065\ m$, once again in the absence of the airfoil. This leads to the observation of a near isotropic turbulence, well suited by the von Kármán spectrum. The mean flow velocities were $U = 30\ m/s$, $U = 50\ m/s$ and $U = 60\ m/s$ (Juknevicius and Chong, 2018);

- Narayanan and Singh, at last, have conducted similar measurements for a NACA 65 airfoil with relative thickness of 12% with a chord length $c = 0.15\ m$ and span $s = 0.45\ m$, placing a microphone at a $1.2\ m$ distance orthogonal to its leading-edge. The turbulence intensity and the turbulent eddies integral length scale near the airfoil leading edge were, respectively, $I = 0.025$ and $L = 0.006\ m$, once again in the absence of the airfoil. This leads to the observation of a near isotropic turbulence, well suited by the von Kármán spectrum. The mean flow velocities were $U = 40\ m/s$, $U = 60\ m/s$ and $U = 80\ m/s$ (Narayanan and Singh, 2020).

Having the three experimental setups described, the validation range can be estimated as $1.3 \cdot 10^5 < Re < 8.11 \cdot 10^5$ and $0.056 < M < 0.235$. For a better representation of the experimental setup, its main parameters are summarized at table 3.

Table 3: Experimental setup and flow conditions

	Airfoil profile	c	s	Relative thickness	U	L	I
Bampanis *et al.*, 2019	Flat-plate	0.10 m	0.3 m	3%	19 m/s	0.009 m	0.045
					27 m/s	0.009 m	0.045
					32 m/s	0.009 m	0.045
Juknevicius and Chong, 2018	NACA 0008	0.15 m	0.498 m	8%	30 m/s	0.0065 m	0.037
					50 m/s	0.0065 m	0.037
					60 m/s	0.0065 m	0.037
Narayanan and Singh, 2020	NACA 65	0.15 m	0.45 m	12%	40 m/s	0.006 m	0.025
					60 m/s	0.006 m	0.025
					80 m/s	0.006 m	0.025

Before the implementation in the *QBlade/PNoise* environment, a computational script was developed in *Python* language as a testing platform for the discussed TI noise prediction methods. The standard Lowson method (equations 2.107 and 2.108) and its RDT-modified counterpart (equations 2.107 and 2.114) were defined as callable functions in terms of frequency, airfoil chord and span, mean flow velocity, turbulence intensity and integral length scale and the spherical directivity parameters, i.e. distance and angles. Such script allowed agile qualitative and quatitative assessment of each of the compared prediction methods.

3.2   RDT criteria verification step

As stated in the experimental setup description, in both Juknevicius and Chong (2018) and Bampanis *et al.* (2019), turbulence has presented a good agreement with von Kármán isotropic velocity spectrum at the leading-edge location, as obtained by hot-wire measurements in the absence of the airfoil. However, it can be demonstrated that, interacting with the airfoil, the *RDT* criteria from section 2.4.3.2 (equations 2.95, 2.96 and 2.97) are met by any of the flow conditions from Bampanis *et al.* (2019) and Juknevicius and Chong (2018), as table 4 evidences.

From an accurate analysis of the input data, the larger turbulence scales are shown to be small enough to experience rapid distortion while approaching the airfoil surface in every studied case. Besides that, such high turbulent Reynolds numbers $\frac{IUL}{\nu}$ indicate that leading-edge noise source plays a significant role in the airfoil noise assessment.

Table 4: *RDT* criteria verification

	I	L/c	$\frac{IUL}{\nu}$	Meets the criteria for RDT?
Bampanis *et al.*, 2019	0.045	0.09	509.27	Yes
			723.69	Yes
			857.71	Yes
Juknevicius and Chong, 2018	0.037	0.04333	477.49	Yes
			795.83	Yes
			955.0	Yes
Naraynan and Singh, 2020	0.025	0.04	405.40	Yes
			608.11	Yes
			810.81	Yes

3.3 Turbulent inflow noise prediction

The *Python* scripts were run for each one of the setups presented at table 3. From that, nine plots were obtained, three for Bampanis *et al.* conditions, three for Juknevicius and Chong experiment and the last set of three for Narayanan and Singh study. The predicted noise spectrum is plotted at the same chart as the measured data gathered from these authors manuscripts and are depicted at figures 30, for Bampanis *et al.*, 31, for Juknevicius and Chong, and 32 for Narayanan and Singh.
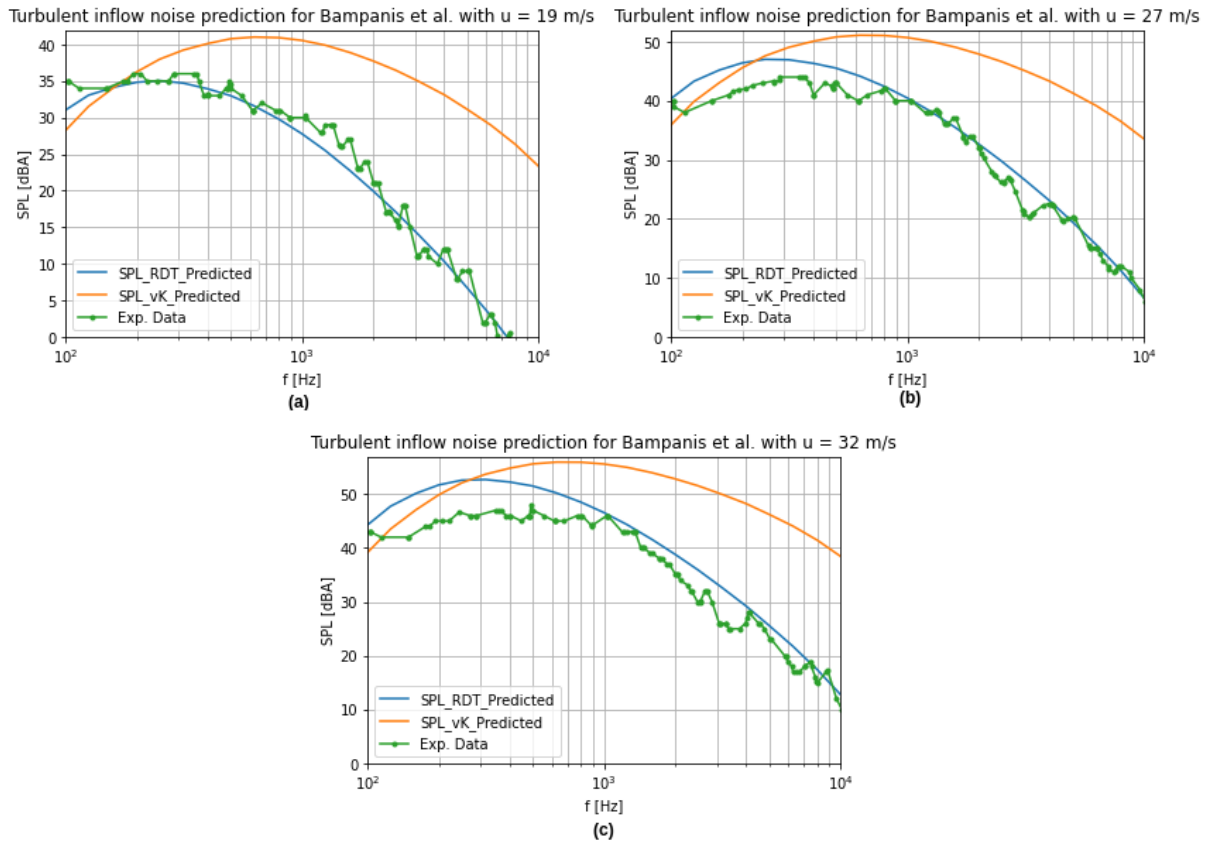
Figure 30: Comparison between the A-filtered turbulent inflow noise experimental data (green lines with dots) collected by Bampanis *et al.* (2019) and the predicted curves for the standard Lowson method, considering von Kármán isotropic turbulence (orange solid curves), and the *RDT*-modified Lowson method (blue solid curves). The flow regimes refer to table 29, where (a) stands for $U = 19 \ m/s$, (b) represents $U = 27 \ m/s$ and (c) denotes $U = 32 \ m/s$.
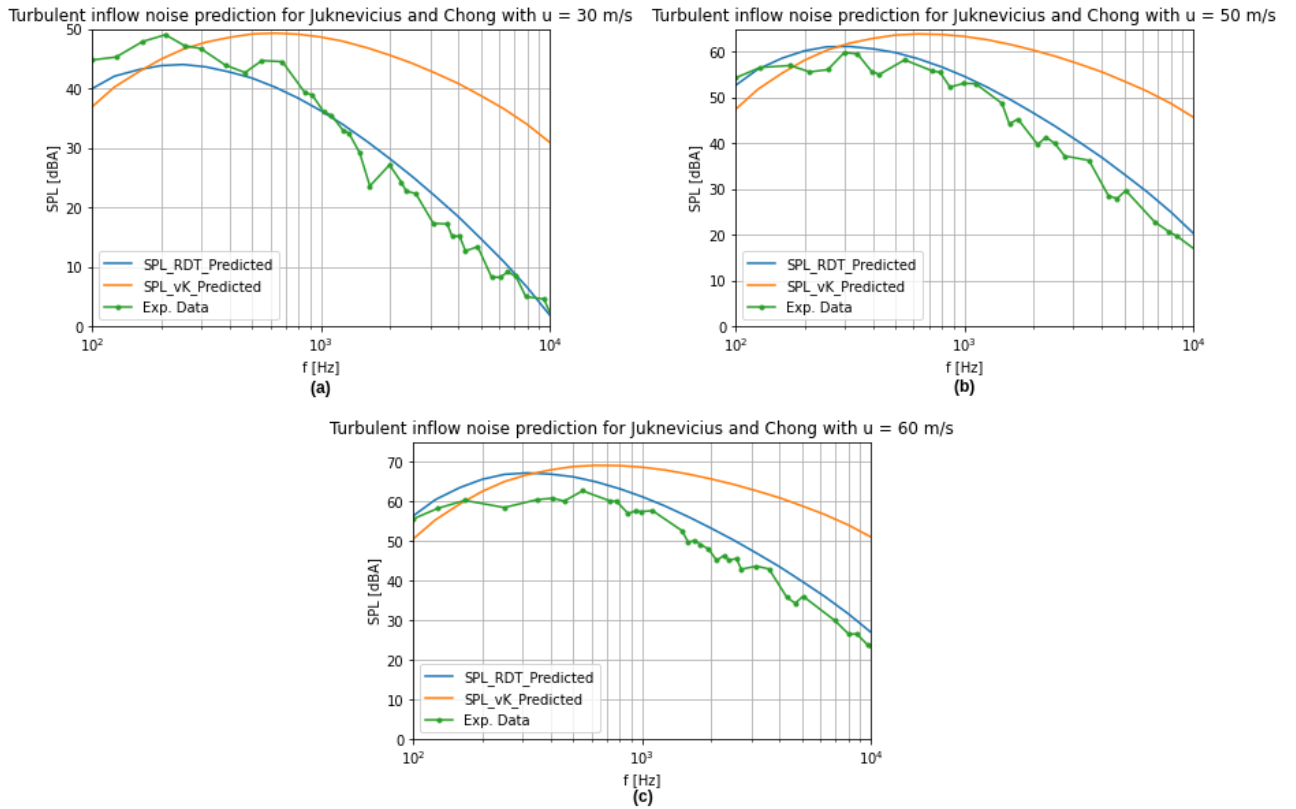
Figure 31: Comparison between the A-filtered turbulent inflow noise experimental data (green lines with dots) measured by Juknevicius and Chong (2018) and the predicted curves for the standard Lowson method, considering von Kármán isotropic turbulence (orange solid curves), and the RDT-modified Lowson method (blue solid curves). The flow regimes refer to table 29, where (a) stands for $U = 30\ m/s$, (b) represents $U = 50$ m/s and (c) denotes $U = 60\ m/s$

.
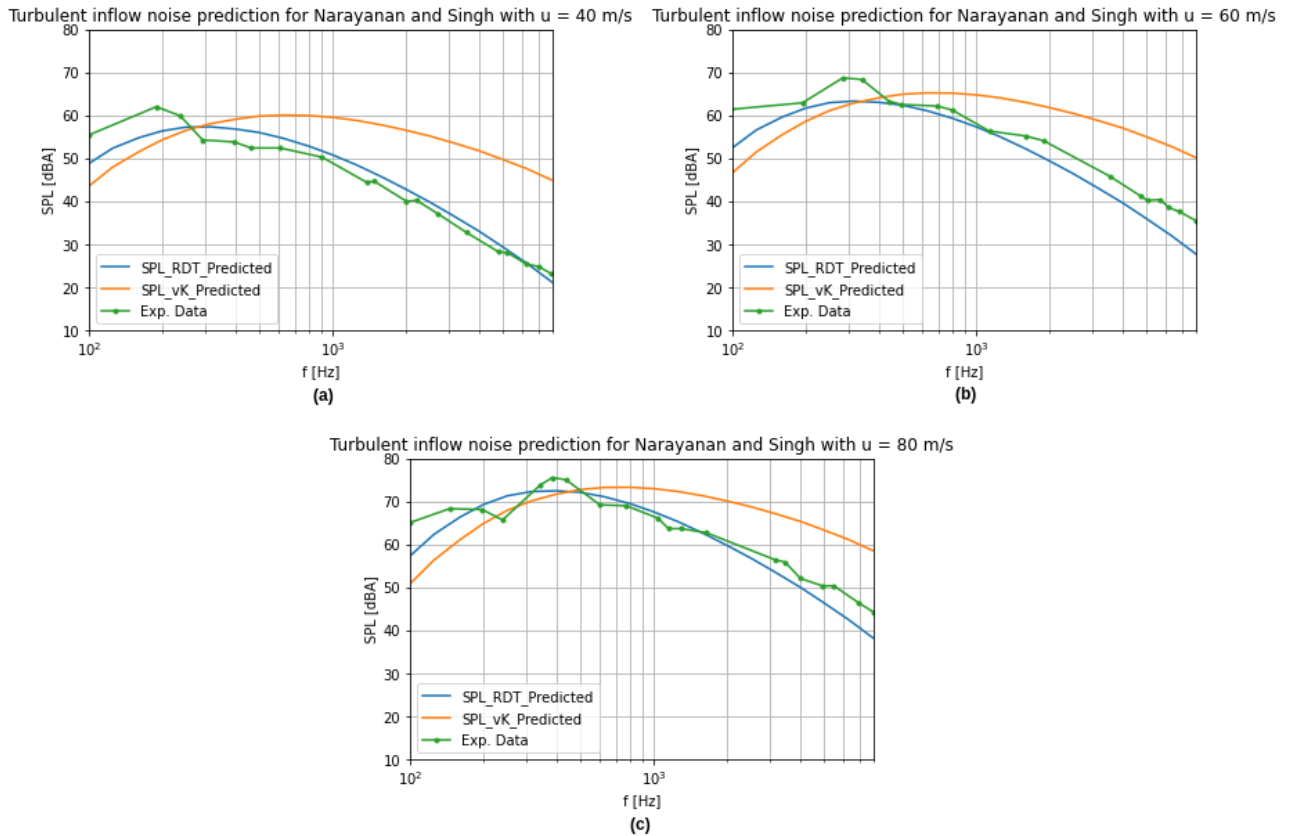
Figure 32: Comparison between the A-filtered turbulent inflow noise experimental data (green lines with dots) collected by Narayanan and Singh (2020) and the predicted curves for the standard Lowson method, considering von Kármán isotropic turbulence (orange solid curves), and the RDT-modified Lowson method (blue solid curves). The flow regimes refer to table 29, where (a) stands for $U = 40 \ m/s$, (b) represents $U = 60 \ m/s$ and (c) denotes $U = 80 \ m/s$.

By taking an overview of figures 30, 31 and 32, the adherence of the experimental datasets to the RDT-modified prediction method is fairly clear and confirm the expected behavior based on the table 4 criteria. The discrepancy between measurements and the von Kármán isotropic turbulence Lowson method points out that even thin airfoils inside the test section induce distortion on the turbulent eddies, and therefore significant anisotropy.

In cases (a) and (b) of figure 30, (a) of figure 31 and in cases (a) and (c) of figure 32, for given frequency ranges, the modified Lowson method fits the measurement data so well as seen on linear regression models. Indeed there are some noticeable under and overstimation of up to 10 dBA, but it is distinctly more accurate than the prediction method that assumes turbulence to be isotropic and follow a von Kármán spectrum model. Besides,

the peak frequency also match in almost every graph, although its correspondent SPL peak value may not. No measurement dataset is detached from the predicted spectrum considering RDT. Quantitatively, it is possible to integrate the curves and obtain the corresponding overall sound pressure level (OASPL) and through statistical methods one can evaluate the root mean square (RMS) error of the prediction methods. The RMS error turbulent inflow noise SPL follows the expression

$$RMS_{error} = \sqrt{\frac{\sum(SPL_{predicted} - SPL_{measured})^2}{n}}. \tag{3.1}$$

The RMS error associated to each experimental measurement and prediction are calculated and summarized in table 5.

Table 5: RMS error evaluation

| | U | $RMS_{error}(dBA)$ | |
	(m/s)	von Kármán	RDT
Bampanis _et al._, 2019	19	15.47	1.79
	27	15.17	3.25
	32	15.69	4.69
Juknevicius and Chong, 2018	30	17.82	3.39
	50	15.98	4.06
	60	15.50	4.50
Narayanan and Singh, 2020	40	15.22	5.08
	60	9.66	5.36
	80	8.94	6.37

As expected from the observation of figures 30, 31 and 32, while the assumption of isotropic turbulence following the von Kármán spectrum model resulted on an error that ranged from 15.17 dBA to 17.82 dBA for the standard Lowson prediction method, the RMS error associated to the rapid distortion spectrum assumption ranged from 1.79 dBA to 6.37 dBA, which is more reasonable for the purpose of increasing prediction accuracy.

Yet, by taking the integral of each of the curves, the overall sound pressure level for each flow-airfoil configuration is presented in table 6.

It is once again verified that the RDT-modified prediction method is more effective on predicting the turbulent inflow noise either for Bampanis _et al._ (2019), for Juknevicius and Chong (2018) or Narayanan and Singh (2020) configuration, except for a single measurement from the latter, with $U = 60\ m/s$, where the $\Delta OASPL$ is smaller for the prediction method computed with von Kármán isotropic turbulence.

From figure 32 (b), it is possible to identify a bias induced by the measured SPL in frequencies around 300 Hz on the $OASPL$ for such experimental conditions, and that should have produced this discrepancy with respect to the correspondent predicted value

Table 6: Overall sound pressure level (OASPL)

	U (m/s)	$OASPL_{measured}$ (dBA)	$OASPL_{predicted}$ (dBA)		$\Delta OASPL$ (dBA)	
			von Kármán	RDT	von Kármán	RDT
Bampanis et al., 2019	19	44.74	50.74	43.85	6	-0.89
	27	52.14	60.71	55.58	8.57	3.44
	32	56.04	65.49	61.14	9.45	5.1
Juknevicius and Chong, 2018	30	55.23	58.94	52.69	3.71	-2.54
	50	66.97	73.35	69.51	6.38	2.54
	60	70.57	78.42	75.35	7.85	4.78
Narayanan and Singh, 2020	40	65.95	69.51	65.67	3.56	-0.27
	60	74.05	74.59	71.51	0.54	-2.54
	80	81.43	82.50	80.54	1.07	-0.89

by the RDT-modified Lowson method.

The inflow noise prediction results confirm what was supposed true from the table 4 criteria. In any of the two experimental setups, the turbulent eddies were likely to distort once approaching and interacting with the airfoil surface. This thus emphasizes the importance of an accurate turbulence mapping and confirms the eddies behavior described by Batchelor and Proudman (1954) and Santana et al. (2014).

3.4 Airfoil thickness effects on turbulent inflow noise

Amiet theory-based turbulent inflow noise prediction methods are well known for producing good preliminary results and estimates, as it was presented in the last section. However, a major drawback of such noise prediction methods is the thin airfoil hypothesis. That means Amiet-based methods, e.g. standard and RDT-modified Lowson method, do not take into account the actual airfoil shape other than chord and span. Although being this approximation good enough for many applications, e.g. industrial fans, drones and home wind turbines (Geyer et al., 2019), a method derived under thin airfoil assumption might not work properly for others applications, such as aircraft noise and wind turbine noise.

For wind turbines, the blade airfoils are known to have relative thicknesses that range from 18% to 24% (Tangler and Somers, 1995), which may be considered out of scope of thin airfoil approximation. Because of that, a still open research subject is the incorporation of thickness effects on Amiet-based airfoil noise prediction methods (Tian et al., 2013).

In the field of high fidelity computational aeroacoustics, Gershfeld (2004) and, more re-

cently, Zhong *et al.* (2020) have presented discussion on thickness and camber effects on turbulent inflow noise generation. For semi-empirical preliminary analysis purposes, on the other hand, Tian and Cotté (2016) proposed a thickness correction expression relative to a NACA 0012 experiment from Roger and Moreau (2010).

3.4.1 Tian and Cotté expression for SPL reduction

Investigation conducted by Roger and Moreau (2010) pointed out that Amiet-based prediction methods produced an accentuated overestimation of the noise spectra, specially for frequencies above 1000 Hz, supposedly on account of thickness effects. It is also indicated that a correction of the incident turbulence spectrum based on RDT may improve the quality of the prediction methods (Roger and Moreau, 2010).

To assess the potential overestimation, Roger and Moreau (2010) conducted for three different geometries: a flat-plate airfoil, with relative thickness smaller than 3%, a NACA 0012 airfoil and a cambered optimized airfoil, with relative thickness of 3%. Although the authors did not provide some of the needed information to reproduce their experiment and/or their prediction, e.g. distance between source and observer, a chart containing the difference between predicted and measured sound pressure levels as function of the frequency and the airfoil thickness was presented, and it is reproduced at figure 33.
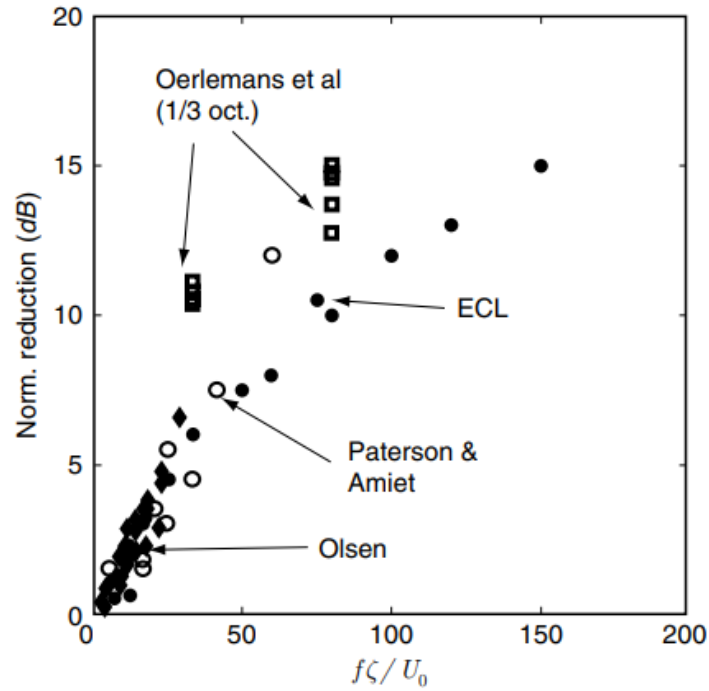
Figure 33: Amount of far-field response reduction of an airfoil to incident turbulence as a function of the airfoil thickness and frequency. Paterson and Amiet and ECL results refer to a NACA 0012 airfoil; Oerlemans and Migliore results refer to a wind turbine airfoil; Olsen results refer to an airfoil in a turbulent round jet. Source: (Roger and Moreau, 2010).

In figure 33, the ECL black dots refer to the Roger and Moreau (2010) NACA 0012 experiment and, based on that data, Tian and Cotté (2016) derived an expression for the sound pressure level reduction SPL_R, as a linear regression, thus resulting in the following expression,

$$SPL_R = \frac{9}{50} \frac{(e/c)}{(e/c)_{ref}} \frac{f}{U} \frac{(L/c)_{ref}}{(L/c)}, \tag{3.2}$$

where e/c is the maximum relative thickness of the airfoil, L/c is the relation between turbulence integral length scale and the airfoil chord. The subscript ref references to the experiment from Roger and Moreau (2010) for a NACA 0012 airfoil. In that case, the values correspond to $(e/c)_{ref} = 0.12$ and $(L/c)_{ref} = 0.1$.

As depicted in figure 34, reproduced from Tian and Cotté (2016), for the given case of Paterson and Amiet experiment with a NACA 0012, equation (3.2) has seemed to serve well the purpose of adjusting the turbulent inflow noise prediction to the measured spectrum in the frequency range from 200 Hz up to 5000 Hz. Nevertheless, once being derived based on a similar geometry as the tested, the (e/c) ratio is equal to the reference

value and the term $\frac{(e/c)}{(e/c)_{ref}}$ goes to the unit and vanishes from the equation.
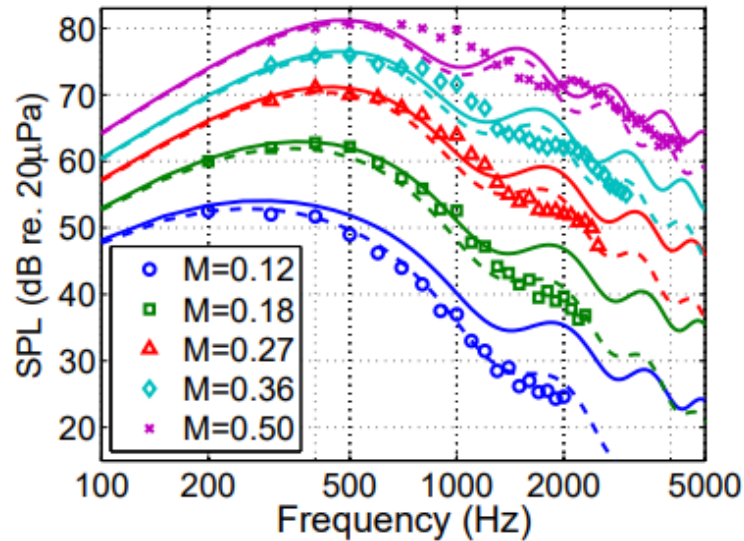
Figure 34: Turbulent inflow noise predictions with (dashed lines) and without (solid lines) thickness correction for a NACA 0012 airfoil. The symbols correspond to measurements conducted by Paterson and Amiet. Source: (Tian and Cotté, 2016).

Besides, the predicted curves with and without Tian and Cotté correction are obtained under the assumption of isotropic turbulence, which is deemed not to be the real case either for an airfoil in an acoustic tunnel (Santana *et al.*, 2014), or for an airfoil subjected to atmospheric turbulence (Batchelor and Proudman, 1954, Hunt, 1973, Simonich *et al.*, 1986), according to the criteria established by equations (2.95), (2.96) and (2.97). Thus its validity must be investigated.

3.4.1.1 Validation pitfalls

Aiming for further validation of the thickness effects correction on SPL prediction, Tian and Cotté (2016) gathered the measurement data from Devenport *et al.* (2010) for a S831 non symmetrical airfoil, with chord length 0.91 m, span of 1.83 m, and maximum relative thickness of 18% inside the open-jet of the Virginia Tech (VT) acoustic tunnel. Figure 35 illustrates the comparison of Virginia Tech experimental data and two prediction curves, with and without considering the thickness correction.
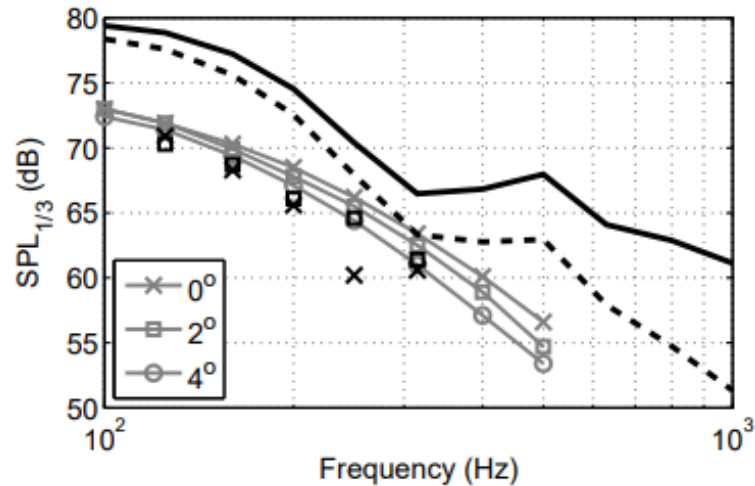
Figure 35: Turbulent inflow noise predictions with (black dashed lines) and without (black solid lines) thickness correction for a S831 airfoil. The results are compared to the measurements (black symbols) and predictions (gray lines) of Devenport *et al.* for AoA 0°, 2° and 4°. Source: (Tian and Cotté, 2016).

Despite presenting the same trend and also a proximity in a very short frequency range, from 250 Hz to 315 Hz, the thickness corrected prediction presents overestimation for up to 15 dB in the spectrum. Furthermore, two major pitfalls are spotted in the analysis.

First, measurements conducted for a S831 airfoil, at the same VT acoustic tunnel, but for airfoil self-noise (Devenport and Burdisso, 2010), have produced discrepancies of around 10 dB close to the 1000 Hz band in comparison to the BPM TE model (Brooks *et al.*, 1989). In spite of that, Devenport *et al.* have considered the results to be "*in good agreement in the* 1000 Hz *to* 4000 Hz *range*", and the discrepancies were attributed to different wind tunnel test facilities and methods to compute the airfoil self-noise from raw data. On account of that, Doolan and Moreau (2013) and Saab Jr. *et al.* (2018) suggested that the VT experimental dataset was not suitable for their specific validation processes, as figure 36 illustrates.
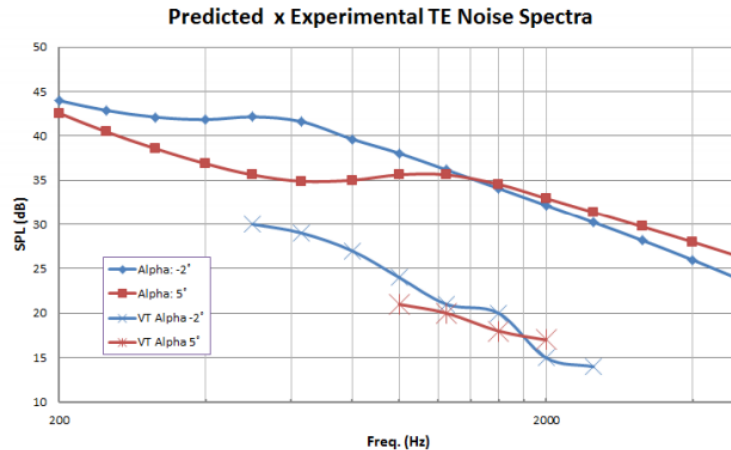
Figure 36: Total TE Noise SPL calculated bt the modified BPM method (upper plots), compared to VT measured spectrum (lower plots), for the tripped S831 airfoil at 28 m/s at $-2°$ and $5°$ AoA. Source: (Saab, 2016).

While trying to replicate the results obtained by Tian and Cotté (2016) for the $S831$ airfoil of the VT research, for the same flow conditions and assumptions, a second pitfall was spotted. Devenport *et al.* (2010) measurements point to a turbulence integral length scale of 0.082 m. However, Tian and Cotté (2016) SPL prediction from figure 35 considers an integral length scale of 0.82 m, which is not only ten times greater than the measured length scale from Devenport *et al.* (2010), but it is also a structure with an order of magnitude much larger than grid-generated turbulent scales and that may compromise the comparison between the predicted spectrum and the experimental data, presenting then a behavior completely different from what was presented in figure 35.

It was decided, however, to run the standard Lowson method with the original input parameters of the VT experiment and recalculate the prediction following Tian and Cotté model expression, but with the correct integral length scale, and compare it to the erroneous.

According to Devenport *et al.* (2010), a S831 airfoil was placed inside the test section of the VT acoustic tunnel at zero angle of attack, with a microphone was placed 1.80 m orthogonal to its leading-edge. Turbulence was generated by a grid and its intensity set to 3.9%, while the measured turbulent integral length scale was 0.082 m. Hot-wire measurements indicated a near isotropic turbulence following a von Kármán spectrum, without the airfoil. The mean flow conditions correspond to a Mach number $M = 0.08$ ($U = 28$ m/s) and a Reynolds number $Re = 1.7 \cdot 10^6$.
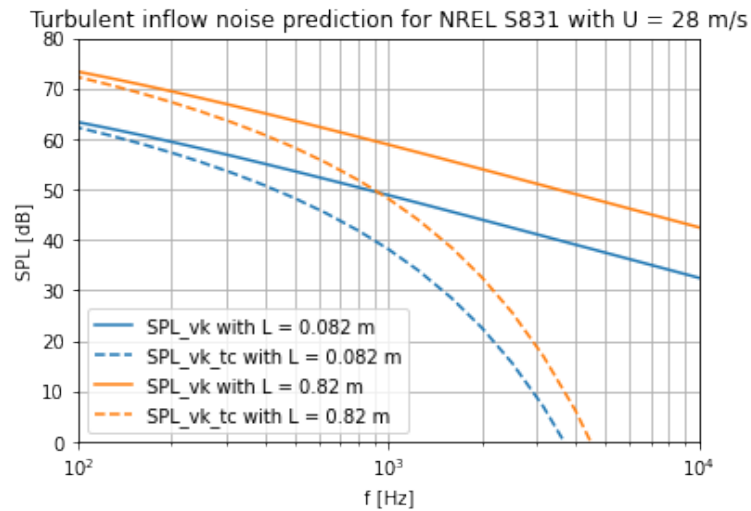
Figure 37: Comparison between the Tian and Cotté turbulent inflow noise prediction considering thickness effects, for the NREL S831 airfoil. Turbulence integral length scales are the erroneous $L = 0.82\ m$ and the actual $L = 0.082\ m$.

Figure 37 is an illustrative example of the sensitivity of the SPL prediction to the integral length scale. Comparing the obtained spectrum for $L = 0.82\ m$ and for $L = 0.082\ m$, an increase of 10 dB is observed for the whole frequency spectrum, with and without the thickness effects correction, due to the adoption of an inappropriate length scale. Furthermore, by plotting the Lowson SPL prediction with $L = 0.82\ m$ and comparing it to the measurements from Devenport et $al.$, it is observed that the prediction fits the experimental data so well as a linear regression.
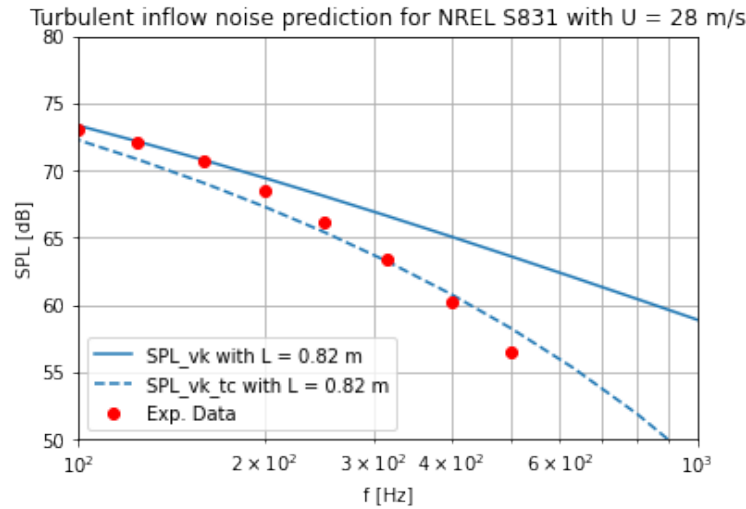
Figure 38: Comparison between the SPL prediction, with and without Tian and Cotté reduction model, considering the incorrect turbulent length scale of $L = 0.82\ m$, and the experimental data gathered from Devenport *et al.* (2010).

Figure 38 is where both of the two pitfalls lie. The apparent fitting of the measurement data by the standard Lowson method coupled with Tian and Cotté SPL reduction is only virtual, and that is because of the nature of the problem. Grid generated turbulent scales are known to have an order of magnitude lower that is under 10% of the tested characteristic length, i.e. the S831 airfoil chord. This apparent fitting may be an indicative that measurement and Tian and Cotté prediction are one and the other inconsistent.
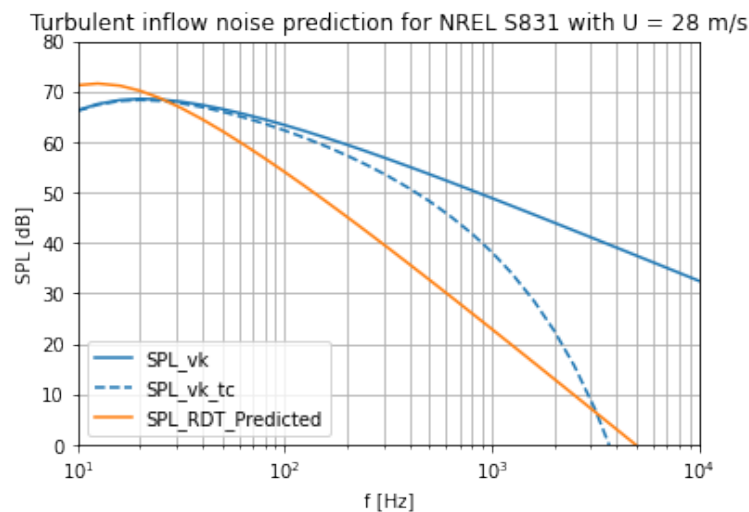
Figure 39: Comparison between the effects of Tian and Cotté thickness correction and the RDT spectrum modification on the predicted SPL versus the standard Lowson prediction method considering Devenport *et al.* (2010) experimental setup.

As a second illustrative example, a comparison of the effects of changing the turbulence spectrum from von Kármán isotropic turbulence to the rapidly distorted anisotropic spectrum and the result of coupling Tian and Cotté thickness correction to the standard Lowson prediction method is performed by running the correspondent *Python* routines. As it is depicted in figure 39, the adjustments provided by Tian and Cotté SPL reduction are way less impactant to the prediction, when compared to the RDT hypothesis. As a function of the frequency, it is expected that SPL_R becomes larger and larger along the frequency range. On the other hand, the RDT turbulence spectrum hypothesis produces a prediction curve with a higher slope and a more drastic reduction. That may be an indicative that, if the equations (2.95), (2.96) and (2.97) RDT criteria are met, the gap between prediction and measurements may be due to a incorrect choice of the turbulence spectrum modeling, and not on account of thickness effects.

Moreover, equation (3.2) might not be serving its intentional purpose. Instead, it may just be attenuating the discrepancies related to the use of an incorrect turbulence spectrum model that does not consider wall effects, the shear layer induction, and the distortion of the grid-generated turbulent eddies because of the presence of the airfoil in the test section of acoustic tunnels.

3.4.2 Guidati-Moriarty thickness correction

Buck *et al.* (2018) make use of a more conservative $SPL_{1/3}$ reduction expression due to finite thickness of real airfoils. This model is taken from Moriarty *et al.* (2004), and is based on an interpolation of a model developed by Guidati for the turbulent inflow noise prediction for airfoils of finite thickness (Guidati *et al.*, 1997). The expression for the Guidati-Moriarty thickness correction follows,

$$SPL_{G-M} = SPL_{inflow} + \Delta SPL + 10, \tag{3.3}$$

where SPL_{G-M} is given in dB. SPL_{inflow} in this text refers to the predicted turbulent inflow noise considering the classical Lowson method, from equations (2.107) to (2.111), and the 10 dB constant value comes from a experimental validation of the original Guidati model. The model for ΔSPL follows,

$$\Delta SPL = - \left[1.123 \left(T_{rel,1\%} + T_{rel,10\%} \right) + 5.317 (T_{rel,1\%} + T_{rel,10\%})^2 \right] \left[2 \left(k_x/k_e \right) + 5 \right], \tag{3.4}$$

where $T_{rel,1\%}$ and $T_{rel,10\%}$ are the finite airfoil relative thicknesses in the positions of 1% and 10%, respectively, relative to the chord length.

Unlike the expression derived by Tian and Cotté, which is based only on the maximum relative thickness of the airfoil, the Guidati-Moriarty model is based on two different thickness values, that correspond to points along the airfoil chord.

3.4.2.1   Guidati-Moriarty expression validation

Similar to the previous qualitative investigation, Devenport *et al.* (2010) experimental setup is considered as the case study. A *Python* script coupling equation (3.4) with the standard Lowson method is written to assess the thickness correction effects.

Table 7: Interpolation of the NREL S831 generation curves

Location relative to the chord length (x/c)	Relative thickness (%)
@1%	2.8820541
@10%	9.2944001

In this case, it was necessary to look after the NREL S831 curves and obtain through linear interpolation the values for relative thicknesses correspondent to the locations at 1% of the chord and 10% of the chord, and are summarized in table 7. These values of local relative thicknesses are central objects for evaluating the ΔSPL term from equation (3.4).

A first analysis concerning Guidati-Moriarty SPL correction is performed by comparing it to the correction obtained by Tian and Cotté expression, both coupled with the standard Lowson method.
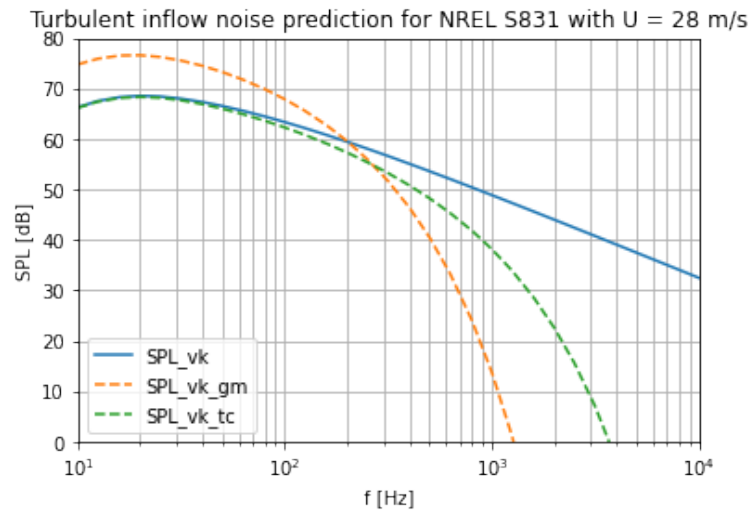
Figure 40: Comparison between Tian and Cotté (2010) and Guidati-Moriarty (1997) SPL corrections based on thickness effects on turbulent inflow noise. The comparison is based on the experimental setup from Devenport *et al.* (2010), with $U = 28 \ m/s$

.

As depicted in figure 40, the effects of Guidati-Moriarty SPL correction on the noise spectrum prediction difer substantially from Tian and Cotté model. While Tian and Cotté model is a pure SPL reduction expression and acts as a filter, Guidati-Moriarty correction induces a low-frequency hump on the predicted SPL and filters it more drastically in the high frequencies range. Although less intense, the RDT spectrum hypothesis, supported by equations (2.95), (2.96) and (2.97) criteria, also induces a low-frequency hump.
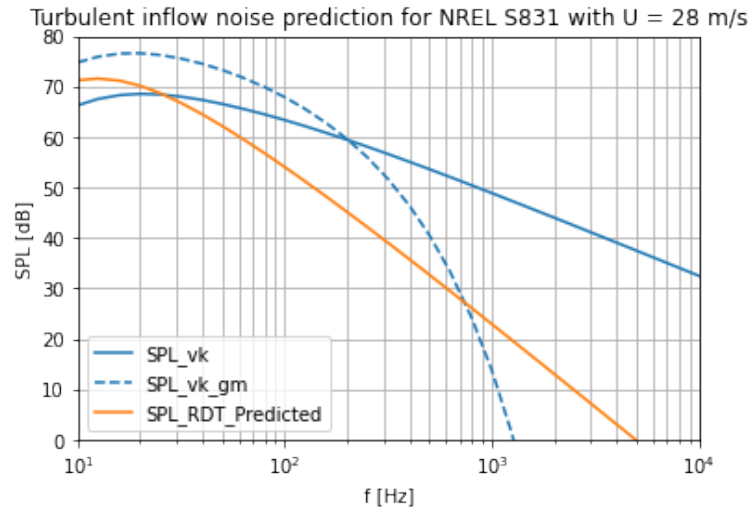
Figure 41: Comparison between and Guidati-Moriarty (1997) SPL corrections based on thickness effects on turbulent inflow noise prediction and the RDT spectrum assumption. The comparison is based on the experimental setup from Devenport *et al.* (2010), with $U = 28 \ m/s$

.

Figure 41 presents these similarities between each other turbulent inflow noise prediction method, yet the SPL reduction is more effective under the of the assumption of a rapidly distorted turbulence spectrum for frequencies in a range up to 1000 Hz. For frequencies above 1000 Hz, the airfoil self-noise sources become more prominent and the contribution of TI noise mechanism to the overall spectrum is many times negligible.

The results once again point that the so-called thickness correction methods, instead of incorporating real airfoil effects, were only attenuating the errors caused by an incorrect turbulence spectrum assumption, as the RDT criteria indicate for such test conditions.

This result dialogues in a macro scale with the observation made by Santana, for airfoils subjected to incoming turbulence in an acoustic tunnel, that the turbulent eddies rapidly distort once approaching the airfoil leading-edge, abandoning its previous isotropic distribution. This can also be used to open a debate on near airfoil turbulence behavior, as many authors ensure a near homogeneous and isotropic turbulence condition in the test section of the acoustic tunnels in the absence of the airfoil, conduce the measurements with the airfoil placed in that same test section, and then present a prediction method which models turbulence as homogeneous and isotropic, neglecting the effects due to the airfoil presence within the turbulent flow.

As a complement, the thickness effects on adjusting the airfoil turbulent inflow noise prediction may be deemed low, in comparison to the change on turbulence spectrum

modeling, at the same manner as for thin airfoils, given that a similar behavior is observed. That is because even for infinitesimally thin flat-plate airfoils in a test section of a wind/acoustic tunnel, a condition only ensured in a no-airfoil situation is not reproducible. Despite this, however, given that there is a lack on measurements for turbulent inflow noise data, specially for thicker airfoils or for angles of attack other than zero, it is still only possible to have a qualitative analysis of the noise prediction methods, which was presented in this section, and more measurement data is needed to further validate and expand the validity range of the method subject of discussion.

It is noticed that, despite the fact that many authors observe a nearly isotropic turbulence inside the test section of an acoustic tunnel, that is done in the absence of the airfoil. In effect, its simple introduction drastically changes the turbulence spectrum by rapidly distorting eddies. Therefore, the actual turbulence spectrum under such conditions is far departed from that of homogeneous and isotropic turbulence. This is confirmed by validating the data against measurements from Bampanis *et al.* (Bampanis *et al.*, 2019), and from Juknevicius and Chong (Juknevicius and Chong, 2018), for airfoils with 3% and 8% relative thickness respectively, subjected to flows which chord-based Reynolds numbers ranged from $1.3 \cdot 10^5$ to $6 \cdot 10^5$.

In order to understand the thickness effects of real airfoils in turbulent inflow noise prediction, a $SPL_{1/3}$ reduction expression derived by Tian and Cotté (Tian and Cotté, 2016) was revisited and compared to the effects of the change on the turbulence spectrum model. For the same specific case presented in their article, their expression appeared to be attenuating the discrepancies caused by the use of an incorrect turbulence spectrum model, instead of attending to its intentional purpose.

Amiet-based turbulent inflow noise prediction methods consider the hypothesis of a thin airfoil subjected to a turbulent flow. By assuming the turbulence to be isotropic, given that it is a condition nearly observed only on the absence of the airfoil, these two statements are conflicting. A thin airfoil, so thin that it can be approximated to the flat-plate condition, is still an airfoil, a solid and rigid body, with finite chord and span, which induces a shear layer when subjected to a flow, so turbulence cannot be considered homogeneous and isotropic if there is any hindrance to the flow, with characteristic length larger than the turbulence integral length scale. In other words, the isotropic turbulence assumption is equally conceptually inappropriate for flat-plate, thin and even thick airfoils because represents a flow condition that disconsider the airfoil.

4   ROTOR FIELD MEASUREMENTS

This chapter concludes the airfoil noise assessment topic by investigating whether the standard Lowson method, based on isotropic turbulence assumption, or the newly derived RDT-modified Lowson method predicts best the turbulent inflow noise produced by full scale wind turbine blades interacting with the incoming atmospheric turbulence. The task of finding measurement data concerning wind turbine noise is not that simple, given that there is not much recent available data in the literature, specially for modern large wind turbines, whose blades range from 70 to 110 meters.

Table 8: Technical data for Vestas VT 27 225 kW. Source: (Fuglsang and Madsen, 1996).

Vestas VT 27 225 kW	
Rotor type	Upwind, pitch regulated
Rated power	225 kW
Rotor diameter	27 m
Hub height	31.5 m
Number of blades	3
Maximum chord	1.33 m
Tip chord	0.47 m
Maximum twist	14°
Airfoils	Modified NACA 63200 series
Angular velocity	43.0 rpm
Tip pitch angle	Various between $-1.5°$ and $3.5°$

Fuglsang and Madsen, while proposing geometric optimization of WT units based on measurements from Andersen and Jakobsen, have provided, in details, the technical data of a *Vestas VT 27 225 kW* wind turbine and a *Bonus Combi 300 kW* WT (Fuglsang and Madsen, 1996, Andersen and Jakobsen, 1995).

Table 9: Technical data for Bonus Combi 300 kW. Source: (Fuglsang and Madsen, 1996).

Bonus Combi 300 kW	
Rotor type	Upwind, stall regulated
Rated power	300 kW
Rotor diameter	31 m
Hub height	30.7 m
Number of blades	3
Maximum chord	1.58 m
Tip chord	0.50 m
Maximum twist	16°
Airfoils	NACA 63400/NACA 63200 series
Angular velocity	35.0 rpm
Tip pitch angle	−1.8°

The technical specification of both wind turbine units are presented in tables 8 and 9, which are reproduced from Fuglsang and Madsen report. Although being nowadays classified as small units, both of the WT presented in their study are still representative qualitatively and quantitatively for the purpose of validation, even for such specific conditions.
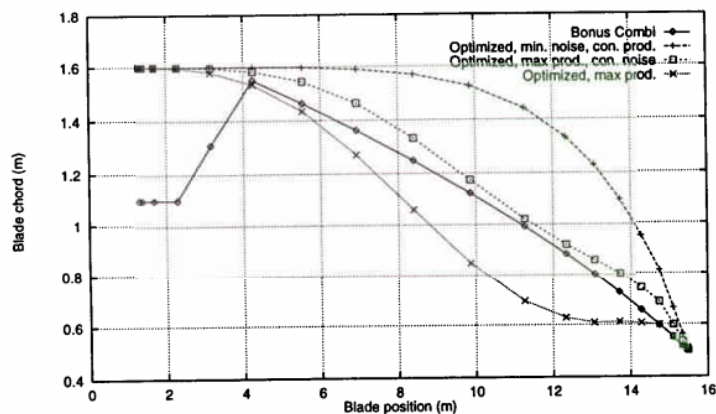
Figure 42: Airfoil chord distribution for the *Bonus Combi* wind turbine blades, along its rotor radius. Source: (Fuglsang and Madsen, 1996)

As an additive to the technical specification, Fuglsang and Madsen (1996) also provided the airfoils chord distribution along the wind turbine blade span for the *Bonus Combi 300 kW* wind turbine, as depicted in figure 42. That allows a more accurate assessment of the turbulent inflow noise, once it is possible to employ *QBlade* aerodynamic

analysis modules such as the blade element momentum (BEM) method to gather relevant information regarding the inflow velocity distribution and compute the TI noise as a summation of each segment contribution.

4.1   A note on wind turbines aerodynamics

Transposing airfoil noise prediction methods, which are representative of acoustic tunnel experiments, mainly focused on aeronautical applications to a full scale wind turbine noise assessment is not a simple task, given its particularities such as the local flow conditions, e.g. the characteristics of atmospheric turbulence. As previously seen in figures 26 and 27, these conditions are not easily obtained or estimated, as turbulence intensity and integral length scale estimation methods diverge from each other and are not conclusive enough. In addition to that, attention should be drawn to the fact that the commonly used grid-generated turbulence scales from acoustic tunnel measurements, acoustic tunnel measurements have an order of magnitude that may be hardly comparable to atmospheric turbulent scales.

Currently, *QBlade* presents many tools that allow the determination of the local flow conditions in each section of the wind turbine blade, such as the *XFOIL/XFLR5* and the blade element momentum method. The BEM method makes possible the analysis of the local inflow velocities for each blade section, and, consequently, a more careful assessment of the turbulent inflow noise for the entire WT blade, based on the tip speed ratio (TSR) and the mean flow velocity at the far-field.

4.1.1   BEM method

The BEM method is a powerful tool for determining the local flow conditions on defined segments of the blade rotor, along with steady loads, thrust and power for different wind speeds, rotational speeds and pitch angles (Hansen, 2008).
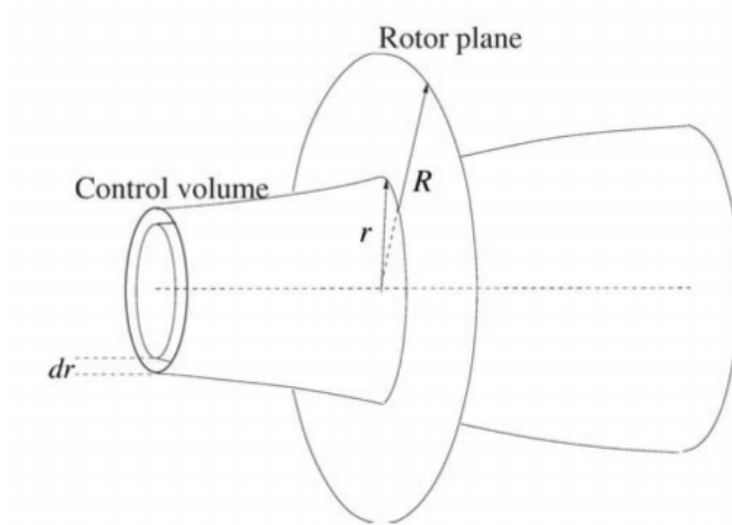
Figure 43: Annular control volume for the BEM method (Hansen, 2008)

.

In the BEM method, the rotor is discretized into N annular elements of width dr along its plane (see figure 43), having the streamlines as boundaries.
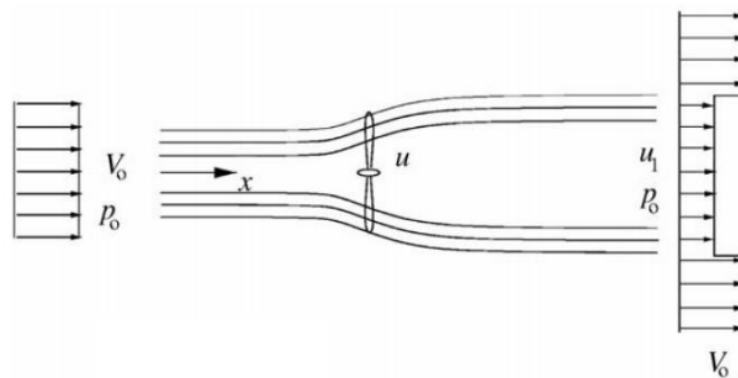
Figure 44: Streamlines passing a rotor in the windimilling state, with axial distributions of pressure and velocity (Hansen, 2008)

.

The model hypothesis for the control volumes are:

- No radial influence on neighbor control volumes. The control surface is a streamtube, as in figure 44.

- The number of blades in the rotor is infinite. The force that the blades exert on the flow is constant in each annular area. The Prandtl tip loss correction factor is then introduced to compensate for this hypothesis.

- The pressure distribution along the curved streamlines enclosing the wake does not result in an axial force component.
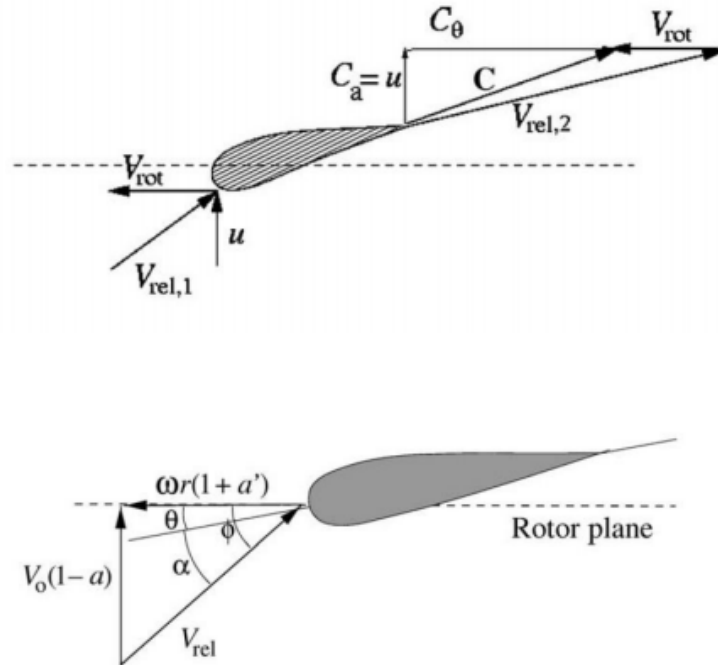
Figure 45: Velocity triangles at the edges and relative velocity at the LE (Hansen, 2008)

.

With the velocity notation given by figure 45, the thrust dT on the annular control volume with area $2\pi r dr$ can be found from the integral momentum equation as

$$dT = (V_0 - u_1)d\dot{m} = 2\pi r \rho u(V_0 - u_1)dr, \tag{4.1}$$

where V_0 is the undisturbed wind speed, the axial speed in the rotor plane is $u = (1-a)V_0$, and the axial speed in the wake is given by $u_1 = (1-2a)V_0$, where a is the axial induction factor.

For the ideal rotor, there is no rotation in the wake and a', which is the tangential induction factor, is zero. In the case of a modern wind turbine, with a single rotor and no stator, however, the wake will have some rotation. Thus, the torque dM on the control volume, considering the rotational velocity upstream the rotor as zero, can be written as

$$dM = rC_\theta d\dot{m} = 2\pi r^2 \rho u C_\theta dr, \tag{4.2}$$

where $C_\theta = 2a'\omega r$ is the rotational velocity in the wake of the rotor and a' is the tangential induction factor.

The velocity triangles for a section of the rotor can be seen at figure 45.

With the definitions of the axial and tangential induction factors, equations (4.1) and (4.2) can be rewritten as follows:

$$dT = 4\pi r \rho V_0^2 a(1-a)dr;$$ (4.3)

$$dM = 4\pi r^3 \rho V_0 \omega (1-a)a'dr.$$ (4.4)

By solving the local flow in the leading-edge it is possible to calculate the thrust and torque, and to integrate both over the rotor area.

As shown in the lower diagram of figure 45, the local angle of attack, α, is given by the angle between the plane of rotation and the relative velocity, ϕ, and the local pitch of the blade, θ, as

$$\alpha = \phi - \theta.$$ (4.5)

The local pitch angle of the section, θ, is the combination of the variable pitch angle, θ_p, and the twist of the blade, β, as

$$\theta = \theta_p + \beta.$$ (4.6)

From the lower diagram of figure 45, the angle ϕ can be determined as

$$tan\phi = \frac{(1-a)V_0}{(1+a')\omega r}.$$ (4.7)

With both axial and tangential local velocities determined, the relative velocity, $V_r el$, is also determined and the lift and drag components, which are by definition perpendicular and parallel to the relative velocity, may also be obtained by

$$\frac{L}{s} = \frac{1}{2}\rho V_{rel}^2 C_L c;$$ (4.8)

$$\frac{D}{s} = \frac{1}{2}\rho V_{rel}^2 C_D c,$$ (4.9)

where c is the local airfoil chord and s is the span of the airfoil segment in the considered section.
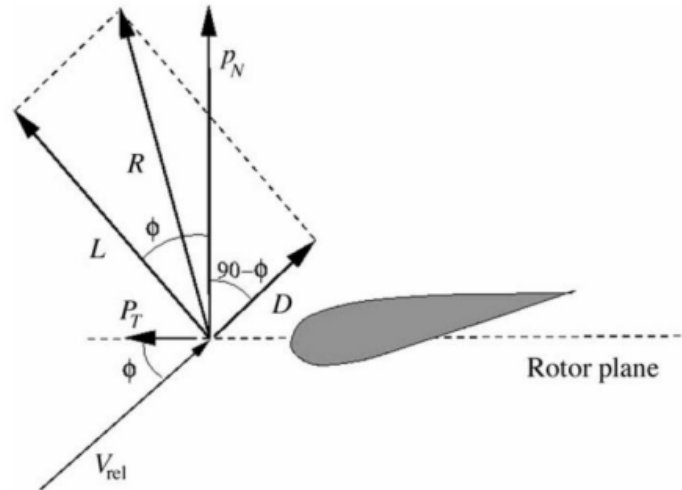
Figure 46: Forces perpendicular and normal to the rotor plane (Hansen, 2008)

.

The blade designer, however, is mostly interested in the forces acting on the rotor plane or perpendicular to it. These loads may be found by projecting the aerodynamic resultant as shown in figure 46.

The resulting projected forces per unit span are shown below, along with their dimensionless coefficient forms:

$$p_N = Lcos\phi + Dsin\phi; \tag{4.10}$$

$$C_n = C_L cos\phi + C_D sin\phi; \tag{4.11}$$

$$p_T = Lsin\phi - Dcos\phi; \tag{4.12}$$

$$C_t = C_L sin\phi - C_D cos\phi. \tag{4.13}$$

The number of blades is finite, so the fraction of the annular area covered by the blades is a function of the rotor radius and is defined as the solidity ratio, σ, i.e.:

$$\sigma(r) = \frac{c(r)B}{2\pi r}, \tag{4.14}$$

where B is the number of blades in the rotor.

The axial and tangential forces, respectively thrust and torque, on the control volume of span dr are

$$dT = Bp_N dr = \frac{1}{2}\rho B \frac{V_0^2(1-a)^2}{sin^2\phi}cC_n dr; \tag{4.15}$$

$$dM = rBp_T dr = \frac{1}{2}\rho B \frac{V_0(1-a)\omega r(1-a')}{sin^2\phi cos\phi}cC_t dr. \tag{4.16}$$

Combining equations (4.15) and (4.3), and by applying the definition of solidity, an ex-

pression for the axial induction factor can be derived as

$$a = \frac{1}{\frac{4sin^2\phi}{\sigma C_n} + 1}. \tag{4.17}$$

In the same manner, combining equations (4.16) and (4.4), it results in

$$a' = \frac{1}{\frac{4sin\phi cos\phi}{\sigma C_t} - 1}. \tag{4.18}$$

Given that the infinite number of blades assumption does not apply to real equipment and that the vortex system in the wake is different from the theory, the Prandtl tip loss factor F can be used to correct the thrust and the torque, so

$$dT = 4\pi r\rho V_0^2 a(1-a)F dr; \tag{4.19}$$

$$dM = 4\pi r^3 \rho V_0 \omega(1-a)F a' dr, \tag{4.20}$$

where $F = \frac{2}{\pi}\frac{1}{cos(e^{-f})}$, $f = \frac{B}{2}\frac{(R-r)}{s(sin\phi)}$, B is the number of blades, R is the total rotor radius, r is the local radius and ϕ is the flow angle. With this correction, the axial and tangential induction factor expressions derived before assume the following new formulation:

$$a = \frac{1}{\frac{4Fsin^2\phi}{\sigma C_n} + 1}; \tag{4.21}$$

$$a' = \frac{1}{\frac{4Fsin\phi cos\phi}{\sigma C_t} - 1}. \tag{4.22}$$
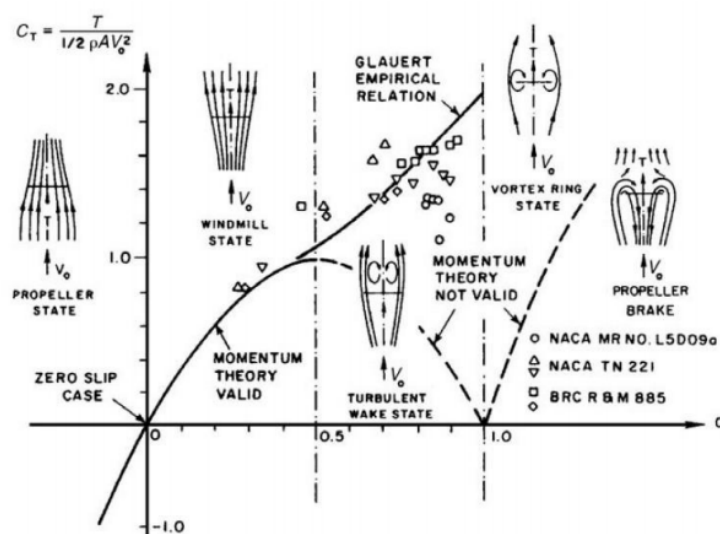
Figure 47: Rotor thrust coefficient as a function of axial induction factor (Hansen, 2008)

.

Another correction is needed for flow conditions where the axial induction factor is larger than 0.4. Figure 47 shows that, for $a > 0.4$, there is no adherence between the experimental data and the predicted thrust coefficient C_T. The operational regime for $a > 0.4$ is called the turbulent wake state, and the simple momentum theory over which the thrust and torque equations were developed for the rotor are not valid anymore. According to Hansen, empirical relations where proposed by Glauert and Wilson and Walker, which follow, respectively,

$$C_T = \begin{cases} 4a(a-1)F & a \leq \frac{1}{3} \\ 4a\left(1 - \frac{1}{4}(5-3a)a\right)F & a > \frac{1}{3} \end{cases} ; \tag{4.23}$$

$$C_T = \begin{cases} 4a(a-1)F & a \leq a_C \\ 4(a_C^2 + (1-2a_C)a)F & a > \frac{1}{3} \end{cases} , \tag{4.24}$$

where $a_C \cong 0.2$.
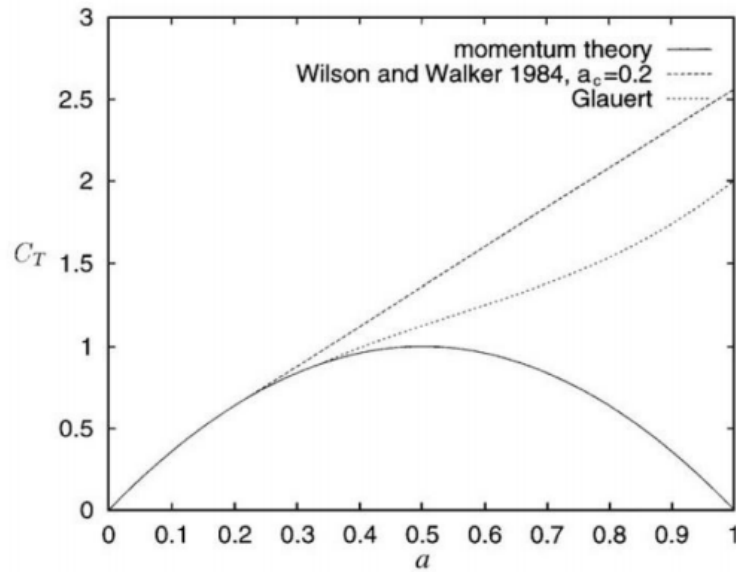
Figure 48: Thrust coefficient as a function of the axial induction factor for the momentum theory: continuous line; Glauert correction equation: dotted line; Wilson and Walker correction equation: dashed line (Hansen, 2008).

The results are plotted in the chart shown in figure 48.

4.2 Noise assessment of full scale wind turbines

Taking up the validation topic of the turbulent inflow noise prediction methods after this brief excursion on wind turbine blade aerodynamics, the *Python* scripts were run and tested for both *Vestas VT 27* and the *Bonus Combi 300 kW* blade geometries, the latter as a summation of each segment, according to figure 42, for both standard and RDT-modified Lowson methods.

From the technical specification of both wind turbine units presented in tables 8 and 9, it is possible to infer that, given a certain geometrical proximity between the studied WT, their SPL spectra will present some similarities to each other. Still, other relevant aspect of the measured noise spectra from Fuglsang and Madsen, for their respective flow conditions, turbulent inflow noise appears to be the major noise source for the overall noise spectrum (Fuglsang and Madsen, 1996), so it turns out to be a good validation exercise for the turbulent inflow noise prediction methods here described in a case for full WT flows.

4.3 Vestas VT 27 225 kW

Beginning with the *Vestas VT 27*, Fuglsang and Madsen (1996) measurements pointed to a mean wind speed of $U_\infty = 8 \ m/s$ and a tip speed ratio of $TSR = 7.6$. That results in a tip velocity $U = 60.8 \ m/s$. The authors adopted the turbulence integral length scale and the intensity respectively as $L = 100 \ m$ and $I = 10\%$, both independent of height, according to Danish standards for a terrain with Roughness Class 1 (Fuglsang and Madsen, 1996). Given that, different from the *Bonus Combi* wind turbine, no mention to the chord distribution along the blade was presented for the *VT 27*, a reasonable approximation for this prediction purpose is to consider each blade as a single airfoil with span equal to the blade length $s = 13.5 \ m$ and an average chord $c = 0.9 \ m$, which is an intermediate value between tip chord $c_{tip} = 0.47 \ m$ and the maximum chord $c_{max} = 1.33 \ m$. In this case, the observer was positioned at the ground, in a distance of 40 m downstream the WT.

Other than in acoustic tunnel measurements, the turbulent length scale is much larger than even the maximum blade chord c_{max}, so the larger scales may be less likely to distort as approaching the airfoil surface, as one of the RDT criteria (equation 2.96) is not fulfilled. That should indicate whether three criteria are mandatory or not. The SPL spectrum measurement follow an A-weight filter.

Figure 49: Comparison between the A-weighted SPL measurements from Fuglsang and Madsen for the *Vestas VT 27* wind turbine and the predicted turbulent inflow noise spectrum applying the standard and the modified versions of Lowson method. The experimental data correspond to the green line with dots, while the orange line refers to the isotropic turbulent spectrum assumption and the blue line corresponds to the prediction considering the rapid distorted turbulence spectrum.

Figure 49 shows that the curves from measurement data and the prediction obtained with the standard Lowson method clearly overlap in the frequency range from 500 Hz to 3000 Hz, while the RDT-modified prediction underestimates the entire sound pressure level spectrum. That may be an indicative that, for a full scale wind turbine in contact with atmospheric turbulence with an integral length scale $L = 100\ m$, the sound pressure level is more likely to be described by the standard Lowson method, and its turbulent velocity spectrum modeled after von Kármán isotropic turbulence.

Slight overestimation is noticed under 500 Hz and above 3000 Hz, although it does not appear to be the case of link it to the airfoil thickness, as either Tian and Cotté or Guidati-Moriarty thickness correction models produce way more drastic effects on the prediction. This overestimation may rely on uncertainties brought by the approximation of the blade to a single airfoil and the adopted pair $L - I$. Statistically, the standard Lowson method prediction has a root-mean-square error of 5.32 dB, while the RDT-modified curve corresponds to a RMS-error of 20.88 dB.

The experimental overall sound pressure level is $OASPL_{exp} = 97.50\ dBA$, while the predicted values are $OASPL_{von\ Kármán} = 99.59\ dBA$ and $OASPL_{RDT} = 85.99\ dBA$, resulting in $\Delta OASPL_{von\ Kármán} = 2.09\ dBA$ and $\Delta OASPL_{RDT} = -11.51\ dBA$.

4.4   Bonus Combi 300 kW

For the *Bonus Combi 300 kW* wind turbine, more details were provided by Fuglsang and Madsen, when compared to the *Vestas VT 27*. The chord distribution along the span of $s = 15.5\ m$, as reproduced in figure 42, allows a more accurate aerodynamic analysis of the blades.

Bonus Combi 300 kW (NACA 63400 and 63200)
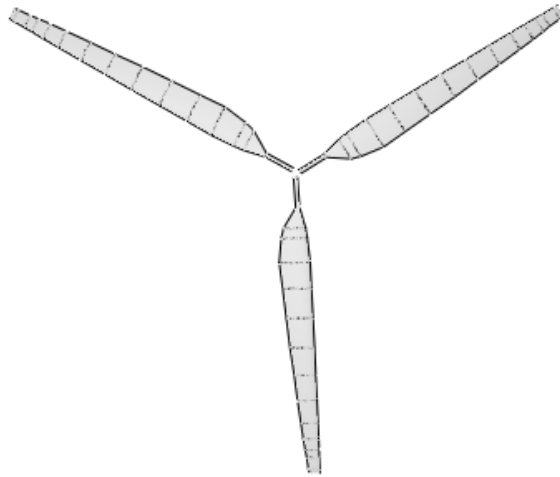
Figure 50: Sketch of the *Bonus Combi* wind turbine rotor in *QBlade*

Figure 50 is a reconstruction of the wind turbine rotor blades, performed in *QBlade*, following figure 42 chord distribution chart. This allows a more refined calculation for *Bonus Combi 300 kW* wind turbine noise prediction, without having to make any coarse approximation, such as the approximation of the blade as a single airfoil, as made for the *VT 27*.

With a mean wind speed of $U_\infty = 8\ m/s$ and a tip speed ratio of $TSR = 7.1$, it is possible to obtain the local inflow velocity distribution for each of the *Bonus Combi 300 kW* blades, by running *QBlade* BEM module.
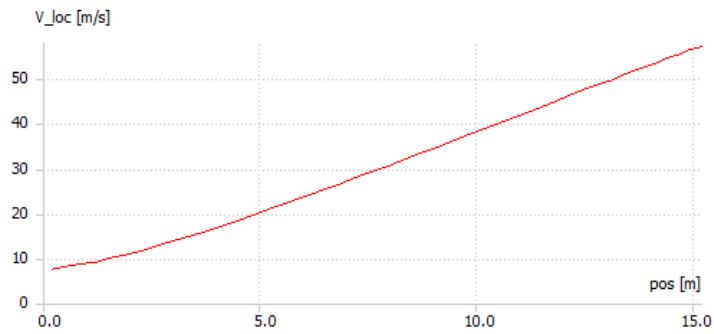
Figure 51: Local inflow velocity distribution for the *Bonus Combi* wind turbine

Combining the results from figure 51 and the chord distribution along the span from figure 42, it is possible to predict the contribution of each blade segment to the noise spectrum and run a log-summation of the single results to obtain the turbulent inflow noise prediction for the *Bonus Combi 300 kW* wind turbine blade. Turbulence integral length scale and intensity are once again assumed by Fuglsang and Madsen (1996) as, respectively, $L = 100\ m$ and $I = 10\%$. Their measurements were taken from an observer positioned at the ground, in a distance of $40\ m$ downstream the wind turbine.
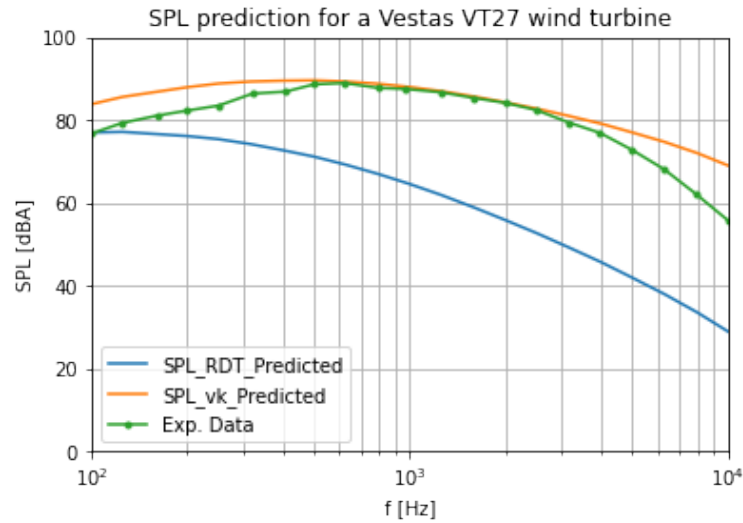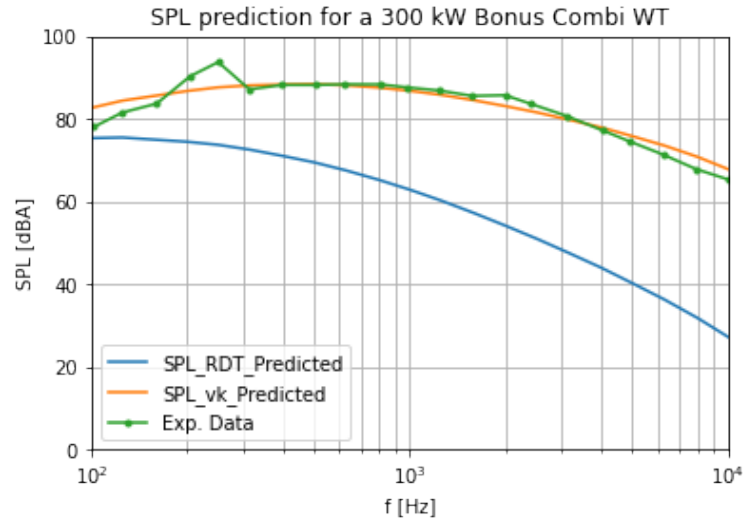

Figure 52: Comparison between the A-weighted SPL measurements from Fuglsang and Madsen for the *Bonus Combi 300 kW* wind turbine and the predicted turbulent inflow noise spectrum applying the standard and the modified versions of Lowson method. The experimental data correspond to the green line with dots, while the orange line refers to the isotropic turbulent spectrum assumption and the blue line corresponds to the prediction considering the rapid distorted turbulence spectrum.

The results, although refined, are mostly similar to the obtained for *Vestas VT 27*.

Figure 52 again points out to a better adherence of the measured data to the standard Lowson method, considering von Kármán isotropic turbulence model. A coarse underestimation is observed when considering the RDT-modified Lowson method, while the other fits almost perfectly, except for few frequencies.

Statistically, the standard Lowson method prediction has a root-mean-square error of 3.50 dB, while the RDT-modified curve corresponds to a RMS-error of 24.33 dB. A smaller RMS-error for the isotropic turbulence hypothesis and a greater RMS-error for the RDT hypothesis, in comparison to the $VT\ 27$ wind turbine.

The experimental overall sound pressure level is $OASPL_{exp} = 99.64\ dBA$, while the predicted values are $OASPL_{von\ Kármán} = 98.39\ dBA$ and $OASPL_{RDT} = 84.32\ dBA$, resulting in $\Delta OASPL_{von\ Kármán} = -1.25\ dBA$ and $\Delta OASPL_{RDT} = -15.32\ dBA$.

It is noteworthy that NACA 63400 and NACA 63200 series consist of airfoils with maximum thicknessess that range from 18% to 21%, and that should at once imply the need for a thickness correction, as discussed by Tian and Cotté (2016), Guidati $et\ al.$ (1997) and Moriarty $et\ al.$ (2004). Yet this is not verified, as the predicted and measured spectra overlap nearly flawless. Besides, the turbulence spectrum was proven to be completely different from the obtained in acoustic tunnel experiment environment.

4.5   Remarks on turbulence velocity spectrum modeling

Chapters 3 and 4 presented results that are very distinctive to each other. While aeroacoustic facility investigation pointed to a better adherence to the turbulent inflow noise prediction considering the rapidly distorted spectrum, the field measurements discussed in this present chapter gives the complete opposite conclusion.

Although the obtained in each chapter may seem to be contradictory, attention should be drawn to each case particularities regarding turbulence and fluid-solid interactions. In fact, the order of magnitude of the turbulent length scale shifts from milimeters to hundred meters and that causes not only a change on the ratio integral length scale over chord that violates the equation (2.96) RDT criterion, but also an increse on the turbulence Reynolds number, Re_t, from under 10^3 to over 10^7.

Phisically, the interaction between the wind turbine blades and the atmospheric turbulence integral length scales are hardly comparable to the interaction between grid-generated scales and test airfoils. Whether the grid-generated scales are likely to distort when approaching the airfoil surface, the atmospheric turbulence is capable of involving

the entire blade geometry, as it is more than fifty times larger than the maximum blade chord.

Thus, reflect of such distinct behavior is the respective turbulence energy spectrum, and therefore the fitting of the measured SPL to the standard or the RDT-modified Lowson method for turbulent inflow noise prediction. The respective statistical RMS errors and the $\Delta OASPL$ also shift. While for Bampanis *et al.* (2019) and Juknevicius and Chong (2018) the experimental SPL data are adherent to the RDT-modified prediction and the prediction method considering the hypothesis of isotropic turbulence overestimates the sound spectrum, for the latter cases discussed by Fuglsang and Madsen (1996) the inverse occurs in similar magnitude.
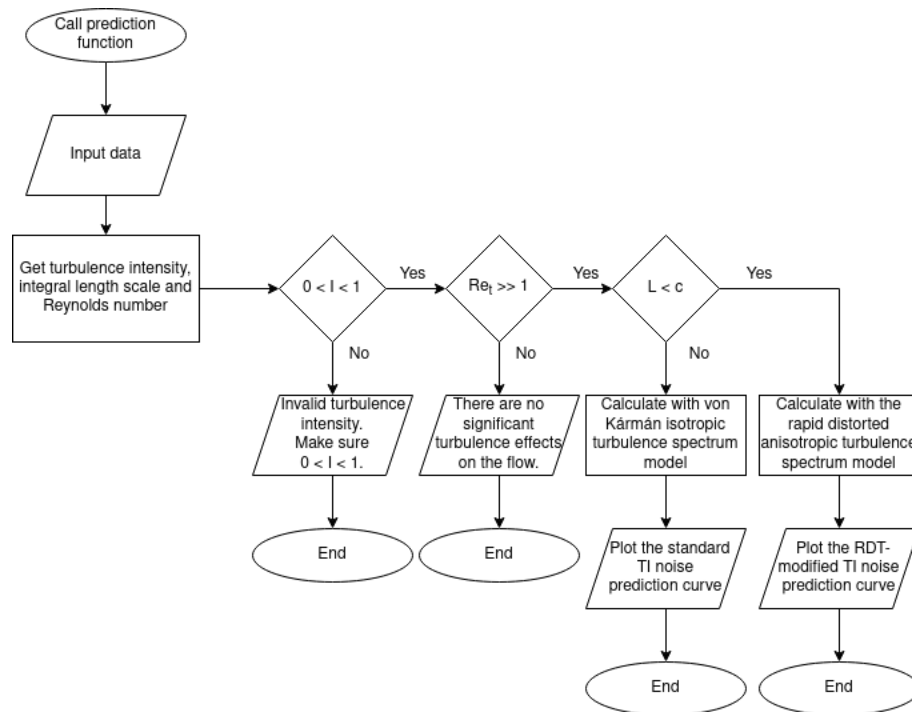
Figure 53: Workflow of the *PNoise* turbulent inflow noise prediction module.

This observation has led to figure 53 algorithm, which takes into account how the flow and the turbulent scales interact with the airfoil and then makes an option for the appropriate turbulent inflow noise prediction method when applies.

Although the algorithm is based on the RDT-criteria from equations (2.95), (2.96) and (2.97), there is plenty of room for further investigation as the limits of the ratio integral length scale over airfoil chord that causes the eddies distortion are not yet fully understood and mapped, i.e. for Bampanis *et al.* (2019), $L/c = 0.09$, for Juknevicius and Chong (2018), $L/c = 0.04333$, and then for the Fuglsang and Madsen study (1996), for the *Vestas VT 27*, $L/c_{max} = 75.19$ and for the *Bonus Combi* 300 kW, $L/c_{max} = 63.29$, so

the transition point is still not clear, and will be virtually set as $L/c = 1$.

This makes the airfoil self-noise much easier to deal with, given that the predicted values are comparable with both acoustic tunnel and siting situations. The turbulent inflow noise prediction correspondent to the acoustic tunnel measurements gives a hint that even the experiments are not yet representative of the noise produced for a full wind turbine operation, since the turbulent inflow noise prediction method representative of an acoustic tunnel measurement produces a large underprediction when applied to predict noise for a full wind turbine unit.

Other points that may raise questions are the fact that the wind turbine units provided by Fuglsang and Madsen (1996) are much smaller than the modern WTs, and also their rotation is much faster than the current units. For sure the wind turbine blades are nowadays larger in both length and chord length distribution. However, the growth on the chord length causes negligible impact on the proportion turbulence integral length scale over chord length. That means, the order of magnitude of the blade chords remain the same as for the older units. With respect to the rotation, since the noise is approximately a function of the tangential velocity at 85% of the blade length, it will not depend directly on the rotation of the blades, but in the tip speed ratio instead, which did not have grown that much since then, and being yet nowadays a mechanism for noise control.

5 CHANGES IN *PNOISE*

In view of the topics previously addressed, summarized in figure 53 algorithm, Lowson method for turbulent inflow noise prediction was embedded within *QBlade* environment, inside *PNoise* module. The method has shown yet a good coupling to the NASA BPM method for predicting the turbulent boundary layer trailing edge noise source, as both share a substantial amount of input variables, and the output predicted spectrum is given in terms of the 1/3 octave band frequencies.
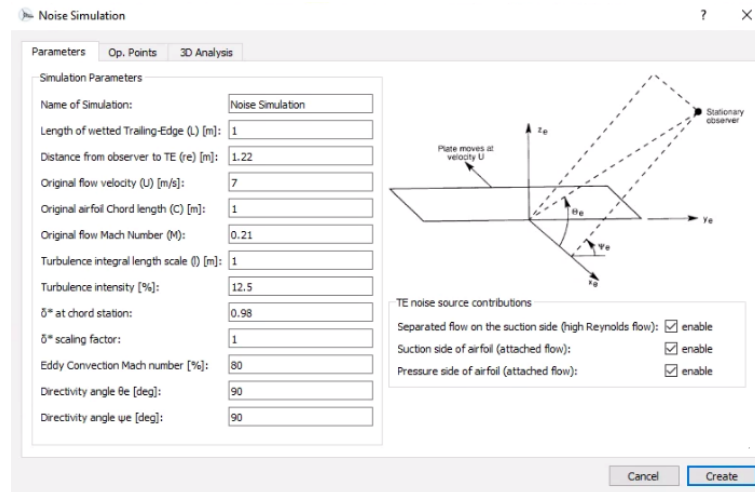
Figure 54: *PNoise* new input window, considering the turbulent inflow noise source contribution.

This update, as illustrated in figure 54, shows the adding of two new fields to the *Noise Simulation* input dialog for turbulent integral length scale and turbulence intensity.
As the Lowson directivity function has a similar construction compared to the BPM counterpart, a conversion was needed to obtain the actual observer position relative to the airfoil leading-edge by taking into account the airfoil chord length. By taking the Al-Kashi law of cosines, it results in

$$r_{e,LE} = \sqrt{r_{e,TE}^2 + c^2 - 2 \cdot c \cdot r_{e,TE} \cdot cos(1 - \theta_{TE})}, \tag{5.1}$$

where c is the airfoil chord, $r_{e,TE}$ is the distance between observer and the airfoil trailing-edge, $r_{e,LE}$ is the observer position relative to the airfoil leading-edge and *theta* is a directivity angle represented in figure 54.

Following the same logic, the directivity angle θ with reference of the leading-edge follows

$$cos(\theta_{TE}) = \frac{r_{e,LE}^2 + c^2 - r_{e,TE}^2}{2 \cdot r_{e,LE} \cdot c}. \tag{5.2}$$

Last, the directivity angle Ψ is the same for both TE and LE.

As the input values are set and the *Create* button is pushed, the turbulent inflow noise prediction function is triggered and the algorithm starts by reading the text boxes and, based on the RDT-criteria, it identifies whether the rapid distorted turbulence spectrum or the von Kármán isotropic turbulence spectrum is more appropriate to the investigation, or even if turbulent inflow noise does not show up for the specific flow conditions as a relevant source of noise.

Then it runs in parallel to the airfoil self-noise sources and return a graph for each of the individual spectra, as well as the resultant spectrum of a log summation the sources.
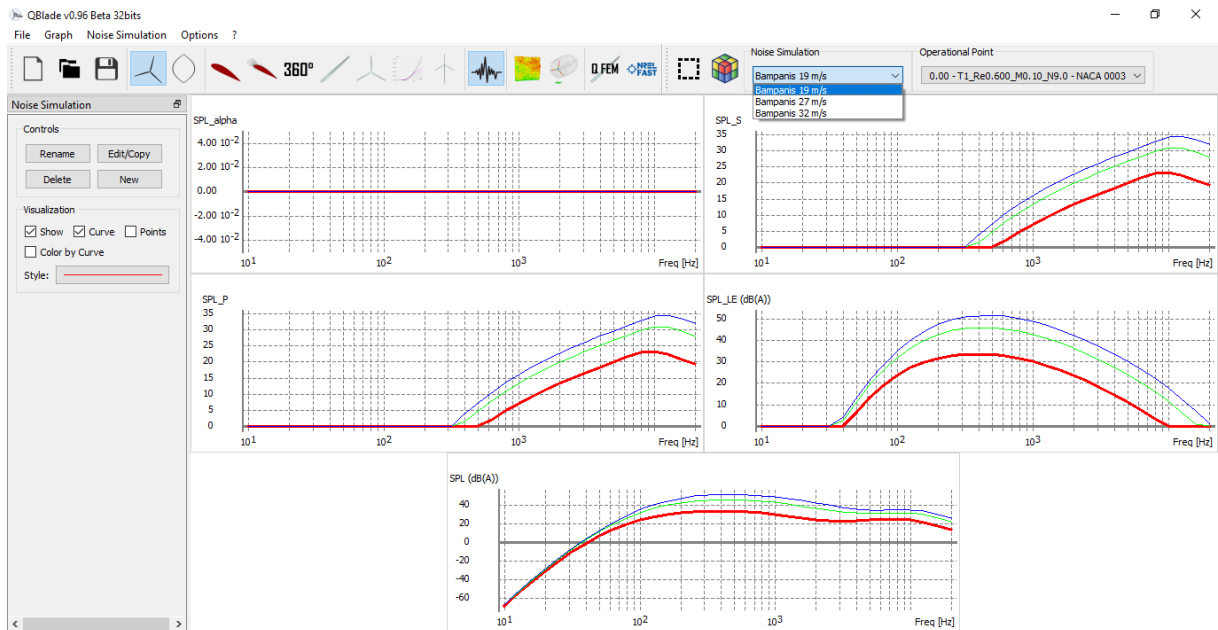
Figure 55: *PNoise* output graphs, containing the new chart for the turbulent inflow noise predicted spectrum for Bampanis *et al.* (2019) experiment. The red curves correspond to $U = 19\ m/s$, the green curves to $U = 27\ m/s$ and the blue curves to $U = 32\ m/s$.
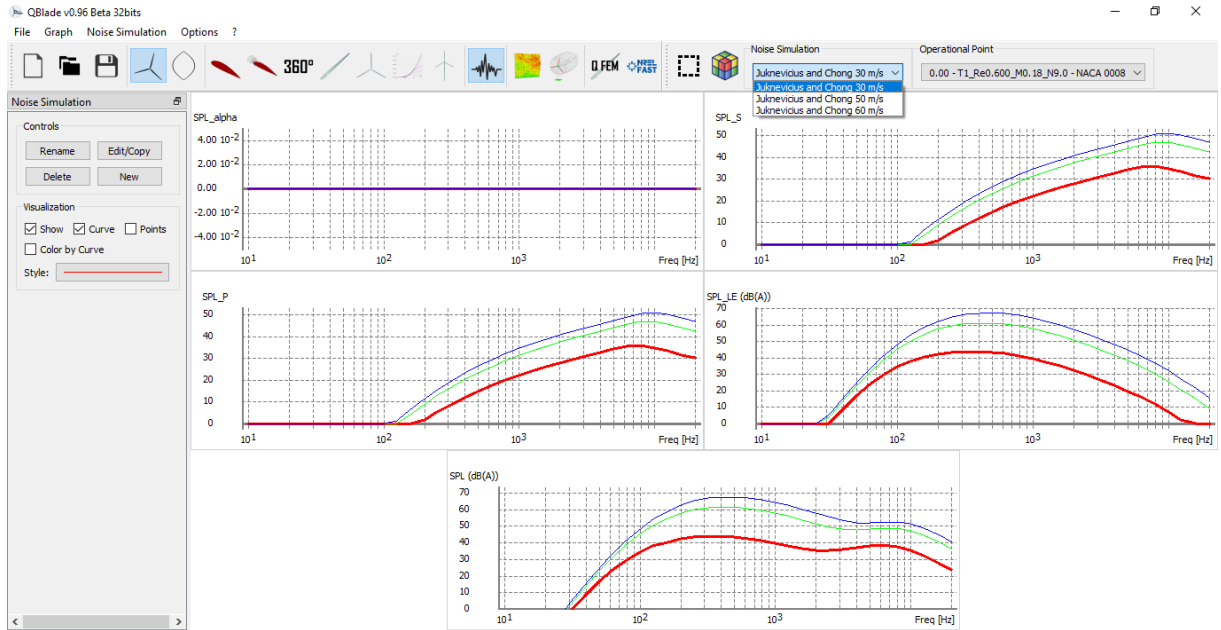
Figure 56: *PNoise* output graphs, containing the new chart for the turbulent inflow noise predicted spectrum for Juknevicius and Chong (2018) experiment. The red curves correspond to $U = 30 \ m/s$, the green curves to $U = 50 \ m/s$ and the blue curves to $U = 60 \ m/s$.
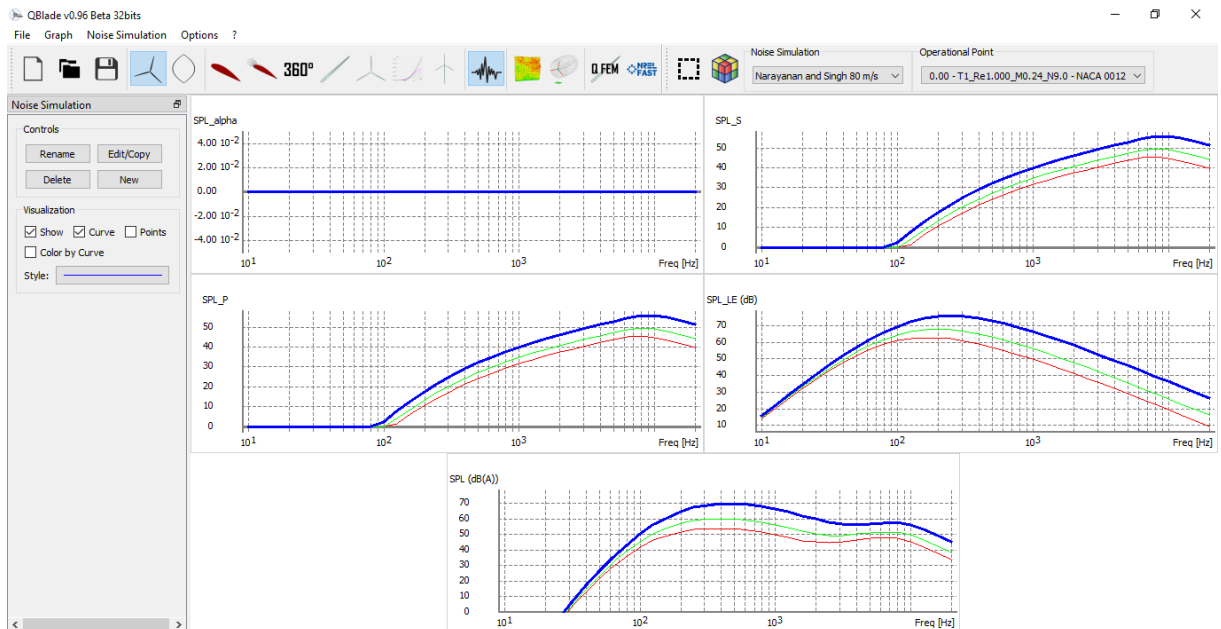
Figure 57: *PNoise* output graphs, containing the new chart for the turbulent inflow noise predicted spectrum for Narayanan and Singh (2020) experiment. The red curves correspond to $U = 40 \ m/s$, the green curves to $U = 60 \ m/s$ and the blue curves to $U = 80 \ m/s$.
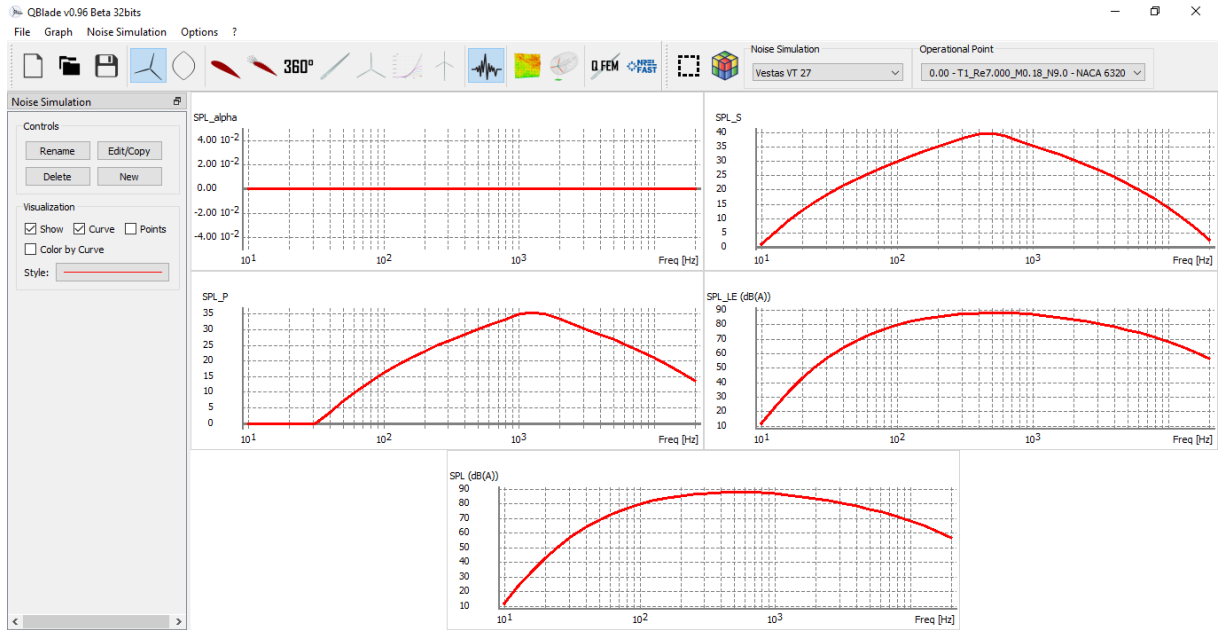
Figure 58: *PNoise* output graphs, containing the new chart for the turbulent inflow noise predicted spectrum for Vestas VT 27 measurement from Fuglsang and Madsen (1996).
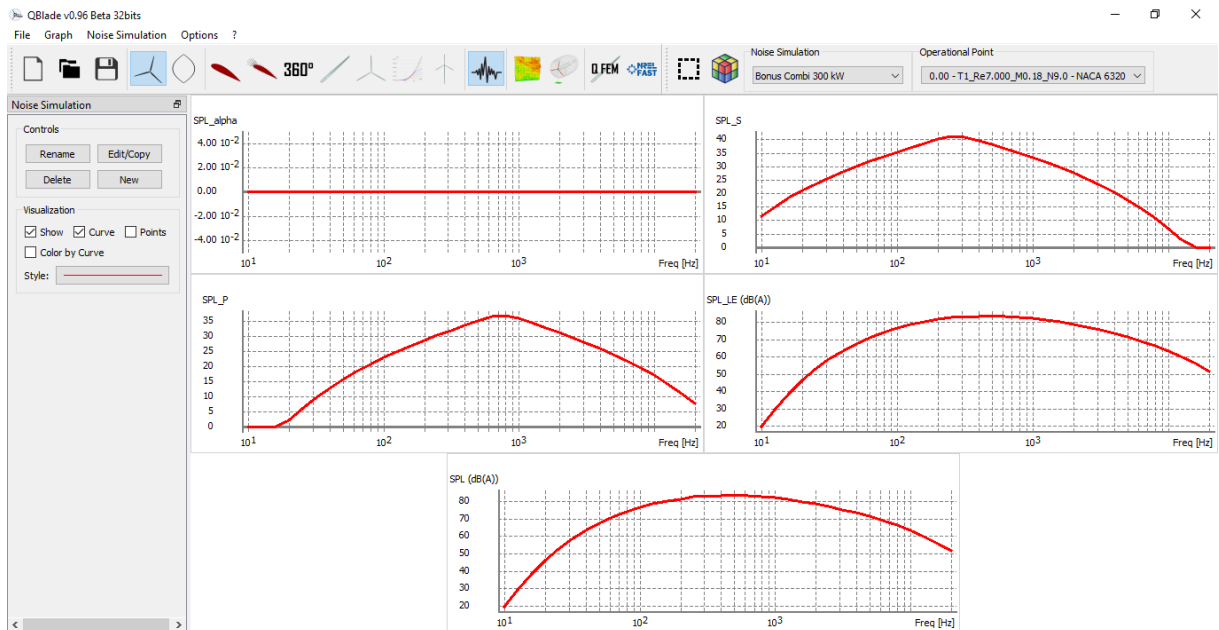
Figure 59: *PNoise* output graphs, containing the new chart for the turbulent inflow noise predicted spectrum for Bonus Combi 300 kW measurement from Fuglsang and Madsen (1996).

As an illustrative and practical example of the new *PNoise* turbulent inflow noise prediction functionality, the most relevant experimental setups discussed in previous chapters were reproduced as simulations in *QBlade* environment. In figures 55 to 59, Bampanis

et al., Juknevicius and Chong, Narayanan and Singh and Fuglsang and Madsen measurements are reproduced for every flow condition studied. The graphics for SPL_{LE} (dBA) present exact the same output obtained by the *Python* scripts, since the method is just transposed to *QBlade C++* language (see figures 30, 31, 32, 49 and 52).

The *PNoise* output window allows the comparison between the airfoil self-noise sources and the turbulent inflow, as well as an observation of the resultant noise spectrum. For Bampanis *et al.* and Juknevicius and Chong setups, the LE noise was reported as the dominant source for frequencies under 2000 Hz, where the trailing-edge noise becomes prominent.

For Fuglsang and Madsen measurements, on the other hand, the turbulent inflow noise was seen to be dominant over airfoil self-noise for the entire spectrum, as the turbulent boundary layer trailing-edge noise has a maximum peak level of under 40 dB.

Noteworthy that all simulations were run for a fixed angle of attack $AoA = 0$.

The current validity of the *PNoise* module for turbulent inflow noise prediction relies, at this point, on these tested experimental datasets and it should be further expanded as new research is conducted on experimental measurements of airfoil turbulent inflow noise and wind turbine noise. Another possibility is to map the behavior of the turbulence spectrum as the ratio integral length scale over airfoil chord L/c approaches the unit.

6 CONCLUSIONS

6.1 Overview

This work has discussed the global expansion of wind energy application, and its limitations, such as open terrain availability for the wind farm siting and people's concern on its impacts, whether they are environmental impacts or impacts on human health and fauna. Then these concerns are listed and, being wind turbine noise one of the most recurring, the option on describing this phenomenon and helping the assessment of WTN in the preliminary phase of wind turbine blade design was taken. The initiative of *QBlade/PNoise* was seen as an opportunity to provide the the WT manufacturers and the global research community a fast access tool that predicts the aerodynamic noise.

A detailing of the aerodynamic noise sources is then made, by splitting it in two major contributions, the airfoil self-noise and the turbulent inflow noise. While the first is subject of studies conducted by Saab (2016), the latter is the main focus of this thesis. This was made through an extensive review on airfoil turbulent inflow noise prediction methods, following the semi-empirical approach of Amiet-based methods, introducing the turbulence spectrum based on the rapid distortion theory and deriving a RDT-modified Lowson semi-empirical method, in opposition to its standard counterpart, that models the turbulence energy spectrum after the von Kármán homogeneous and isotropic spectrum. Criteria for the rapid distortion to occur were also established as subject of investigation. To validate the discussed methods, *Python* scripts were written as calculation routines and were run against measurement datasets in two distinct contexts. First, with respect to acoustic tunnel measurements, and later for field measurements from old wind turbine units, being all datasets gathered from the literature.

As expected from the RDT criteria, given that grid-generated turbulence have a small scale when compared to the airfoil chord, there is a better adherence of acoustic tunnel measurements to the prediction obtained though employment of the RDT-modified Lowson method, although the observation of isotropic turbulence in the absence of the airfoil in the test section of the tunnel prior to the experiment.

In its turn, for the full scale wind turbines, the prediction that better fits the measured datasets are whose turbulence spectra are modeled after von Kármán isotropic turbulence. That occurs as their integral length scale over airfoil chord ratio overcomes the RDT-criteria, since the atmospheric scales measured by Fuglsang and Madsen (1996) have an order of magnitude of 100 m and the blade airfoil characteristic length is not capable of inducing significant distortion on such large eddies.

A secondary topic is the sound pressure level prediction correction due to the real airfoil geometry, as Amiet-based methods are approximate the airfoil as a flat-plate. As it is commonly seen for acoustic tunnel representations, predictions considering von Kármán isotropic turbulence spectrum overestimate the SPL when compared to the measured data, and it is reported as due to real geometry effects. Although it is a reasonable statement that may require further investigation, the models provided by the literature are less effective on adjusting the prediction as correcting the turbulence spectrum from the observation that all of those experimental setups fill the RDT-criteria of inflow-airfoil interaction.

Following this logic, the predicted spectra for the *Vestas VT 27* or the *Bonus Combi 300 kW* wind turbines should overpredict the noise even more. That is not the case, once both SPL predictions seem to fit the measurement datasets so well as linear regression models. After the steps of analysis and validation, the turbulent inflow noise prediction method was designed as an algorithm and seamlessly integrated to *QBlade/PNoise*, as part of the new functionalities to be featured on the upcoming version of the code, being the algorithm capable of identify whether to use RDT-modified Lowson method or the standard Lowson method, following the RDT-criteria. The method is currently validated for the experimental setups and measurements analyzed in this study.

6.2 Relevant contributions

This thesis main contribution is the update of the current state of *QBlade* code by integrating the airfoil turbulent inflow noise prediction method as an improvement of the wind turbine noise assessment *PNoise*, by introducing the aeroacoustics response to the interaction between turbulence and the blade airfoils. This allows an increase on precision of the wind turbine noise prediction and, therefore, its minimization through changes in blade geometry since the WT preliminary design phase.

As a consequence, the discussion regarding turbulence spectrum modeling is brought to

the realm of semi-empirical methods, and points out to a walk hand in hand with research involving high performance computational methods, a field where computational fluid dynamics and computational aeroacoustics have expanded in the past couple of years.

The validation steps of the TI noise prediction method were determinant to establish appropriate criteria for the turbulent energy spectrum modeling. It was confirmed that the adherence of the prediction to each single measurement dataset has followed the RDT-criteria from equations (2.95), (2.96) and (2.97), whether for acoustic tunnel experiments or for field measurements. It was mathematically noticed that airfoils in the test section of acoustic tunnel induced distortion on previously isotropic grid-generated turbulence, as the scales approached the airfoil surface. This justifies the overprediction of the turbulent inflow noise by the standard Lowson method, considering isotropic turbulence spectrum. Once changed to the RDT-modified counterpart in both Bampanis *et al.* (2019), Juknevicius and Chong (2018) and Narayanan and Singh (2020), the prediction error has reduced considerably.

For the analyzed wind turbines interacting with larger scales of atmospheric turbulence, on the other hand, the criteria point to the violation of the established criteria, and it was then confirmed by the adherence of the field measurements to the prediction obtained by employment of the standard Lowson method.

The validation steps also point to a major character of the TI noise to the overall noise spectrum, as it was seen as the dominant source for the airfoils in acoustic tunnel for frequencies below 2000 Hz, where the airfoil self-noise source becomes prominent. With respect to the *Vestas VT 27* and the *Bonus Combi 300 kW* wind turbine measurements, the leading-edge source was reported since from Fuglsang and Madsen (1996) study as the dominant source, and it was confirmed through *PNoise* simulations.

Besides, this thesis also contributes to the discussion of thickness effects on turbulent inflow noise prediction by showing how Tian and Cotté and Guidati-Moriarty SPL reduction might have been tackling a mistaken overestimation caused by innappropriate turbulence spectrum model assumption. This is demonstrated by the fact that the SPL reduction equations were less effective than considering the hypothesis of anisotropic turbulence spectrum following the rapid distortion theory, for qualitative examples of acoustic tunnel experiments and, more important, the field measurements did not point to an overestimation of the turbulent inflow noise spectrum biased by the thin airfoil hypothesis, as the prediction error is considerably low. The latter are the most significative for this discussion, as the employed airfoils relative thicknesses ranged from 18% to 21%. That is an indicative that, differently from the airfoil self-noise source, the turbulent inflow noise are not highly dependent on the airfoil shape other than the values of chord and span.

6.3 Open questions and future work

There are still open questions after accomplishing this study objectives. The current major challenge is to validate *PNoise* wind turbine noise prediction module for larger modern WT units and to extrapolate the 2D noise prediction method for stationary airfoils to a 3D full rotor noise model. This is part of Poli-Wind ongoing research.

Besides, there is still a need for expanding the validity of the RDT-modified Lowson method for airfoil tubulent inflow noise prediction, in order to attend a broad variety of flow conditions. The test cases with respect to Juknevicius and Chong (2018), Bampanis *et al.* (2019) and Narayanan and Singh (2020) datasets are limited in terms of flow Reynolds numbers, being not representative of wind turbines operational conditions that correspond at least to $Re = 7 \cdot 10^6$. That means an airfoil with a chord more than ten times higher is needed to perform such investigation, once only two of Juknevicius and Chong and two Narayanan and Singh flow conditions were capable of matching WT operational Mach numbers. This trade-off may require more physical space for the experimental facilities because an increase of the airfoil span of the same proportion will be needed in order to the border effects become negligible.

Other possible investigation after this thesis results is the transition from the rapidly distorted turbulence to the isotropic spectrum while the ratio turbulence integral length scale over airfoil chord approaches the unit and further increases. Other than that, the understanding on how multiple scales interact with the airfoil or the wind turbine blade and how it represents a change on the noise spectrum is also an important topic derived from the main study.

Although being put aside in this research, as the currently available methods have proven to be less effective on representing a SPL reduction independent of the overestimation caused by the isotropic turbulence hypothesis, the thickness effects on turbulent inflow noise is a topic that need to be further addressed.

REFERENCES

[1] R.K. Amiet: Acoustic Radiation from an Airfoil in a Turbulent Stream. Journal of Sound and Vibration 41 (1975), pp. 407-420. https://doi.org/10.1016/S0022-460X(75)80105-2.

[2] R.W. Paterson, R.K. Amiet: Noise and Surface Pressure Response of an Airfoil to Incident Turbulence. Journal of Aircraft 14 (1977), pp. 729-736. https://doi.org/10.2514/3.58845.

[3] M.V. Lowson: Applications of aero-acoustics to wind turbine noise control. Journal of Wind Engineering 16 (1992), pp. 126-140.

[4] M.V. Lowson: Assessment and Prediction of Wind Turbine Noise. Flow Solutions Report 92/19 (1992).

[5] J.L. Tangler, D.M. Somers: NREL Airfoil Families for HAWTs. NREL Technical Report 442-7109 (1995).

[6] Y. Tian, B. Cotté, A Chaigne: Wind Turbine Noise Modeling Based on Amiets Theory. Wind Turbine Noise Conference 5 (2013).

[7] M. Roger, S. Moreau: Extensions and Limitations of Analytical Airfoil Broadband Noise Models. International Journal of Acoustics 9 (2010), pp. 273-305. https://doi.org/10.1260/1475-472X.9.3.273.

[8] S. Sinayoko, J. Hurault: On Predicting Wind Turbine Noise and Amplitude Modulation Using Amiet's theory. Wind Turbine Noise Conference 6 (2015).

[9] Y. Tian, B. Cotté: Wind Turbine Noise Modeling Based on Amiet's Theory: Effects of Wind Shear and Atmospheric Turbulence. Acta Acustica united with Acustica 102 (2016), pp. 626-639. https://doi.org/10.3813/AAA.918979.

[10] S. Buck, S. Oerlemans, S. Palo: Experimental Validation of a Wind Turbine Turbulent Inflow Noise Prediction Code. AIAA Journal 56 (2018), pp. 1495-1506. https://doi.org/10.2514/1.J056134.

[11] S. Zhong, X. Zhang: On the Effect of Streamwise Disturbance on the Airfoil-Turbulence Interaction Noise. The Journal of the Acoustical Society of America 145 (2019), pp. 2530-2539. https://doi.org/10.1121/1.5098783.

[12] G.K. Batchelor, I. Proudman: The Effect of Rapid Distortion of a Fluid in Turbulent Motion. The Quarterly Journal of Mechanics and Applied Mathematics 7 (1954), pp. 83-103. https://doi.org/10.1093/qjmam/7.1.83.

[13] J.C.R. Hunt: A Theory of Turbulent Flow Round Two-Dimensional Bluff Bodies. Journal of Fluid Mechanics 61 (1973), pp. 625-706. https://doi.org/10.1017/S0022112073000893.

[14] J.C. Simonich, R.K. Amiet, R.H. Schlinker, E.M. Greitzer: Helicopter Rotor Noise due to Ingestion of Atmospheric Turbulence. NASA Contractor Report 3973 (1986).

[15] L. D. Santana, J. Christophe, C. Schram: A Rapid Distortion Theory Modified Turbulence Spectra for Semi-Analytical Airfoil Noise Prediction. Journal of Sound and Vibration 383 (2016), pp. 349-363. https://doi.org/10.1016/j.jsv.2016.07.026.

[16] W. Devenport, J. Staubs, S. Glegg: Sound Radiation from Real Airfoils in Turbulence. Journal of Sound and Vibration 329 (2010) pp. 3470-3483. https://doi.org/10.1016/j.jsv.2010.02.022.

[17] L. D. Santana, W. Desmet, C. Schram: Extension of the Amiet Theory for Compact Leading Edge Airfoil Noise Prediction. International Conference on Noise and Vibration Engineering 07 (2014).

[18] L. D. Santana: Semi-analytical Methodologies for Airfoil Noise Prediction. PhD Thesis. KU Leuven, 2015.

[19] J. Christophe: Application of Hybrid Methods to High Frequency Aeroacoustics. PhD Thesis. von Kármán Institute for Fluid Dynamics, 2011.

[20] G. Bampanis, M. Roger, D. Ragni, F. Avallone, C. Teruna: Airfoil-Turbulence Interaction Noise Source Identification and Reduction by Leading-Edge Serrations. AIAA/CEAS Aeroacoustics Conference 25 (2019). https://doi.org/10.2514/6.2019-2741.

[21] A. Juknevicius, T. P. Chong: On The Leading Edge Noise and Aerodynamics of Thin Airfoil Subjected to Straight and Curved Serrations. Journal of Sound and Vibration 425 (2018), pp. 324-343. https://doi.org/10.1016/j.jsv.2018.02.038.

[22] T.F. Geyer, A. Lucius, M. Schrödter, M. Schneider, E. Sarradj: Reduction of Airfoil Interaction Noise Through Airfoils with Perforated Leading Edges. Acta Acustica united with Acustica 105 (2019), pp.109-122. https://doi.org/10.3813/AAA.919292.

[23] W. Devenport, R.A. Burdisso, H. Camargo, E. Crede, M. Remillieux, M. Rasnick, P. van Seeters: Aeroacoustic Testing of Wind Turbine Airfoils. NREL Technical Report SR-500-43471 (2010).

[24] T.F. Brooks, S.B. Pope, M.A. Marcolini: Airfoil Self-Noise and Prediction. NASA Report 1218 (1989).

[25] C. Doolan, D. Moreau: Review of NACA 0012 Turbulence Trailing Edge Noise Data at Zero Angle of Attack. Wind Turbine Noise Conference 5 (2013).

[26] J.Y. Saab Jr., M.M. Pimenta, A.M. Faria, S. Rodriguez: Determination of Local Flow Conditions and Validation of the PNoise Code for Large Size Wind Turbine. Journal of the Brazilian Society of Mechanical Sciences and Engineering 40 (2018), pp. 495-516. https://doi.org/10.1007/s40430-018-1412-1.

[27] I. Barreto, F. Melo, F. Pimenta, M. Scarton, L. Lordelo, A.C. Paes, C. Galiano, R. Cunha: Licença Social em Parques Eólicos: Uma Proposta Metodológica. Anuário Trabalhos Técnicos Brazil Windpower 2019 (2019).

[28] A.J.A. Meireles: Danos socioambientais originados pelas usinas eólicas nos campos de dunas do Nordeste brasileiro e critérios para definição de alternativas locacionais. Confins. Revue franco-brésilienne de géographie/Revista franco-brasilera de geografia (2011).

[29] D. Bowdler, G. Leventhall: Wind Turbine Noise. Brnetwood: Multi-Science Publishing Co Ltd. (2011).

[30] S. Gibbons: Gone with the wind: Valuing the visual impacts of wind turbines through house prices. Journal of Environmental Economics and Management, v. 72, p. 177-196 (2015).

[31] J.S. Mendes, A. Gorayeb, C. Brannstrom: Diagnóstico participativo e cartografia social aplicados aos estudos de impactos das usinas eólicas no litoral do Ceará: o caso da Praia de Xavier, Camocim. Geosaberes: Revista de Estudos Geoeducacionais, v. 6, n. 3, p. 243-245 (2015).

[32] I. Angulo: Impact analysis of wind farms on telecommunication services. Renewable and Sustainable Energy Reviews, v. 32, p. 84-99 (2014).

[33] E. Koppen, K. Fowler: International Legislation for Wind Turbine Noise. Proceedings of EuroNoise, Maastricht (2015). ISSN 2226-5147.

[34] P. Gipe: Wind Power (Revised and Expanded Edition ed.) Vermont: Chelsea (2004) Green Publishing Co.

[35] W. K. Blake: Mechanics of Flow-Induced Sound and Vibration (Vol. I). Orlando, FL.: Academic Press (1986).

[36] W. K. Blake: Mechanics of Flow-Induced Sound and Vibration (1ed ed., Vol. II). Orlando: Academic Press (1986).

[37] O. Jianu, M. A. Rosen, G. Naterer: Noise Pollution Prevention in Wind Turbines: Status and Recent Advances, 1st World Sustainability Forum (2011).

[38] ABEEÓLICA: Boletim de dados. São Paulo (2021).

[39] R. Bareiß, G. Guidati, S. Wagner: An approach towards refined noise prediction of wind turbines. Proceedings of the European Wind Energy Association Conference & Exhibition, (pp. 785-790). Thessaloniki (1994).

[40] T. F. Brooks, M. A. Marcolini: Airfoil Trailing-Edge Flow Measurements. AIAA Journal, pp. 1245-1251 (1986).

[41] T. F. Brooks, S. Pope, M. A. Marcolini: Airfoil Self-Noise and Prediction. NASA. Langley: NASA (1989).

[42] S.R. Bistafa: Acústica Aplicada ao Controle de Ruído (Segunda edição). São Paulo: Edgar Blücher (2011).

[43] K. Boorsma, J. Schepers: Enhanced wind turbine noise prediction tool SILANT. Technical Report ECN-M-12-004 (2011).

[44] J. Couniham: Adiabatic atmospheric boundary layers: a review and analysis of data from the period 1880-1972. Atmospheric environment, vol. 9, no. 10, pp. 871-905 (1967).

[45] N. Curle: The influence of solid boundaries upon aerodynamic sound, vol. 231, pp. 505-514. The Royal Society (1955).

[46] ESDU 85020: Characteristics of atmospheric turbulence near the ground, part 2: Single point data for strong winds (neutral atmosphere). Tech. Report (1985).

[47] F. Farassat: Derivation of Formulations 1 and 1A of Farassat. NASA, Hampton, VA (2007).

[48] J. Ffowcs Williams, L. Hall: Aerodynamic sound generation by turbulent flow in the vicinity of a scattering half-plane. Journal of Fluid Mechanics 40(4), (pp. 657-670) (1970).

[49] J. Ffowcs Williams, D.L. Hawkings: Sound generation by turbulence and surfaces in arbitrary motion. Philosophical Transactions of the Royal Society of London A: Mathematical, Physical and Engineering Sciences, vol. 264, no. 1151 (pp. 321-342) (1969).

[50] P. Fuglsang, H.A. Madsen: Implementation and verification of an aeroacoustic noise prediction model for wind turbines (1996).

[51] S. Glegg, S. Baxter, A. Glendinning: The prediction of broadband noise from wind turbines. Journal of Sound and Vibration, vol. 118, no. 2 (pp. 217-239) (1987).

[52] G. Guidati, R. Bareiß, S. Wagner, T. Dasseb, R. Parchen: Simulation and measurement of inflow turbulence noise on airfoils. American Institute of Aeronautics and Astronautics Conference Paper (pp. 1697-98) (1997).

[53] GWEC (Global Wind Energy Council): Wind energy expansion database (2018).

[54] GWEC (Global Wind Energy Council): Wind Energy Report (2021).

[55] Instituto Chico Mendes de Conservação da Biodiversidade (ICMBIO): Relatório anual de rotas e áreas de concentração de aves migratórias no Brasil. Cebedelo, PB (2016).

[56] M. Kamruzzaman, T. Lutz, K. Nübler, E. Krämer: Implementation and Verification of an Aeroacoustic Wind Turbine Blade Analysis Tool. Wind Turbine Noise Conference 2011. INCE Europe. Rome (2011).

[57] M.J. Lighthill: On sound generated aerodinamically. I general theory, vol. 211 (pp. 564-587), The Royal Society (1952).

[58] S. Moreau, M. Roger, V. Jurdic: Effect of angle of attack and airfoil shape on turbulence interaction noise. Proceedings of the 11th AIAA/CEAS Aeroacoustics Conference (Monterey, CA), AIAA Paper, vol. 2881 (2005).

[59] P. Moriarty, G. Guidati, P. Migliore: Prediction of turbulent inflow and trailing-edge noise for wind turbines. Proceedings of the 11th AIAA/CEAS Aeroacoustics Conference (Monterey, CA), AIAA Paper, vol. 2881 (2005).

[60] P. Moriarty, P. Migliore: Semi-empirical aeroacoustic noise prediction code for wind turbines. NREL Technical Report. Golden, Colorado. Report No.: NREL/TP-500-34478 (2003).

[61] S. Narayanan, S. K. Singh: On the reductions of aerofoil-turbulence interaction noise through multi-wavelength leading edge serrations. Journal of Aerospace Engineering (0), pp. 1-17 (2020. https://doi.org/10.1177/0954410020965747.

[62] S Oerlemans: Wind turbine noise: primery noise sources. National Aerospace Laboratory NLR, Amsterdam (2011);

[63] S. Oerlemans, P. Migliore: Wind tunnel aeroacoustic tests of six airfoils for use on small wind turbines. NREL Scientific Report. Golden, Colorado. Report No.: NREL/SR-500-35339 (2004).

[64] S. Oerlemans, P. Sijtsma, B. Méndez-López: Location and quantification of noise sources on a wind turbine. Journal of Sound and Vibration (pp. 869-883) (2007).

[65] R. Orselli: Previsão numérica de escoamento e ruído gerado em corpos rombudos prismáticos [dissertation]. Escola Politécnica, Universidade de São Paulo (2011).

[66] A. Rogers, J. Manwell, S. Wright: Wind turbine acoustic noise. University of Massachussets, Amherst (2006).

[67] ABNT: NBR 10151 Standard - Acoustics - Measurement and evaluation of sound pressure levels in inhabited environments - Application for general use (2019)

[68] J.Y Saab Jr.: Trailing-edge noise - Development and application of a noise prediction tool for the assessment and design of wind turbine airfoils [doctoral thesis]. Escola Politécnica, Universidade de São Paulo (2016).

[69] J.Y. Saab Jr., M.M. Pimenta: Displacement thickness evaluation for semi-empirical airfoil trailing-edge noise prediction model. Journal of the Brazilian Society of Mechanical Sciences and Engineering, Vol. 38, No. 2, pp. 385-394 (2016).

[70] K. Schwarzschild: Die Beugung und Polarisation des Lichst durch einen Spalt. I. Mathematische Annalen, 55, 2, pp: 177-247 (1901).

[71] J.K. Staubs: Real airfoil effects on leading-edge noise [dissertation]. Virginia Polytechnic Institute and State University. Blacksburg, VA (2008).

[72] C.R. Sucameli: Development and implementation of an aeroacoustic module for wind turbine noise prediction [dissertation]. Politecnico de Milano, Italy (2017).

[73] S. Wagner, R. Bareiß, G. Guidati: Wind Turbine Noise. Berlin: Springer (1996).

[74] W.J. Zhu, N. Heilskov, W.Z. Shen, J.N. Sörensen: Modeling of aerodynamically generated noise from wind turbines. Journal of Solar Energy Engineering, vol. 127, no. 4, pp. 517-528 (2005).

[75] M. Hansen: Aerodynamics of Wind Turbines (Second Edition). London: Earthscan (2008).

[76] N.K.R. Kevlahan: Rapid Distortion of Turbulent Structures. Applied Scientific Research, 51, pp: 411-415 (1993).

[77] A.C. Martinazzo: Implementação de modelo para predição de ruído aerodinâmico próprio em turbinas eólicas [dissertation]. Escola Politécnica, Universidade de São Paulo (2015).

APPENDIX A – CONSIDERATIONS ON FLUID DYNAMICS

A.1 Conservation laws and governing equations

In fluid dynamics, gases and liquids are considered as continuous media, e.g. for calculation purposes, one can define a "fluid particle", in a scale bigger than molecular scales, but smaller than other scales contained in the problem. After that, it is possible to describe the fluid motion through conservative laws, such as mass, momentum and energy conservation, applied to the fluid particle. From the application of these laws to an element with infinitesimal volume, the differential equations that consider fluid properties to behave after the continuum hypothesis and their derivatives exist are obtained. In other cases, the conservative laws may be applied in their integral form.

The mass conservation law follows,

$$\frac{\partial \rho}{\partial t} + \frac{\partial}{\partial x_i}(\rho v_i) = m. \tag{A.1}$$

Let us then consider the case with mass conservation ($m = 0$), a process without source or sink.

The linear momentum conservation is presented in the form of

$$\frac{\partial}{\partial t}(\rho v_i) + \frac{\partial}{\partial x_j}(P_{ji} + \rho v_j v_i) = f_i + m v_i, \tag{A.2}$$

where f_i represents the field forces, i.e. gravity, and P_{ji} is the fluid internal stress tensor. From the combination of equations (A.1) and (A.2), it results in

$$\rho \frac{\partial}{\partial t} v_i + \frac{\partial P_{ji}}{\partial x_j} + \rho v_j \frac{\partial v_i}{\partial x_j} = f_i \tag{A.3}$$

. The fluid stress tensor is related to the viscous stress tensor τ_{ij} after the following expression

$$P_{ij} = p \delta_{ij} - \tau_{ij}, \tag{A.4}$$

where τ_{ij} can be written as

$$\tau_{ij} = \mu \left(\frac{\partial v_i}{\partial x_j} + \frac{\partial v_j}{\partial x_i} \right) - \frac{2}{3} \mu \left(\frac{\partial v_k}{\partial x_k} \right) \delta_{ij}. \tag{A.5}$$

Equation (A.5) is a constitutive equation, a function of the dynamic viscosity, which can be experimentally measured, function of pressure and temperature.

With $m = 0$, the energy equation can be written as

$$\frac{\partial}{\partial t} \rho \left(e + \frac{1}{2} v^2 \right) + \frac{\partial}{\partial x_i} \rho v_i \left(e + \frac{1}{2} v^2 \right) = -\frac{\partial q_i}{\partial x_i} - \frac{\partial}{\partial x_i} p v_i + \frac{\partial}{\partial x_i} \tau_{ij} v_j + f_i v_i, \tag{A.6}$$

where q_i is the amount of heat conducted, from the Fourier law that follows

$$q_i = -K \frac{\partial T}{\partial x_i}. \tag{A.7}$$

The thermodynamic relation for reversible processes follows

$$T dS = de + p d \left(\rho^{-1} \right). \tag{A.8}$$

From equation (A.8), and also from the mechanical energy conservation, obtained by taking the scalar product between the conservation of linear momentum equation and the velocity vector, the entropy equation can be written as

$$\rho T \left(\frac{\partial s}{\partial t} + v_i \frac{\partial s}{\partial x_i} \right) = -\frac{\partial q_i}{\partial x_i} + \tau_{ij} \frac{\partial}{\partial x_i} v_j. \tag{A.9}$$

The fluid is considered to be isentropic when viscous dissipation and heat conduction are negligible, or

$$\left(\frac{\partial s}{\partial t} + v_i \frac{\partial s}{\partial x_i} \right) = 0. \tag{A.10}$$

This approximation is reasonable for the cases to be presented, as long as being localized in regions far from walls.

Let us define the constitutive equation $e = e(\rho, s)$. Then, one can write

$$p = \rho^2 \left(\frac{\partial e}{\partial \rho} \right)_s ; \tag{A.11}$$

$$T = \left(\frac{\partial e}{\partial s} \right)_\rho . \tag{A.12}$$

In some other cases, instead of $e = e(\rho, s)$, a function $p = p(\rho, s)$ is specified. So

$$dp = c^2 d\rho + \left(\frac{\partial p}{\partial s} \right)_\rho ds, \tag{A.13}$$

where

$$c^2 = \left(\frac{\partial p}{\partial \rho}\right)_s, \tag{A.14}$$

and c^2 represents the square of the isentropic sound velocity. Although equation (A.14) represents $c = c(\rho, s)$, and being c a thermodynamic property, it represents also a measurement of the sound velocity. When the same equation $c = c(\rho, s)$ is valid for any point of the flow, the fluid is characterized as homogeneous. When the density is pressure-dependent only, the fluid is characterized as barotropic. If the fluid is homogeneous and isentropic, it is a homentropic fluid.

Let us define the heat capacity at constant volume for a reversible process, as

$$C_V = \left(\frac{\partial e}{\partial T}\right)_V. \tag{A.15}$$

For an ideal gas, the energy is only dependent on the temperature, as follows

$$e(T) = \int_0^T C_V dT. \tag{A.16}$$

For an ideal gas with constant heat capacity,

$$e = C_V T. \tag{A.17}$$

The condition described by equation (A.17) is the perfect gas approximation.

A.2 Approximate and alternative forms for the ideal fluid conservative laws

Recovering the definition of the total derivative operator,

$$\frac{D}{Dt} = \frac{\partial}{\partial t} + \vec{v} \cdot \nabla. \tag{A.18}$$

The mass conservation in the absence of any source or sink can be written as

$$\frac{1}{\rho}\frac{D\rho}{Dt} = -\nabla \cdot \vec{v}. \tag{A.19}$$

Considering constant density, one can write

$$\nabla \cdot \vec{v} = 0. \tag{A.20}$$

Equation (A.20) is the mass conservation for non-compressible fluids.

For an non-viscous flow, the conservation of the linear momentum can be written as

$$\rho \frac{D\overrightarrow{v}}{Dt} = -\nabla p + \overrightarrow{f}. \tag{A.21}$$

This is the Euler equation, which corresponds to the second Newton law, applied to a constant mass fluid element.

For an idea gas, the correspondent energy equation follows

$$\frac{Ds}{Dt} = 0. \tag{A.22}$$

That means entropy of an ideal gas is constant. That occurs because of the fact that heat conduction is negligible for a non-viscous gas flow. Heat and momentum transfer are governed by the same molecular collision processes. For isentropic flows, the equation of state commonly used follows

$$\frac{Dp}{Dt} = c^2 \frac{D\rho}{Dt}, \tag{A.23}$$

being $c = c(\rho, s)$ in equation (A.23) not necessarily constant.

The velocity vector, as well as any other vectorial field, can be described as part solenoid, part irrotational, that means

$$v_i = \frac{\partial \varphi}{\partial x_i} + \epsilon_{ijk} \frac{\partial \Psi_k}{\partial x_j}, \frac{\partial \Psi_j}{\partial x_j} = 0, \tag{A.24}$$

where φ is a scalar potential and Ψ is a vector potential.

For a potential flow, let us then write the simplified continuity equation,

$$\frac{1}{\rho} \frac{D\rho}{Dt} = -\nabla^2 \phi. \tag{A.25}$$

Equation (A.25) evidences that the flow related to the acoustic field is a non-rotational flow. A definition of an acoustic field is the instability component of the non-rotational field $\nabla \varphi$. The vector potential function describes the vorticity $\overrightarrow{\omega} \times \overrightarrow{v}$, because $\nabla \times \nabla \varphi = 0$. Then, one can write the vorticity as

$$\overrightarrow{\omega} = \nabla \times \left(\nabla \times \overrightarrow{\Psi} \right) = -\nabla^2 \overrightarrow{\Psi}. \tag{A.26}$$

It can be verified that the vorticity $\overrightarrow{\omega}$ corresponds to double of the angular velocity $\overrightarrow{\Omega}$ of a fluid particle. When ρ can be written as $\rho(p)$, as only pressure dependent, as for an homentropic flow, and there are no tangential viscous forces, pressure and density can be eliminated from Euler equation. By taking the rotational of this simplification, it is

obtained that

$$\frac{\partial}{\partial t}\vec{\omega} + \vec{v} \cdot \nabla \vec{\omega} = \vec{\omega} \cdot \nabla \vec{v} - \vec{\omega} \cdot \vec{v} + \nabla \times \left(\frac{\vec{f}}{\rho}\right). \tag{A.27}$$

Applying the continuity equation, the following is obtained:

$$\rho \left(\frac{\partial}{\partial t} + \vec{v} \cdot \nabla\right) \left(\frac{\vec{\omega}}{\rho}\right) = \vec{\omega} \cdot \nabla \vec{v} - \frac{m\vec{\omega}}{\rho} + \nabla \times \left(\frac{\vec{f}}{\rho}\right). \tag{A.28}$$

It is noticeable that the vorticity of the fluid particle is modified by stretching, by a mass source on the presence of the vorticity, or for a external and non-conservative force field. For a two-dimensional non-compressible flow ($\nabla \cdot \vec{v} = 0$), with velocity $\vec{v} = (v_x, v_y, 0)$, the vorticity $\vec{\omega} = (0, 0, \omega_z)$ is not affected by stretching because there is no flow in the same direction of $\vec{\omega}$. Despite the source terms $-\frac{m\vec{\omega}}{\rho}$ and $\nabla \times \left(\frac{\vec{f}}{\rho}\right)$, the linear momentum equation is reduced to a pure kinematic law, being known that $\vec{\Psi}$ and $\vec{\omega}$ are linked to kinematic aspects of the flow.

From definition of specific enthalpy,

$$h = e + \frac{p}{\rho}, \tag{A.29}$$

the fundamental thermodynamic equation can be written for a homentropic fluid as follows

$$dh = \frac{dp}{\rho}. \tag{A.30}$$

So, Euler's equation can be written as

$$\frac{D\vec{v}}{Dt} = -\nabla h + \frac{1}{\rho}\vec{f}. \tag{A.31}$$

Let the total specific enthalpy B (Bernoulli constant) be defined as

$$B = h + \frac{1}{2}v^2. \tag{A.32}$$

The total enthalpy is achieved in a hypothetical and full reversible process, where the fluid particle is decelerated to a zero velocity. The following vector identity is used

$$(\vec{v} \cdot \nabla)\,\vec{v} = \frac{1}{2}\nabla v^2 + \vec{\omega} \times \vec{v}. \tag{A.33}$$

Euler's equation can be written as Crocco's equation

$$\frac{\partial \vec{v}}{\partial t} = -\nabla B - \vec{\omega} \times \vec{v} + \frac{1}{\rho}\vec{f}, \tag{A.34}$$

which is utilized if the sound production through vorticity is considered. The acceleration $\vec{\omega} \times \vec{v}$ corresponds to the Coriolis acceleration, which is experienced by an observer

moving with the particle, which rotates at an angular velocity $\overrightarrow{\Omega} = \frac{1}{2}\overrightarrow{\omega}$.

If the flow is non-rotational, potential and without any external forces, one can write

$$\frac{\partial \nabla \varphi}{\partial t} + \nabla B = 0, \tag{A.35}$$

which can be integrated to Bernoulli's equation

$$\frac{\partial \varphi}{\partial t} + B = \frac{\partial \varphi}{\partial t} + \frac{1}{2}v_2 + \int \frac{dp}{\rho} = g\left(t\right), \tag{A.36}$$

where $g\left(t\right)$ is a function determined by the boundary conditions. Being important only the gradient of φ, one can, without any loss of generality, absorb $g\left(t\right)$ into φ and make $g\left(t\right) = 0$. Bernoulli's equation is useful for acoustics by means that, for a homentropic flow, energy conservation is written as

$$\frac{\partial}{\partial t}\left(\rho B - p\right) + \nabla \cdot \left(\rho \overrightarrow{v} B\right) = \frac{\partial}{\partial t}\left(\rho \left(e + \frac{1}{2}v^2\right)\right) + \nabla \cdot \left(\rho \overrightarrow{v} B\right) = \overrightarrow{f} \cdot \overrightarrow{v}. \tag{A.37}$$

APPENDIX B – WAVE EQUATION, SOUND VELOCITY AND ACOUSTIC ENERGY

B.1 Magnitude order estimation

The audible sound wave frequency range for the human ear follows

$$20Hz \leq f \leq 20kHz. \tag{B.1}$$

The expression for the sound intensity level follows

$$PWL = 10log_{10}\left(\frac{Power}{10^{-12}W}\right). \tag{B.2}$$

The sound pressure level is described as

$$SPL = 20log_{10}\left(\frac{p'_{rms}}{p_{ref}}\right), \tag{B.3}$$

where $p_{ref} = 2 \cdot 10^{-5}$ Pa for air and $p_{ref} = 2 \cdot 10^{-6}$ Pa for other media. The intensity level can be defined as

$$IL = 10log_{10}\left(\frac{I}{I_{ref}}\right), \tag{B.4}$$

where the reference intensity level $I_{ref} = 10^{-12}$ W/m^2 is related with $p'_{rms} = 2 \cdot 10^{-5}$ for air, by the following relation, valid for progressive plane waves,

$$I = \left(\frac{p'_{rms}}{\rho_0 c_0}^2\right), \tag{B.5}$$

where $\rho_0 c_0 = 4 \cdot 10^2 \ kg/m^2 s$, for atmospheric conditions. The threshold of pain corresponds to pressure fluctuations of $p_{rms} = 200 \ Pa$. The correspondent fluctuations of relative

density, on atmospheric conditions, are given by

$$\frac{\rho'}{\rho_0} = \frac{p'}{\gamma p_0} \leq 10^{-3}, \tag{B.6}$$

where $\gamma = C_P/C_V$. By the definition of sound velocity, one can write that

$$\frac{\rho'}{\rho_0} = \frac{1}{\rho_0 c_0^2} p' = \frac{1}{\rho_0} \left(\frac{\partial \rho}{\partial p}\right)_s p'. \tag{B.7}$$

The factor $\frac{1}{\rho_0 c_0^2}$ is the adiabatic volumetric compressibility module of the media. For acoustic waves in a stagnant media, a progressive plane wave involves change of fluid particle position with a u' velocity, which is described as

$$u' = \frac{p'}{\rho_0 c_0}. \tag{B.8}$$

The factor $\rho_0 c_0$ is called characteristic impedance of the fluid. Dividing equation (B.8) by c_0, it is possible to observe that the acoustic Mach number u'/c_0 is a measure for the variation of relative density ρ'/ρ_0. In the absence of a mean flow ($u_0 = 0$), it implies that a convective term as $\rho (\vec{v} \cdot \nabla)$ in the equation of linear momentum conservation is a second order term and can be neglected in a linear approximation.

The amplitude of the displacement of a fluid particle δ corresponds to the wave harmonic propagation, in an angular frequency $\omega = 2\pi f$, is given by

$$\delta = \frac{u'}{\omega}. \tag{B.9}$$

To justify the linearization of the motion equations, it is necessary that the acoustic displacement is small, when compared to the characteristic length scale L, for the respective geometry. That means, the acoustic Strouhal number $St_a = \frac{L}{\omega}$ must be a great value. Specifically, if δ is larger than the wall curvature radius on the borders, the flow separates from the wall resulting on vortex detachment.

On the other hand, a small acoustic Strouhal number imply that non-linear effects resulting from vortex detachment are important. This is a strong non-linear effect because there is an increase of δ, resultant from a decrease on the frequency ω.

In order to the continuum hypothesis be valid, one should define a small air particle, related to measurement mechanisms, or the wavelength, but large when compared to the average free path, i.e.:

$$\lambda = \frac{c_0}{f}. \tag{B.10}$$

For gases, the continuum hypothesis is coupled to the assumption that the wave is isentropic and non-viscous. Kinematic viscosity and thermal diffusivity have, typically, the

same order of magnitude of the product between sound velocity and average free path. Let us write that

$$v \sim c\bar{l}. \tag{B.11}$$

The ration between wavelength and the average free path is defined as an acoustic Knudsen number, which can be also interpreted as a acoustic Fourier number, i.e.

$$\frac{\lambda}{\bar{l}} = \frac{\lambda c}{\nu} = \frac{\lambda^2 f}{\nu}. \tag{B.12}$$

This relates the diffusive length of the viscosity effects with the acoustic wavelength. This relation can be considered as a unstable Reynolds number, i.e.

$$Re_t = \frac{\left|\rho\frac{\partial u'}{\partial t}\right|}{\left|\mu\frac{\partial^2 u'}{\partial x^2}\right|} \sim \frac{\lambda^2 f}{\nu}. \tag{B.13}$$

B.2 Wave equation for a stagnant uniform fluid and compactness

B.2.1 Linearization and wave equation

For a quiescent fluid, equations from appendix A, related to fluid motion are simplified as follows

$$\frac{\partial \rho'}{\partial t} + \rho_0 \nabla \cdot \overrightarrow{v} = 0; \tag{B.14}$$

$$\rho_0 \frac{\partial \overrightarrow{v}}{\partial t} + \nabla p' = 0; \tag{B.15}$$

$$\rho_0 \frac{\partial s'}{\partial t} = 0. \tag{B.16}$$

In which the second order terms were neglected. The constitutive equation becomes

$$p' = c_0^2 \rho'. \tag{B.17}$$

By subtracting the temporal derivative of the continuity equation by the divergence of linear momentum conservation equation, the velocity vector is eliminated and it is obtained that

$$\frac{\partial^2 \rho'}{\partial t^2} - \nabla^2 p' = 0. \tag{B.18}$$

Applying the constitutive equation for uncoupling the variables,

$$\frac{\partial^2 p'}{\partial t^2} - c_0^2 \nabla^2 p' = 0; \tag{B.19}$$

$$\frac{\partial^2 \rho'}{\partial t^2} - c_0^2 \nabla^2 \rho' = 0; \tag{B.20}$$

By using the linearized Bernoulli equation, it is obtained that

$$\frac{\partial \phi'}{\partial t} + \frac{p'}{\rho_0} = 0. \tag{B.21}$$

Equation (B.21) should be a valid equation, because of the non-rotational characteristics of the flow. A new wave equation can be derived for φ', that presents the same form of equations (B.19) and (B.20). It follows:

$$\frac{\partial^2 \varphi'}{\partial t^2} - c_0^2 \nabla^2 \varphi' = 0. \tag{B.22}$$

By taking the gradient of equation (B.22), it is obtained a wave equation for the velocity, by knowing that $\overrightarrow{v'} = \nabla \varphi'$. Although being an abstract quantity, the potential function is convenient for acoustics calculations. The linearized Bernoulli equation is utilized to translate the obtained results with the potential function in less abstract quantities, as pressure fluctuations.

B.2.2 Simple solutions

The two simplest solutions for the wave equation are the d'Alembert solutions for one and three dimensions. For 1-D, the general solution follows

$$p' = f(x - c_0 t) + g(x + c_0 t); \tag{B.23}$$

$$v' = \frac{1}{\rho_0 c_0} \left(f(x - c_0 t) - g(x + c_0 t) \right), \tag{B.24}$$

in which f and g are functions defined by boundary and initial conditions, however arbitrary. The velocity v' is obtained after the pressure p', by means of the linearized momentum equation. Functions f and g are respectively correspondent to waves that occur on the positive and negative x-directions. This solution is useful to describe low frequency waves in rigid wall ducts and planar waves in free field. In order to allow a general orientation of the coordinate system, a planar waves free field is described generally as

$$p' = f(\overrightarrow{n} \cdot \overrightarrow{x} - c_0 t); \tag{B.25}$$

$$\overrightarrow{v'} = \frac{\overrightarrow{n}}{\rho_0 c_0} f(\overrightarrow{n} \cdot \overrightarrow{x} - c_0 t), \tag{B.26}$$

in which the propagation direction is described by the unit vector $\overrightarrow{n}$. Besides the 1-D case, the planar propagation on a free field may be found by a summation (or an integral)

in the $\overrightarrow{n}$ directions. A planar harmonic wave with frequency ω is usually written in its complex form

$$p' = Ae^{i\omega t - i\overrightarrow{k}\cdot\overrightarrow{x}};\tag{B.27}$$

$$\overrightarrow{v} = \frac{\overrightarrow{k}}{\rho_0\omega}Ae^{i\omega t - i\overrightarrow{k}\cdot\overrightarrow{x}};\tag{B.28}$$

$$c_0^2\left|\overrightarrow{k}\right|^2 = \omega^2,\tag{B.29}$$

in which the wave vector $\overrightarrow{k} = \overrightarrow{n}k = \overrightarrow{n}\frac{\omega}{c_0}$ indicates the propagation direction (or at least on the present stagnant and uniform media).

In 3-D, there is a general solution for spherically symmetric waves, dependent on radial distance only. They are similar to the 1-D solutions because of the combination $rp(r,t)$ satisfy the 1-D wave equation.

One should note, however, that the radial velocity, differently from the 1-D case, the radial velocity component v_r' is more difficult. The velocity should be determined by obtaining pressure, by integrating the momentum equation in time, i.e.

$$p' = \frac{1}{r}f(r - c_0 t) + \frac{1}{r}g(r + c_0 t);\tag{B.30}$$

$$v' = \frac{1}{\rho_0 c_0}\left(\frac{1}{r}f(r - c_0 t) - \frac{1}{r^2}F(r - c_0 t)\right) - \frac{1}{\rho_0 c_0}\left(\frac{1}{r}g(r + c_0 t) - \frac{1}{r^2}G(r + c_0 t)\right),\tag{B.31}$$

in which $F(z) = \int f(z)dz$ and $G(z) = \int g(z)dz$. Usually, there are only waves coming out, what signifies that, before an instant of time t_0, the field disappears. So, $f(z) = 0$ for $z = r - c_0 t \geq r - c_0 t_0 \geq -c_0 t_0$ because $r \geq 0$ and $g(z) = 0$ for any $z = r + c_0 t \leq r + c_0 t_0$. Being r non-restricted by the pointed out conditions, it implies that, for any value of z,

$$g(z) \equiv 0.\tag{B.32}$$

This solution obtained is specially used to describe a field of small symmetric sources, modeled after a point in space. Besides that, other solutions for the wave equation can be generated by differentiation of the position. For example, if $\frac{\partial}{\partial x}r = \frac{r}{x}$, then

$$p' = \frac{x}{r^2}\left(f'(r - c_0 t) - \frac{1}{r}f(r - c_0 t)\right);\tag{B.33}$$

$$v' = \frac{1}{\rho_0 c_0}\frac{x}{r^2}\left(f'(r - c_0 t) - \frac{2}{r}f(r - c_0 t) + \frac{2}{r^2}F(r - c_0 t)\right),\tag{B.34}$$

in which f' represents the derivative of f with respect to its argument.

Being the roles of r and t symmetrical in f and anti-symmetrical in g, a condition of causality in t is formulated, also as a boundary condition. A causal wave disappears from

outside of a large sphere, whose radius grows linearly in time, with velocity c_0. This is valid for any field in the free space, with a finite-sized source because far from the field, it is itself simplified as a point source.

In the case of an ideal temporal harmonic field, it is not possible to directly apply this causality . However, a modified form of the boundary condition in r is utilized, the so-called *radiation condition of Sommerfeld*, as

$$\lim_{r \to \infty} r \left(\frac{\partial p^{'}}{\partial t} + c_0 \frac{\partial p^{'}}{\partial r} \right).$$ (B.35)

B.2.3 Compactness

In regions, e.g. borders, where the acoustic potential $\varphi^{'}$ varies significantly along distance L, which are small, when compared to the wavelength λ, the acoustic flow can be locally approximated to an incompressible potential flow. This region can be called compact, and a source with length much smaller than λ is called compact source. In a more precise definition, it is assumed that one may distinguish a typical time scale τ, or frequency ω and length scale L in the problem. In the non-dimensional form, the wave equation is written as

$$\sum_{i=1}^{3} \frac{\partial^2 \varphi}{\partial \hat{x}_i^{\,2}} + (He)^2 \frac{\partial^2 \varphi}{\partial \hat{t}^2},$$ (B.36)

where

$$He = \frac{L}{c_0 \tau} = \omega L c_0 = 2\pi L \lambda = kL,$$ (B.37)

and

$$\hat{t} = \frac{t}{\tau} = \omega t, \hat{x}_i = \frac{x_i}{L}.$$ (B.38)

The non-dimensional parameter He is called Helmholtz number. When L and τ are well chosen, $\frac{\partial^2 \varphi}{\partial \hat{x}_i^2}$ and $frac\partial^2 \varphi \partial \hat{t}^2$ have the same order of magnitude, and the character of wave motion is described by Helmholtz number. In a compact region, $He \ll 1$. That occurs near singularities, where spatial gradients grow large, or at low frequencies, where temporal derivatives become small. Within compact regions, the temporal derivative multiplied by a small He value results in negligible values. This results in Lapace equation

$$\nabla^2 \varphi^{'} = 0.$$ (B.39)

Equation (B.39) describes a incompressible potential flow, $\nabla \cdot \overrightarrow{v} = 0$. That makes incompressible potential flow theory applicable to determine the acoustic field for a compact region. If the compact region is placed within a large acoustic region of a simple nature,

it acts on the scale of the largest region as a punctual source, allowing a relative simple acoustic field. The alignment is utilized intuitively, in the first order approximation.

B.3   Sound velocity in an ideal gas

It was considered so far that sound velocity has a constant value. However, in many cases, c_0 is not uniform in space, what affects the wave propagation. So, the influence of many parameters in sound velocity is discussed.

At atmospheric pressure, air behaves as an ideal gas, so

$$p = \rho RT, \tag{B.40}$$

where R can be expressed in two forms for ideal gases

$$R = \frac{k_B N_A}{M}; \tag{B.41}$$

$$R = C_P - C_V. \tag{B.42}$$

For an ideal gas, internal energy depends only on temperature, i.e. $de = C_V dT$. So, applying the second law of thermodynamics for an isentropic process, it is obtained that

$$C_V dT = -pd(\rho)^{-1}, \tag{B.43}$$

or

$$\frac{dT}{T} = \frac{R}{C_V} \frac{d\rho}{\rho}. \tag{B.44}$$

So, for an isentropic process, it can be written that

$$\frac{d\rho}{\rho} + \frac{dT}{T} = \frac{dp}{p} = \gamma \frac{d\rho}{\rho}, \tag{B.45}$$

where $\gamma = \frac{C_P}{C_V}$.

By definition of sound velocity $c^2 = \left(\frac{\partial p}{\partial \rho}\right)_s$ and the following relation, it is obtained that

$$c = \sqrt{\frac{\gamma p}{\rho}} = \sqrt{\gamma RT}. \tag{B.46}$$

For an ideal gases mixture, it is necessary to work with molar fractions, i.e.

$$M = \sum_i M_i X_i. \tag{B.47}$$

So, the ratio between specific heats γ can be written as

$$\gamma = \frac{\sum \frac{\gamma_i X_i}{(\gamma_i - 1)}}{\sum \frac{X_i}{(\gamma_i - 1)}}. \tag{B.48}$$

The mixture of gases in air does not affect much the sound velocity, however, it may affect drastically the damping of sound waves, so, its propagation. The dependency of sound velocity on temperature is responsible for the difference of sound propagation at different atmospheric regions.

B.4   Influence of temperature gradients

It is important to derive a wave equation in a more general fashion, with respect to an arbitrary temperature distribution in a stagnant ideal gas. From the linearized continuity equation and the linear momentum conservation equation, let us write that

$$\frac{\partial \rho}{\partial t} + \nabla \cdot \left(\rho_0 \vec{v}' \right) = 0; \tag{B.49}$$

$$\rho_0 \frac{\partial \vec{v}'}{\partial t} + \nabla p' = 0; \tag{B.50}$$

$$\frac{\partial s}{\partial t} + \vec{v}' \cdot \nabla s_0' = 0, \tag{B.51}$$

where ρ_0 and s_0 vary in space. The constitutive equation for isentropic flow $\left(\frac{Ds}{Dt} = 0 \right)$ is

$$\frac{Dp}{Dt} = c^2 \frac{D\rho}{Dt}, \tag{B.52}$$

which can also be written in the form of

$$\frac{\partial p'}{\partial t} + \vec{v}' \cdot \nabla p_0 = c_0^2 \left(\frac{\partial \rho'}{\partial t} + \nabla \cdot \left(\rho_0 \vec{v}' \right) \right). \tag{B.53}$$

Combining equation (B.53) and the continuity equation, it becomes

$$\frac{\partial p'}{\partial t} + \vec{v}' \cdot \nabla p_0 + \rho_0 c_0^2 \nabla \cdot \vec{v}' = 0. \tag{B.54}$$

If temperature gradients are considered at low heights, variations in p_0 can be neglected $\left(\frac{\nabla p_0}{p_0} \ll \frac{\nabla T_0}{T_0} \right)$, and the following approximation can be made:

$$\nabla \cdot \vec{v}' = -\frac{1}{\rho_0 c_0^2} \frac{\partial p'}{\partial t}. \tag{B.55}$$

By taking the divergence of the linear momentum equation, comes the following

$$\frac{\partial}{\partial t}\left(\nabla \cdot \vec{v}'\right) + \nabla \cdot \left(\frac{1}{\rho_0}\nabla p'\right) = 0. \tag{B.56}$$

By eliminating $\nabla \cdot \vec{v}'$ from equation (B.56), it is obtained that

$$\frac{\partial^2 p'}{\partial t^2} - c_0^2 \rho_0 \nabla \cdot \left(\frac{1}{\rho_0}\nabla p'\right) = 0. \tag{B.57}$$

For an ideal gas, $c_0^2 = \gamma \frac{p_0}{\rho_0}$, and being p_0 assumed as uniform, one can write that

$$\rho_0 c_0^2 = \gamma p_0. \tag{B.58}$$

Equation (B.58) represents a constant. So, a new wave equation can be derived and is represented as

$$\frac{\partial^2 p'}{\partial t^2} - \nabla \cdot \left(c_0^2 \nabla p'\right) = 0. \tag{B.59}$$

Equation (B.59) is more complex than the wave equation obtained in past sections, given the non-uniformity of c_0. It is noteworthy that, differently from quiescent fluids, the wave equation for pressure fluctuations p' for ideal, non-stagnant and non-uniform gases is not valid for density fluctuations. This is because density fluctuations are related not only to pressure variations, but also convective effects.

B.5   Influence of the mean flow

On the presence of a mean flow, which satisfies the following conditions:

$$\nabla \cdot \rho_0 \vec{v_0} = 0; \tag{B.60}$$

$$\rho_0 \vec{v_0} \nabla \cdot \vec{v_0} = -\nabla p_0; \tag{B.61}$$

$$\vec{v_0} \cdot \nabla s_0 = 0; \tag{B.62}$$

$$\vec{v_0} \cdot \nabla p_0 = c_0^2 \vec{v_0} \cdot \rho_0; \tag{B.63}$$

The linearized conservative laws and the constitutive equation for isentropic flow become

$$\frac{\partial \rho'}{\partial t} + \vec{v_0}\nabla \rho' + \vec{v}' \cdot \nabla \rho_0 + \rho_0 \nabla \cdot \vec{v}' + \rho' \nabla \cdot \vec{v_0} = 0; \tag{B.64}$$

$$\rho_0 \left(\frac{\partial \vec{v}'}{\partial t} + \vec{v_0} \cdot \nabla \vec{v}' + \vec{v}' \cdot \nabla \vec{v_0}\right) + \rho' \vec{v_0} \cdot \nabla \vec{v_0} = -\nabla p; \tag{B.65}$$

$$\frac{\partial s'}{\partial t} + \vec{v_0}\nabla s' + \vec{v}' \cdot \nabla s_0 = 0; \tag{B.66}$$

$$\frac{\partial p^{'}}{\partial t} + \overrightarrow{v_0}\nabla p^{'} + \overrightarrow{v}^{'} \cdot \nabla p_0 = c_0^2 \left(\frac{\partial \rho^{'}}{\partial \rho} + \overrightarrow{v_0} \cdot \nabla \rho^{'} + \overrightarrow{v}^{'} \cdot \nabla \rho_0\right) + c_0^2 \left(\overrightarrow{v_0} \cdot \nabla \rho_0\right) \left(\frac{p^{'}}{p_0} - \frac{\rho^{'}}{\rho_0}\right).$$
(B.67)

The wave equation can be obtained from equations (B.64), (B.65), (B.66) and (B.67), if simplification assumptions are introduced. For an uniform media, with uniform flow velocity $\overrightarrow{v_0} \neq 0$, it can be derived that

$$\left(\frac{\partial}{\partial t} + \overrightarrow{v_0} \cdot \nabla\right)^2 p^{'} - c_0^2 \nabla^2 p^{'} + 0,$$
(B.68)

in which $\frac{\partial}{\partial t} + \overrightarrow{v_0} \cdot \nabla$ denotes a temporal derivative that moves with the mean flow.

B.6 Sound sources

B.6.1 Inverse problem and source singularity

Let us consider the wave equation with a source q, i.e.

$$\frac{\partial^2 p^{'}}{\partial t^2} - c_0^2 \nabla^2 p^{'} = q.$$
(B.69)

Frequently, situations that the source q is concentrated in a determined region of the space within a uniform and stagnant fluid are considered. A new sound field can be constructed, for example $p^{'} + F$, so

$$\left(\frac{\partial^2 p^{'}}{\partial t^2} - c_0^2 \nabla^2\right)\left(p^{'} + F\right) = q + \left(\frac{\partial^2 p^{'}}{\partial t^2} - c_0^2 \nabla^2\right) F.$$
(B.70)

In a general manner, this source is not equal to q. That proves that the acoustic field, outside the source region, is not sufficient for the singular source determination.

B.6.2 Mass and momentum injection

Let us consider initially the non-homogeneous continuity equation and the linearized momentum equation, respective as

$$\frac{\partial}{\partial t}\rho + \nabla \cdot \rho \overrightarrow{v} = m;$$
(B.71)

$$\frac{\partial}{\partial t}\left(\rho \overrightarrow{v}\right) + \nabla p^{'} = \overrightarrow{f}.$$
(B.72)

The mass source m consists of the injection of mass with density ρ_m and volumetric fraction $\beta = \beta(x,t)$, injected at a rate of

$$m = \frac{\partial}{\partial t}\left(\beta \rho_m\right). \tag{B.73}$$

The source region is where $\beta \neq 0$. The new fluid total density, calling ρ_f the density before the injection can be written as

$$\rho = \beta \rho_m + (1 - \beta)\,\rho_f, \tag{B.74}$$

where the injected mass does not mixture with the initial fluid. A substitution can be made, i.e.

$$\frac{\partial}{\partial t}\rho_f + \nabla \cdot (\rho \overrightarrow{v}) = \frac{\partial}{\partial t}\left(\beta\rho_f\right); \tag{B.75}$$

$$\frac{\partial^2}{\partial t^2}\rho_f - \nabla^2 p' = \frac{\partial^2}{\partial t^2}\left(\beta\rho_f\right) - \nabla \cdot \overrightarrow{f}. \tag{B.76}$$

If, for simplicity, it is assumed that $p' = c_0^2 \rho_f'$ for the whole space where ρ_f' is the fluctuation part of ρ_f, what represents the sound field outside the source region, it results in

$$\frac{1}{c_0^2}\frac{\partial^2}{\partial t^2}p' - \nabla^2 p' = \frac{\partial^2}{\partial t^2}\left(\beta\rho_f\right) - \nabla \cdot \overrightarrow{f}. \tag{B.77}$$

Equation (B.77) shows that mass injection is a sound source, because of the displacement of fluid particles. Consequently, the injection of a high mass fluid is not necessary an effective sound source.

It can also be seen that mass injection of a constant density fluid does not produce any sound, because the term $\frac{\partial^2}{\partial t^2}\beta\rho_f$ disappears. In addition to that, it can be demonstrated analogously that, in a linear approximation, the presence of a uniform force field does not affect the sound field of a uniform stagnant fluid.

B.6.3 Lighthill's analogy

Lighthill's analogy is formally exact and derived without approximation from the Navier-Stokes equation, for acoustics. It is useful when considering the case of a source region immerse in a uniform and stagnant fluid. It is assumed at least that the observer who detects the acoustic field in a x point, at a instant of time t, it is immerse in a stagnant and uniform fluid media, characterized by a sound velocity c_0. Consequently, the acoustic field in a receiver or observer position is described by the following wave equation

$$\frac{\partial^2 \rho'}{\partial t^2} - c_0^2\nabla^2\rho' = 0, \tag{B.78}$$

where ρ' is chosen as the acoustic variable, which is the most convenient choice for prediction of sound produced by turbulent flows. The key idea for the so-called *Lighthill's aeroacoustic analogy* is that one can derive from the same motion equations a wave equation with the propagation term as in equation (B.78). Consequently, the uniform and stagnant fluid at the receiver position is assumed to be extended to the whole space, and any start of the ideal acoustic behavior predicted by equation (B.78) is equivalent to a sound source to the receiver.

By taking the temporal derivative from continuity equation and eliminating the term $\frac{\partial m}{\partial t}$, it is obtained that

$$\frac{\partial^2}{\partial t \partial x_i}(\rho v_i) = \frac{\partial m}{\partial t} - \frac{\partial^2 \rho}{\partial t^2} = -\frac{\partial^2 \rho_f}{\partial t^2} + \frac{\partial^2 \beta \rho_f}{\partial t^2}. \tag{B.79}$$

Taking the divergence of the conservation of linear momentum equation, it is obtained that

$$\frac{\partial^2}{\partial t \partial x_i}(\rho v_i) = -\frac{\partial^2}{\partial x_i \partial x_j}(P_{ij} + \rho v_i v_j) + \frac{\partial f_i}{\partial x_i}. \tag{B.80}$$

From equations (B.79) and (B.80), the following relation is obtained

$$\frac{\partial^2 \rho_f}{\partial t^2} = \frac{\partial^2}{\partial x_i \partial x_j}(P_{ij} + \rho v_i v_j) + \frac{\partial^2 \beta \rho_f}{\partial t^2} - \frac{\partial f_i}{\partial x_i}. \tag{B.81}$$

Being $\rho_f = \rho_0 + \rho'$, where only ρ' varies with time, one can derive a wave equation for ρ', by subtracting the term $c_0^2 \left(\frac{\partial^2 \rho'}{\partial x_i^2}\right)$, where c_0 does not refer to the local sound velocity, but the sound velocity at the receiver position. So, the Lighthill's equation is obtained as

$$\frac{\partial^2 \rho'}{\partial t^2} - c_0^2 \left(\frac{\partial^2 \rho'}{\partial x_i^2}\right) = \frac{\partial^2 T_{ij}}{\partial x_i \partial x_j} + \frac{\partial^2 \beta \rho_f}{\partial t^2} - \frac{\partial f_i}{\partial x_i}, \tag{B.82}$$

where the Lighthill's stress tensor is defined as

$$T_{ij} = P_{ij} - \rho v_i v_j - \left(c_0^2 \rho' + p_0\right)\delta_i. \tag{B.83}$$

; The following identity is utilized

$$c_0^2 \left(\frac{\partial^2 \rho'}{\partial x_i^2}\right) = \frac{\partial^2 T_{ij}\left(c_0^2 \rho' \delta_{ij}\right)}{\partial x_i \partial x_j}. \tag{B.84}$$

The identity is exact because of c_0 being a constant. It can also be written that

$$T_{ij} = P_{ij} - \rho v_i v_j - \tau_{ij} + \left(p' - c_0^2 \rho'\right)\delta_i. \tag{B.85}$$

This is the most usual form of the Lighthill's stress tensor found in the literature. In equation (B.85), it is possible to distinct three aeroacoustic processes, which result in

sound sources:

- Reynolds tensor, which characterizes the non-linear convective forces;

- Viscous forces;

- The fluctuations over a pattern of constant sound velocity c_0, or deviation from the isentropic condition.

Since no approximation was made in the derivation, Lighthill's equation is complicated to be solved, and an analytical solution is only possible by introducing some additional assumptions, capable of simplifying the equation, as for the Navier-Stokes equations.